PhD-FSTC-2018-25
The Faculty of Sciences, Technology and Communication

DISSERTATION

Defence held on 26/03/2018 in Luxembourg

to obtain the degree of

DOCTEUR DE L'UNIVERSITÉ DU LUXEMBOURG

EN PHYSIQUE

by

David SPIRITO
Born on 9 March 1987 in Libramont-Chevigny (Belgium)

LARGE-SCALE AND FLEXIBLE NANOGENERATOR BASED ON ZnO CONICAL NANOSTRUCTURES BY NANO-IMPRINT LITHOGRAPHY AND ATOMIC LAYER DEPOSITION

Dissertation defence committee

Prof. Dr. Jens Kreisel, dissertation supervisor
Professor, Université du Luxembourg, Luxembourg Institute of Science and Technology

Dr. Damien Lenoble
Luxembourg Institute of Science and Technology

Prof. Dr. Ludger Wirtz, Chairman
Professor, Université du Luxembourg

Associate Prof. Dr. Anna Maria Coclite
Associate Professor, Graz University of Technology

Prof. Dr. Laurent Francis, Vice Chairman
Professor, Université Catholique de Louvain

“Next time someone complains that you have made a mistake, tell him that may be a good thing. Because without imperfection, neither you nor I would exist.”

Stephen Hawking

Remerciements

English version below the French one.

Durant ces quatre années Luxembourgeoises, j'ai rencontré d'incroyable personnes, que ce soit dans le cadre professionnel ou en dehors.

Tout d'abord, je tiens à remercier les membres du jury, Anna Maria Coclite et Laurent Francis pour avoir accepté de venir jusqu'au Luxembourg pour évaluer mon travail, ainsi que Ludger Wirtz, président du jury et membre du CET.

Ensuite, les deux personnes sans qui je n'aurais pas pu faire ce travail, mes superviseurs de thèse, Damien Lenoble et Jens Kreisel. Ils ont tous les deux su me guider grâce à leurs conseils avisés tout en me laissant la liberté d'explorer les dédales de la science. Patients et disponibles (malgré leurs responsabilités), leur soutien et leur confiance m'ont permis d'accomplir ce projet qu'ils m'avaient confié. Je n'aurais pas pu espérer mieux comme superviseurs que ce duo Franco-Allemand.

Un tout grand merci à Emmanuel Defay pour son aide et son pragmatisme. En tant que chef de groupe, il a su m'aiguiller pour m'apprendre à utiliser au mieux les ressources mise à disposition du groupe et au-delà.

Pour ses idées et sa contribution scientifique, un énorme merci à Jérôme Polesel. Même si nous ne faisions pas partie du même groupe, de simples discussions ont permis de résoudre nombreuses de mes questions scientifiques et problèmes techniques.

Continuant dans la contribution scientifique, ce fut un réel de plaisir d'interagir avec les gens de la « plateforme » : l'équipe des « chauve-souris » (Jérôme[2], Jean-Luc, Brahime, Yves), Nathalie, et plus spécialement Patrick avec qui nous avons souffert dans l'apprentissage du PFM (il en souffre encore).

Il y a aussi le groupe FMT et les anciens UGN (de l'époque du Lippmann) et plus généralement l'unité nanomatériaux avec qui j'ai travaillé et passé d'excellents moments. Tout d'abord, ceux avec qui j'ai travaillé au labo : Didier (maitre FIB-SEM), Bianca-Rita et Kévin (team PRODOS), Stéphanie (comparse de cleanroom, NIL & cie), Maël (la lumière du Raman). Ensuite, ceux avec qui tout a commencé en G1.28 : Gaëlle, Guillaume et Mads (les 4 fantastiques avec moi ;-). Puis les autres avec qui j'ai partagé les bureaux G1.31, G1.33 et F1.14 : Shankari, Alexander, Sunil, Carlos, Vincent, Nohora, Olga, Hameeda, Serena, Catarina, Sabrina, Divya, Alex, Peng, Mauro, Rhishab, Raoul, Tai, Joao,… sans oublier tous les autres de l'équipe : Nicolas, Antoine, Sebastjan, Constance, Charlotte, Romain, Hong Tao, Guillaume, Petru, Manuel, Torsten, Jorge, Cesar, Naoufal, Renaud,…

Les pauses café, Ô combien fructueuses au niveau scientifique[1], sociales et culturelles m'ont permis de rencontrer d'autres personnes avec qui j'ai passé de bons moments, du LIST ou

[1] Véridique ! Les pauses café m'ont sauvé de bien des impasses en échangeant et débattant d'idées scientifiques.

d'ailleurs, transitant par la cafét' : Maxime, Greg, Laura, Dana, Ingrid, Conrad, Jan, Sara, Tobias, …

Dans l'ombre du département, celle qui dirige tout d'une main de fer dans un gant de velours, l'adorable Corinne. Sans elle, je me demande ce que j'aurais bien pu faire.

En dehors du cadre de travail, je tiens à remercier les amis de longue date et ma famille, ainsi que tous ceux que j'ai rencontré avec qui j'ai tissé de nouveaux liens d'amitiés : merci ! Merci d'avoir été là, surtout les derniers mois de ma thèse pour me soutenir et me motiver quand j'en avais besoin.

Finalement (last but not ~~LIST~~ least), Big up à ma Gaëlle-Géraldine-Gazelle qui s'est dévouée pour la relecture/correction « *Des aventures de PENG* ».

J'ai probablement oublié des personnes. J'espère que vous vous retrouverez dans les lignes ci-dessus ou dans la version anglaise. Pardonnez ma mémoire de poisson rouge.

English version :

Thank you !

Contents

List of abbreviations **1**

General introduction **3**

1. State of the Art **7**

1.1. Energy harvesting 7

1.1.1. Solar/Thermo-photovoltaic 7

1.1.2. Thermoelectric 8

1.1.3. Biochemical (microbial fuel cell) 8

1.1.4. Mechanical 9

1.2. Mechanical energy harvesting 10

1.2.1. Electromagnetic 10

1.2.2. Electrostatic 11

1.2.3. Triboelectric 12

1.2.4. Piezoelectric 13

1.3. Piezoelectric energy harvesting devices 15

1.4. Nanogenerators based on ZnO nanowires 20

1.4.1. Working principle 20

1.4.2. Lateral ZnO nanowires 22

1.4.3. Vertical ZnO nanowires 24

1.4.4. ZnO fiber structures 25

1.5. PENG performance optimization and characterization 26

1.6. Aim and approach of this project 32

2. Experimental Part **35**

2.1. Experimental process 35

2.1.1. Spin coating 35

2.1.2. Nano-imprint Lithography (NIL) 36

2.1.3. Reactive Ion etching (RIE) 40

2.1.4. Atomic Layer Deposition (ALD) 40

2.1.5. Metal Evaporator/Sputtering 43

2.1.6. Plasma Radical Assisted Polymerization Chemical Vapor Deposition 43

2.1.7. Wet etching 44

2.2. Techniques for material characterization 44

2.2.1. Ellipsometry 44

2.2.2. Scanning Electron Microscopy and Focus Ion Beam (FIB-SEM) 45

2.2.3. Transmission Electron Microscopy (TEM) 47

2.2.4. X-Ray Diffraction (XRD) 47
2.2.5. X-Ray Photoelectron Spectroscopy (XPS) 48
2.2.6. Secondary Ion Mass Spectroscopy (SIMS) 49
2.2.7. Raman Spectroscopy & Photoluminescence 50
2.2.8. Scanning Probe Microscopy 50
2.2.9. Four Point Probe Resistivity Measurement 51
2.3. Techniques for device characterization 52
2.3.1. Impedance meter 52
2.3.2. Small device setup 52
2.3.3. Setup for large membrane device 53
2.4. Conclusion 56
3. Study of ZnO by Atomic Layer Deposition 58
3.1. Introduction 58
3.2. Experimental 60
3.3. Results and discussion 61
3.3.1. Chemical composition 61
3.3.2. Average structure, local structure and defects 64
3.3.3. Optical gap and electronic properties 68
3.3.4. Piezoelectric properties 72
3.4. Conclusion 74
4. P-PENG fabrication, electronic engineering and output performances 76
4.1. Introduction 76
4.2. P-PENG mechanical design based on finite element modelling 76
4.3. Device engineering 78
4.4. Morphological and structural properties 82
4.5. P-PENG electronic engineering and output performances 86
4.5.1. p-n junction P-PENG 86
4.5.2. Blocking barrier P-PENG 92
4.6. Setup for accurate characterization with speaker and vibrometer 99
4.7. P-PENG perspectives for optimization 108
4.8. Conclusion 110
Conclusion and perspectives 112

List of abbreviations

AC: Alternative Current

AFM: Atomic Force Microscopy

ALD: Atomic Layer Deposition

c-AFM: Conductive Atomic Force Microscopy

CMOS: Complementary Metal Oxide Semiconductor

CVD: Chemical Vapor Deposition

DC: Direct Current

DEZ: Diethylzinc

EDOT: 3,4-ethylenedioxythiophene

FEM: Finite Element Modeling

FIB: Focus Ion Beam

HRTEM: High Resolution Transmission Electron Microscopy

IoT: Internet of Things

IPS: Intermediate Polymer Stamp

ISO: International Organization for standardization

ITO: Indium Tin Oxide

MEMS: Microelectromechanical System

NIL: Nano-imprint Lithography

NW: Nanowire

P-PENG: Patterned Piezoelectric Nanogenerator

PDMS: Polydimethylsiloxane

PEEK: Polyether ether ketone

PENG: Piezoelectric Nanogenerator

PET: polyethylene terephthalate

PEDOT: Poly(3,4-ethylenedioxythiophene)

PFM: Piezoresponse Force Microscopy

PMMA: Polymethyl methacrylate

PRAP: Plasma Radical Assisted Polymerization

PSS: Polystyrene sulfonate

PVDF: Polyvinylidene difluoride

RIE: Reactive Ion Etching

SEM: Scanning Electron Microscopy

SIMS: Secondary Ion Mass Spectroscopy

SPM: Scanning Probe Microscopy

T_g: Glass-transition Temperature

TEM: Transmission Electron Microscopy

TENG: Triboelectric Nanogenerator

TMA: Trimethylaluminum

VLS: Vapor-Liquid Solid

XDR: X-Ray Diffraction

XPS: X-Ray Photoelectron Spectroscopy

General introduction

The emergence and rapid expansion of the Internet of Things (IoT) is driving a new increase of the global market of portable electronics and wireless sensors and actuators. Large companies are investing billions of dollars in this new technology [1]. By the end of 2017, around 6 % of the north American houses have become connected by IoT [2]. The market expects a growth of 28 % by 2019. The example of the connected sensors of the IoT for the healthcare predicts a market larger than 117 billion $ for 2020 [3]. From healthcare monitoring systems to smart objects and connected clothes, electronic components, all require a power source to sense and communicate. For portable devices, habitual batteries appear as the easiest reliable power source but may not be the best choice regarding their limited lifetime and environmental issues. Following Moore's law and the More-than-Moore technologies, communication electronics and sensors are decreasing in size and in power consumption, which in turn makes self-powering devices by harvesting energy from the environment a sustainable second source of power.

Considering the different sources of renewable energy, vibrational-mechanical energy is one of the most widespread for wearable devices. Advances during the last decade in mechanical-to-electrical energy conversion can fill the gap for self-powering systems. Namely, piezoelectric nanogenerators, based on nanostructured piezoelectric materials, and triboelectric nanogenerators, based on contact electrification, have demonstrated power outputs large enough for LEDs, LCD screen and monitoring biological signals [4]. The performance of piezoelectric nanogenerators depends on the piezoelectric properties of the material, its nano-structuration and the device architecture [5]. The development of low-cost and lead-free material for nanogenerators open the opportunities for economic and

environmental friendly devices. To date, the most investigated and promising material considered for piezoelectric nanogenerators is zinc oxide (ZnO). Combined with its optical and semiconductor properties, ZnO triggers an interest in self-powered devices with a large variety of applications such as gas, strain, biological sensors and opto-electronic [6].

Despite the fact that piezoelectric nanogenerators with ZnO nanowires (NWs) have been much investigated as building blocks, there remains many open issues with regard to the optimization of materials processing and materials properties enabling novel device architecture towards the increase of performance. Two main avenues are under investigations: first, tuning the piezoelectric properties of ZnO NWs and second, the optimization of the devices architecture driving the electromechanical performances [7]. A third way of optimization remains neglected and unexplored due to the limited bottom-up growth process of ZnO NWs: the optimization of the height, width and density of ZnO NWs. The currently proposed low-cost growth process of ZnO NWs with wet chemistry uses a bottom-up approach, barely controlling the aspect ratio and density of the piezoelectric nanowires. Moreover, the control of the piezoelectric properties with this bottom-up process often requires high temperature post-process. This jeopardizes the use of flexible large scale and low-cost substrate which is, the most obvious benefit of nanogenerators for powering billions of devices.

Objectives and outline of this work

The aim of our work is to conceptualize by models, to fabricate and to investigate a new kind of piezoelectric nanogenerator based on tailored ZnO nanostructures to rigorously investigate the interplay between tunable piezoelectric materials properties, device architectures and the output power performance. To achieve this goal, we have chosen to privilege an accurately controlled top-down process over the common bottom-up approach. More precisely, we propose a top-down approach that allows an accurate control of the aspect ratio and density of ZnO nanowires with Nano-Imprint Lithography (NIL). Then, using Atomic Layer Deposition (ALD) as a low-temperature process of ZnO, we intend to tune the electronic transport and the local structure of ZnO with nitrogen doping to optimize the piezoelectric properties. We will show that this approach enables an easy scale up for the fabrication of large flexible piezoelectric nanogenerators showing original properties.

In the first part of the manuscript, we describe the context and provide an analysis of the recent piezoelectric nanogenerators. Performance, limitations and improvements are discussed to define the research strategy of this work.

Then, in a second part, the experimental chapter describes the machines used for the fabrication of the piezoelectric nanogenerator based on ZnO. The techniques used for the characterization are described and discussed with regards to the provided information and their limitations. An original electromechanical setup is built to accurately characterize the piezoelectric nanogenerators.

In a third chapter, we report the fabrication and characterization of ZnO thin film by ALD at a temperature as low as 80°C as the building block for a piezoelectric nanogenerator. Combined characterization techniques highlight the control of the ZnO properties with a nitrogen doping without any plasma assistance.

In the last part, we demonstrate the fabrication of functional ZnO piezoelectric nanogenerator based on NIL and ALD. Different electronic architectures are presented in order to optimize the performance. The scaling up displays the feasibility of large nanogenerator on flexible substrate. A special electronic setup with a mechanical actuation is used to accurately characterize and quantitatively compare nanogenerators with different nitrogen doped ZnO.

1. State of the Art

This introductory chapter presents the context of energy harvesting, by focusing on the conversion of mechanical energy into electrical energy. Among the transduction of mechanical energy, we specifically focus on piezoelectric devices and on those which are based on ZnO nanostructures. We analyze the reported performances, the pros and cons, and the application cases, which form the basis of this work.

1.1. Energy harvesting

All kinds of energy source can be harvested with different working principle: solar by thermo-photovoltaic conversion, thermal by thermoelectricity, mechanical by electro-magnetic/static and piezoelectric effect, or biochemical by biochemical reactions [8]. Each harvesting principle has its own features, limitations and matches different potential applications. Some devices are also developed to harvest simultaneously multiple types of energies such as thermal, mechanical and solar energy [9].

1.1.1. Solar/Thermo-photovoltaic

Solar power is one of the cleanest and most reliable energy resources. Compared to photovoltaic systems, the thermo-photovoltaic increases the range of transduced electromagnetic waves. The thermo-photovoltaic effect performs a better energy conversion than the photovoltaic energy thanks to a module combining a micro-emitter and an optical filter. The working principle is illustrated in the Figure 1-1a, relying on a heat source. Usually, the solar spectrum is converted into thermal radiation, but other kinds of radiative source like a thermal combustion or a radionuclide radiation can be used. Then, photons are filtered and focused onto the photovoltaic cell to generate charges at the p- and n-type semiconductors junction that induce a potential difference between output electrodes [10]. The advantages of this system include a cheap process fabrication, easy integration to devices, lack of emission or noise, lack of moving parts and reliability of the energy source [11]. The drawbacks of this

system are the limited solar radiation exposition, a major heat loss and the low conversion efficiency for cheap devices.

1.1.2. Thermoelectric

The energy harvesting via a thermal gradient is mostly based on the Seebeck effect. A typical system is composed of two different materials (metals, semiconductors or alloys) acting as p- and n-type materials, connected electrically in series and thermally in parallel [11]. The same design is used for a thermocouple. The working principle is described in Figure 1-1b. There is a higher temperature at one end and a lower temperature at the other end. The difference of temperature generates a potential difference. The advantages of thermoelectric energy harvesting are their reliability, low cost, scalability, non-moving blocks, lack of emission and noise, plain configuration, as well as reliability of the energy source. Additionally, they have a long operation time. Such systems recycle wasted-heat energy (e.g. human body heat loss) but unfortunately, this kind of energy source is limited by the low energy-conversion-rate and the low temperature-gradient (< 10°C) [10]. Therefore, optimizations are focusing on a higher energy conversion with materials combining a higher electron mobility and a lower thermal conductivity.

1.1.3. Biochemical (microbial fuel cell)

The biochemical energy harvesting system is often considered as the cleanest energy harvesting and the most environmental friendly with its bio-electrochemical transduction. The microbial fuel cell, represented in Figure 1-1c, is composed by an anode and a cathode chamber separated by an electrolyte membrane. The working principle is based on an oxidation reaction in the anode releasing electrons and producing hydrogen ions, which cross the electrolyte membrane. Then, the voltage is driven by the migration of electrons through the electrical circuit to the cathode to react with hydrogen ions and oxygen to produce water. This system can treat waste-water into clean water and/or release hydrogen as fuel [10]. Biochemical energy harvesting devices are also promising green technology by pollution control. Yet, several improvements for this system are still required. The performance is limited by a low output voltage, a lack of transmission of electrons from the anode to the cathode, the frequent replacement of the cathode, as well as its poor reliability and its limited lifetime.

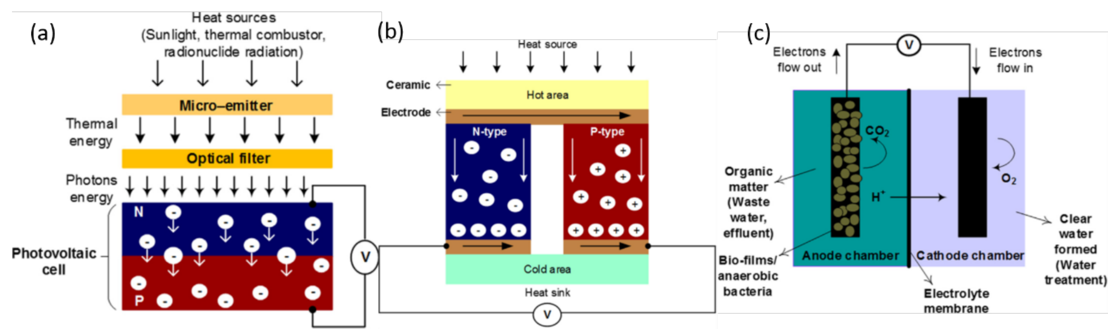

Figure 1-1: working principle of a): thermo-photovoltaic conversion, b): thermoelectric generator, c): microbial fuel cell. From [10]

1.1.4. Mechanical

Kinetic-to-electricity transduction mechanisms are based on several working principles: electromagnetic, electrostatic, triboelectric or piezoelectric energy harvesting devices. They are based on simple mechanisms that can be easily implemented. The working principle of such system is detailed in the next section. The main advantages are the omnipresence of sources of vibration, the broad frequency-range and the high voltage-output [8]. They are all based on moving blocks generating an alternative current (AC) that requires a conversion to a direct current (DC) to store the energy harvested, generally decreasing the performance of the energy harvesting device. Such systems are limited by the amount of applied strain, the high device impedance, the small bandwidth range and the cracking/failure of materials due to the lack of reliability of the moving blocks.

The Table 1.1 summarizes the different energy harvesting mechanisms, the approximate power density generated, the pros and cons and some potential applications. The different harvesting principles present important differences for the approximate power density exhibiting a larger power density for the solar and the mechanical energy transducers. As the solar transducers are limited to radiative environments, the scavenging of energy based on recurring mechanical vibrations is a privileged route to empower wearable or stand-alone devices.

Table 1.1: Comparison of different kind of energy harvesting mechanisms [8], [10].

Energy source	Solar	Thermal	Mechanical	Biochemical
Harvesting principle	Photovoltaic	Thermoelectric	Electromagnetic Electrostatic Piezoelectric	Biochemical reactions
Approximate power density	5-30 mW cm^{-2}	0.01-0.1 mW cm^{-2}	10-100 mW cm^{-2}	0.1-1 mW cm^{-2}
Pros	DC & high power output Mature technology Long life time	DC output, high reliability, no moving blocks, easy scalable, recycle wasted heat energy	Ubiquitous and abundant source, small size, high output voltage, simple mechanism	Environmentally friendly, exploit organic wastes, clean energy, abundant in biological entities
Cons	Limited solar radiation exposure	Low efficiency, large size, heat extinction, large thermal gradient required	Limited strains, high device impedance, mechanical reliability, low operating frequency, not continuous AC output	Low power output, low efficiency, limited lifetime, frequent replacement of the cathode
Potential Applications	Residential powering, remote sensing, environmental monitoring	Coolers, wearable biomedical devices, biometric sensor, vacuum gauge	Wearable systems, bio-chemical and medical devices, orthopedic implant micro-pump	Bio-sensors, hydrogen fuel production, waste water treatment

1.2. Mechanical energy harvesting

The working principle to transduce the mechanical energy into electricity can be classified into four categories depending on the used physical properties: electromagnetic, electrostatic, triboelectric and piezoelectric.

1.2.1. Electromagnetic

The working principle of electromagnetic devices is based on the Faraday's law of electromagnetic induction. The time rate variation of the magnetic flux in the circuit induces an electromotive force [12] (i.e. the voltage). A coil of wire of multiple turns is usually used to

represent the circuit. The variation of magnetic flux comes typically from a rotation or a linear movement of a permanent magnet as described in Figure 1-2 [13]. This energy harvesting system has a resistive impedance. The advantages are the high efficiency and easily scaling up. The drawbacks are the requirement of heavy magnets, expensive materials, the low impedance, and the low output voltage for the small scale devices [8].

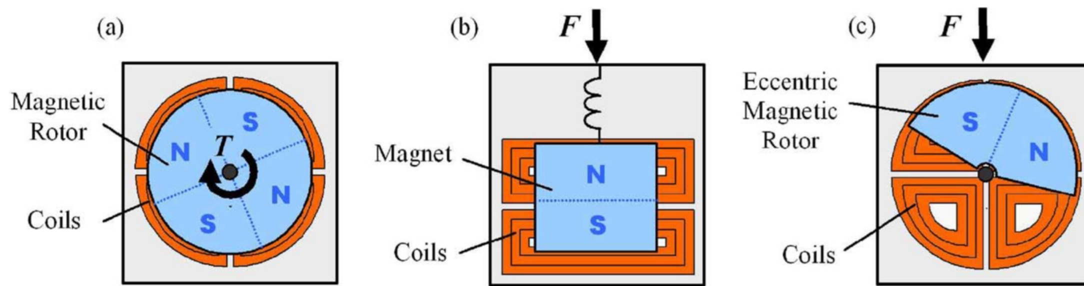

Figure 1-2: Working principle of different electromagnetic energy harvesting devices: a) rotational movement of the magnet, b) magnet oscillation from a vibrational force, c) excentric magnet converting linear vibration into rotational motion, from [13].

1.2.2. Electrostatic

The working principle of the electrostatic energy harvesting devices is mostly based on an electrostatic induction. One or several moving parts of the device lead to a variation of capacitance between two materials [14] (i.e. electrodes). This variation of capacitance creates an electrical work and a charge displacement. The change of capacitance with a mass-proof is also used in electrostatic accelerometers. Several configurations are possible and are conventionally called *out-of-plane gap closing, in-plane overlap varying and in-plane gap closing*, as described in Figure 1-3. Other geometries are also possible for the overlapping parts. In any case, there is no contact between the moving parts. Creating a bias potential between moving parts is a typical approach to increase the performance. Examples of sources of bias potential are: difference of work function, floating electrodes charged by tunneling and electrets. Electrets are dielectric materials electrically-charged and –polarized, where a net amount of charge is trapped [15]. The electrostatic energy harvesters with bias voltage have the same kind of conversion design, as described in Figure 1-3 [14]. Advantages are the low cost and the lightweight of devices, while the drawbacks are the low performance, the electrical pre-charge required and the high matching impedance of the electrostatic harvesters [8].

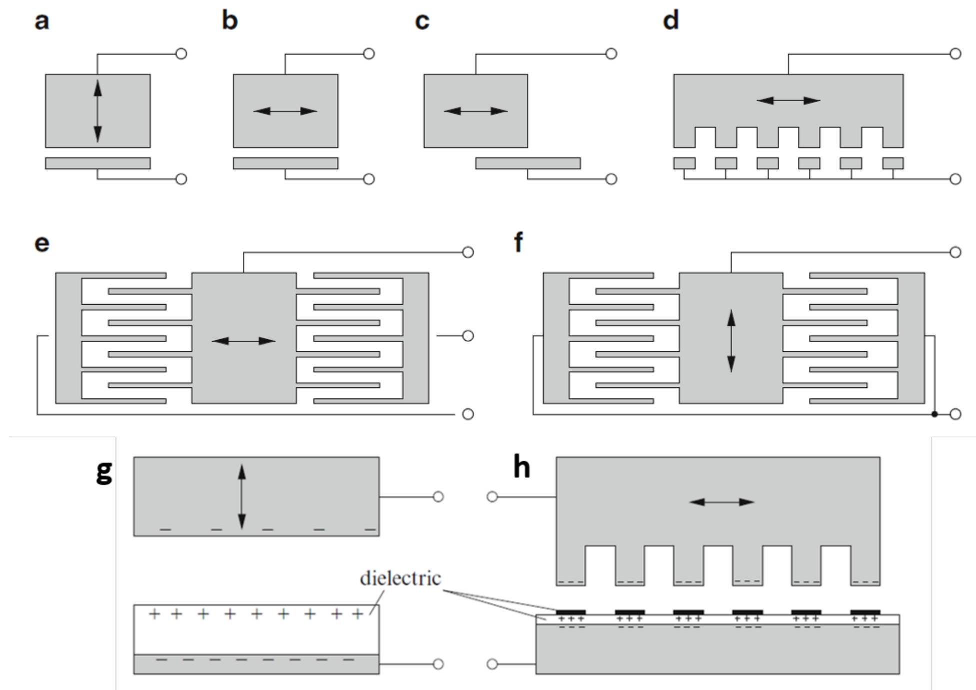

Figure 1-3: Electrostatic energy harvesting design based on a proof-mass motion inducing a variation of capacitance: a) out-of-plane gap closing, b,c,d,e) in-plane overlap varying, f) in-plane overlap closing, g) out-of-plane gap closing with electrets, h) in-plane overlap varying with electrets, from [14]

1.2.3. Triboelectric

Triboelectric energy harvesters, also called triboelectric nanogenerator (TENG), are a recent kind of energy harvesting devices based on an electrostatic induction, like the electrostatic energy harvesters, or on contact electrification [8]. In 2012, the first TENG with a contact electrification was demonstrated [16]. The working principle is based on two polymers films with different electron-attracting abilities. Each polymer has a back electrode as shown in the Figure 1-4a. The roughness of the polymer films generates opposite sign charges at the interface for each polymer when they contact through a friction. When the two films contact and separate, an electric potential appears and drives the charges generated in an external load [4], [17]. After a few years of development, TENGs work with four different fundamental modes: *out-of-plane contact-separation, in-plane linear sliding, single-electrode mode and freestanding triboelectric-layer*, as described in Figure 1-4b. These working modes look similar to the electrostatic ones but a main difference is the contact mode, forbidden for the electrostatic harvesters. TENGs have the advantage to be low-cost, low-weight, with a simple fabrication, and to have a large output and a high efficiency at low frequency. The drawbacks are the pulsed output, the low durability (i.e. lifetime) and the high matching impedance [8].

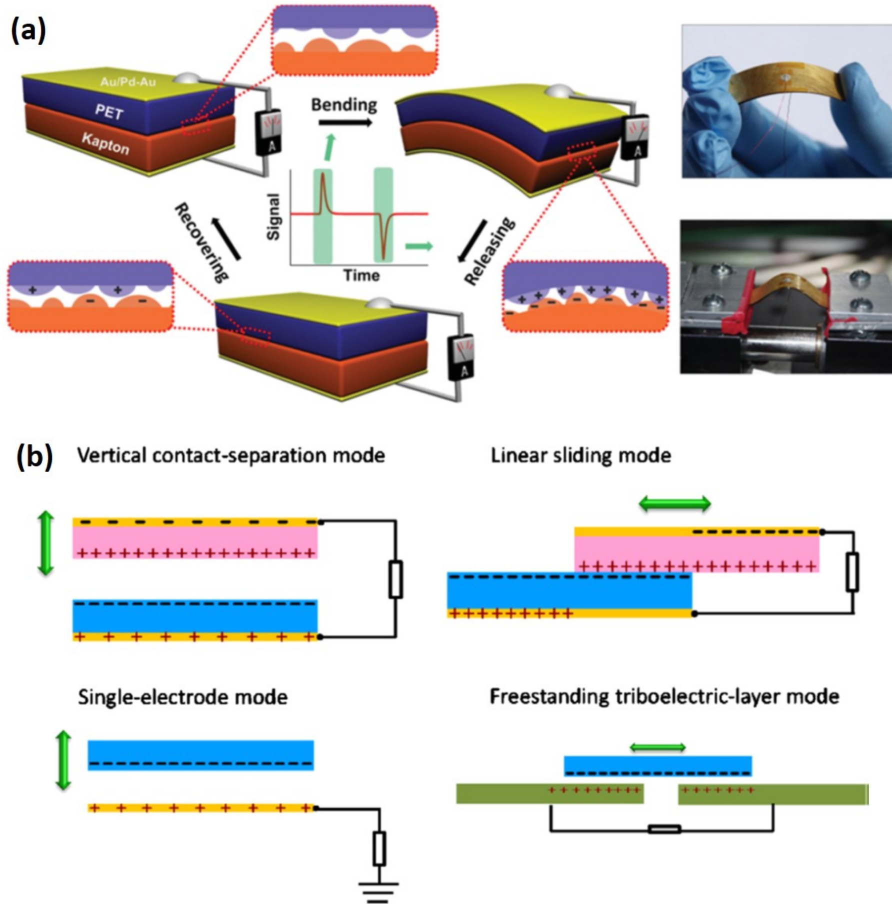

Figure 1-4: a) working principle of the first triboelectric nanogenerator, from [17] b) four fundamental designs of TENGs [8].

1.2.4. Piezoelectric

Piezoelectric harvesters are based on piezoelectric materials that transduce mechanical stress or strain into a difference of voltage at its boundaries. The different kind of piezoelectric devices, materials and the origin of piezoelectricity will be discussed in more detail in the next section. There are two main ways to harvest mechanical energy source with piezoelectric materials: *"inertial"* and *"kinematic"* [19], [20]. The inertial energy harvesting is based on a mass-spring system that is subjected to a vibration at a specific frequency. This system is generally composed of a cantilever with a piezoelectric film with a mass-proof at its extremity, as described in Figure 1-5a. When the whole system is vibrating at a small amplitude and specific frequency, the cantilever starts to oscillate at its resonance frequency. It amplifies the small ambient vibration into a strain governed by the Euler-Bernoulli beam equation [21]. The advantage of this system is the amplitude of vibration of the cantilever that can be

significantly larger than the mechanical amplitude of the environment. Several designs for the cantilever are possible with the piezoelectric material. Two different examples are shown in Figure 1-5b. The kinematic energy harvesting device is directly coupled with the mechanical energy source, as described in the example of the in Figure 1-5c where the ambient stress/strain is applied on the piezoelectric material. The advantages are the easily scaling down and integration to the microelectromechanical system (MEMS) scale, the low cost and the almost facile use into high vibrational frequency regime (i.e. around kHz) [21]. The drawbacks are the low output voltage and a pulsed output that require a specific and complex electronic signal treatment.

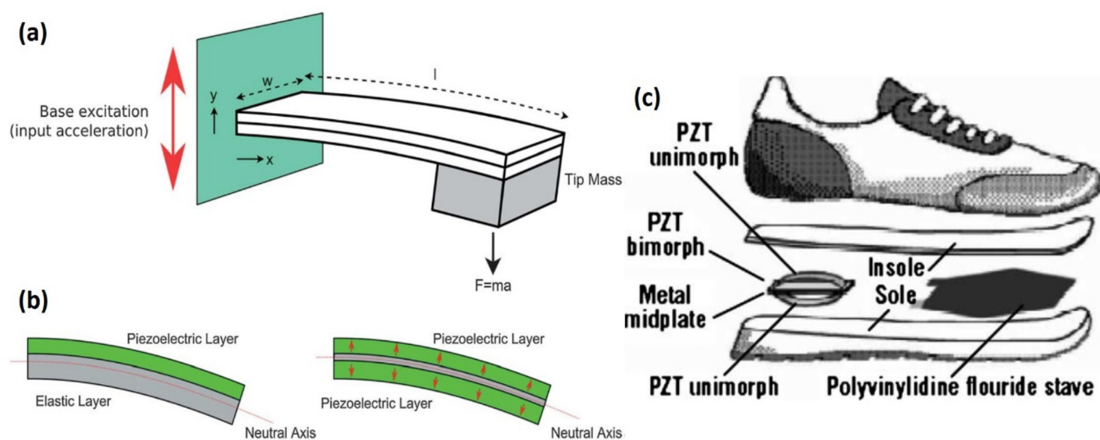

Figure 1-5: a) schematic inertial piezoelectric energy harvesting device based on a cantilever beam structure, b) cantilever beam design with a unimorph and bimorph structure [19] *, c) kinematic piezoelectric energy harvesting device* [21].

The Table 1.2 summarizes the different kinetic-to-electric energy harvesting mechanisms, type of impedance and the pros and cons. A comparison of their approximate power density is not possible regarding the scaling effect on the output power as function of the *"effective material volume"* [21], *V*. For example, the output power of the electromagnetic and piezoelectric conversion is proportional to V^2 and $V^{4/3}$, respectively [22]. Thus, at a dimension lower than mm^3, piezoelectric conversion exhibits a power density larger than electromagnetic conversion.

Table 1.2: Comparison of different mechanical energy harvesting mechanisms. From [8] &[21]

Mechanical energy harvesting	Electromagnetic	Electrostatic	Triboelectric	Piezoelectric
Harvesting principle	Electromagnetic induction	Electrostatic induction	Contact electrification & electrostatic induction	Piezoelectric effect & electrostatic induction
Impedance type	Resistive	Capacitive	Capacitive	Capacitive
Pros	High efficiency, easy to scale up	Light weight, low cost	Large output power, low weight, low cost, simple fabrication	Easy to scale down to nanoscale, low cost, large frequency range
Cons	Expensive heavy magnet, low output for small-scale	Pre-charge required, low output, high impedance matching	Pulsed output, low durability, high impedance matching	Low & pulsed output, high impedance matching

1.3. Piezoelectric energy harvesting devices

The history of piezoelectricity started in 1880. The French Curie brothers discovered the direct piezoelectric effect when they observed an electrification in response to an applied mechanical stress on some crystals (Figure 1-6a). They noticed it was somewhere linked with the symmetry of the crystal. Then, the Luxembourg-born Gabriel Lippmann deduced mathematically the fundamental thermodynamic principle of the converse piezoelectric effect, i.e. a stress or strain in response to an applied electric field (Figure 1-6b). When Voigt published his work about physical crystallography, the piezoelectric effect was described and linked to different crystallographic classes [23]. The piezoelectric coupling is described by a linear relationship between the electric displacement ***D*** or the electric field ***E*** and the stress ***T*** or strain ***S***. Thus, the piezoelectric behavior can be written as [24]:

$$D_i = d_{ijk}T_{jk} \quad \text{or} \quad D_i = e_{ijk}S_{jk} \,, \qquad (1)$$

$$S_{ij} = d_{kij}E_k \quad \text{or} \quad T_{ij} = -e_{kij}E_k \,, \qquad (2)$$

with ***d*** and ***e*** piezoelectric coefficient matrix (i,j,k = 1 to 3). Equations (1) and (2) represent respectively the direct and the converse piezoelectric effect. The ***d*** and ***e*** coefficients are linked with each other through the stiffness of the material. Combining this with the Hooke's law, the two following constitutive equation are used to describe the piezoelectric effect [25]:

$$T_p = c_{pq}^E S_q - e_{kp} E_k \quad (3)$$

$$D_i = e_{iq} S_q + \varepsilon_{ik}^S E_k \quad (4)$$

with $\boldsymbol{c}^{\boldsymbol{E}}$ elastic stiffness matrix at fixed ***E***, $\boldsymbol{\varepsilon}^{\boldsymbol{S}}$ dielectric permittivity matrix under constant strain. ***T, S, E*** and ***ε*** are second-rank tensors, ***c*** is a fourth-rank tensor and ***d*** and ***e*** are third-rank tensors, reported to a matrix notation for simplification with the Voigt notation. For symmetry reasons, all components of the piezoelectric tensor cancel in crystals with a center of symmetry. In the 32 crystal classes, 21 are non-centrosymmetric and 20 exhibit piezoelectricity. Among those 20 piezoelectric crystal classes, 10 point groups exhibit a unique polar axis leading to pyroelectricity. Pyroelectric crystals possess a non-null dipolar moment that increases when a variation of temperature is induced. If an external electric field can reverse the spontaneous polarization of a crystal through a hysteresis curve, then this crystal is defined as ferroelectric, as described by the Figure 1-6c.

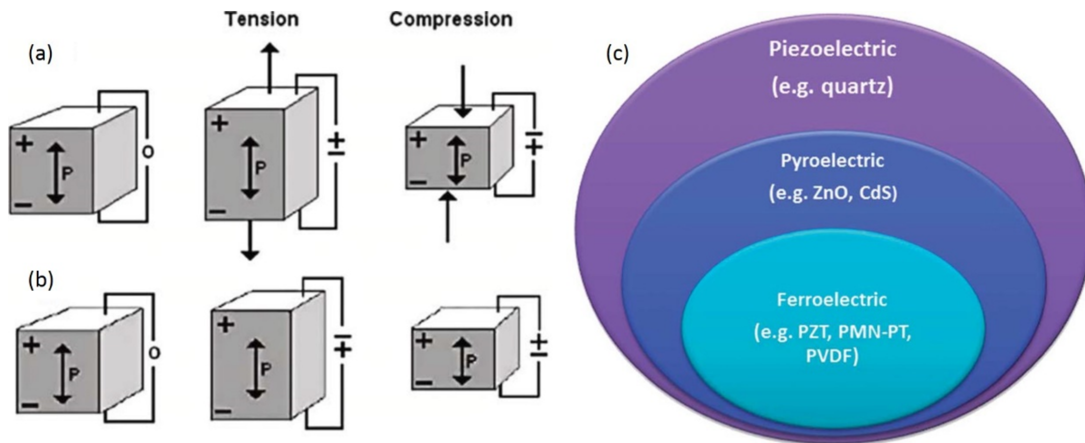

Figure 1-6: Schematic representation of the a) direct piezoelectric effect, b) transverse piezoelectric effect [23], *c) crystallographic classification of the piezoelectric, pyroelectric and ferroelectric materials* [19].

The absence of center of symmetry is therefore mandatory for a material to exhibit a piezoelectric effect but not sufficient to show a large piezoelectric behavior for devices applications. Knowing the symmetry of the crystal does not allow to determine the value of the piezoelectric coefficients, but helps to design the piezoelectric device due to the piezoelectricity anisotropy. The difference of values of piezoelectric coefficients with the orientation of the major piezoelectric materials is reported in the Table 1.3.

Table 1.3: Dielectric, piezoelectric, pyroelectric and mechanical properties of some common piezoelectric materials and nanowires and their symmetries [19] & [23].

Material	α-quartz	GaN	AlN	ZnO	$BaTiO_3$	PZT	PMN-PT	$LiNbO_3$	PVDF
Symmetry	32	6mm	6mm	6mm	4mm	3m/ 4mm	4mm	3m	-
Type	Piezo	Pyro	Pyro	Pyro	Ferro	Ferro	Ferro	Ferro	Ferro
ε^S_{33}	4.63	11.2	10	8.84	910	1470	680	27.9	5-13
ε^T_{33}	4.63	-	11.9	11	1200	3400	8200	28.7	7.6
d_{33} (pC N^{-1})	d_{11} = -2.3	3.7 13.2 (NW)	5	12.4 14-26 (nanobelt)	149	593	2820	6	-33
d_{31} (pC N^{-1})	-	-1.9 -9.4 (NW)	-2	-5	-58	-274	-1330	-1	21
d_{15} (pC N^{-1})	d_{14} = 0.67	3.1	3.6	-8.3	242	741	146	69	-27
Coef Pyro ($\mu Cm^{-2}K^{-1}$)	-	4.8	6-8	9.4	200	260	1790	83	33
s^E_{11} (pPa^{-1})	12.77	3.326	2.854	7.86	12.3	16.4	69	5.83	365
s^E_{33} (pPa^{-1})	9.73	2.915	2.824	6.94	15.5	20.8	119.6	5.02	472

Beside the properties of piezoelectric materials, the energy source is determining the design of piezoelectric harvesters. As briefly explained before, a resonant structure like piezoelectric cantilevers is the best design for an inertial energy harvester (i.e. continuous vibrational source). The best suitable piezoelectric material configuration in that case is a film (Figure 1-5). The main thin films materials exhibiting valuable piezoelectric coefficient are those in Table 1.3, as AlN and PZT ($PbZr_xTi_{1-x}O_3$). Various techniques process those materials controlling their crystalline orientation, like pulsed laser deposition, sputtering, sol-gel, chemical vapor deposition, spray pyrolysis and hydrothermal synthesis. Piezoelectric cantilever energy harvesters are studied, developed and well-known since many years [20], [26]. Some recent small-scale devices are compared in the Table 1.4. The performance can be easily compared with a normalized volumetric power density. Piezoelectric cantilever devices based on AlN

and PZT exhibit the same range of output, even though the piezoelectric coefficient of AlN is by more than one order of magnitude smaller than PZT (Table 1.3). AlN devices exhibit higher output voltage with less dielectric loss compared to PZT [27]. Piezoelectric coefficient of AlN and ZnO are close but there is no current interest in ZnO cantilevers. Indeed, AlN is preferred rather than ZnO in the microelectronic industry because of its better chemical stability and its CMOS compatibility for integration with electromechanical systems [28].

Table 1.4: Comparison of different small scale piezoelectric cantilever energy harvesters from [21].

Reference	Active material	Active area, mm^2	Active volume, mm^3	Accele-ration, g	Frequency, Hz	Power, µW	Norm. area power density (µW mm^{-2} Hz^{-1} g^{-2})	Norm. volum. power density (µW mm^{-3} Hz^{-1} g^{-2})
Muralt et al. (2009)	PZT, d_{33}	0.96	0.48	2	870	1.4	4.19×10^{-4}	8.38×10^{-4}
Hajati and Kim (2011)	PZT, d_{33}	120	0.02	4	1300	22	8.81×10^{-6}	5.29×10^{-2}
Morimoto et al. (2010)	PZT, d_{31}	76.5	4.05	0.5	126	5.3	2.20×10^{-3}	4.15×10^{-2}
Lee et al. (2009)	PZT, d_{31}	4.5	0.452	2.5	256	2.76	3.84×10^{-4}	3.82×10^{-3}
Defosseux et al. (2012)	AlN, d_{31}	3.57	2.8	0.275	214	0.63	1.09×10^{-2}	1.39×10^{-2}
Hirasawa et al. (2010)	AlN		1.63	1	857	0.18		1.29×10^{-4}
Elfrink et al. (2010)	AlN		15	0.2	599	69		1.92×10^{-1}

The kinematic harvesters are based on an intermittent source of vibration, the most widespread energy source for portable wearable devices. These harvesters require a specific design to optimize the transduction of the ambient stress/strain relying on the piezoelectric material (Figure 1-5c). Large strain/stress can be applied on such devices. Unfortunately, most of the materials exhibiting a high piezoelectric transduction are stiff and brittle (e.g. ZnO, GaN, AlN, PZT,… Table 1.3). Soft materials like PVDF are more suitable for this kind of applications, but the low values of piezoelectric coefficients limit the performance. Ten years ago, the emergence of composite materials based on nanostructures started as an alternative to increase the performance [5], [29]. Now, many flexible and stretchable devices based on piezoelectric nano-materials have been reported to show interesting performance by improving the brittleness and stiffness of inorganic piezoelectric materials. A device based on piezoelectric nanostructures is called a piezoelectric *"nanogenerators"* (PENGs). Three kinds

of PENGs exist: ZnO nanowire-based PENGs, polymer-based PENGs and perovskite ceramic-based PENGs (Figure 1-7). Composite-based PENGs are easily processed, cost-effective and exhibit high output-values [5]. The main advantage of a PENG is the larger stress/strain applied on the piezoelectric material leading to a considerable increase of the performances compare to the kinematic harvesters based on thin films or bulk piezoelectric materials. Improvements of PENGs are focusing on lead-free material, larger performance and longer life cycles [5]. To our knowledge, a reliable quantitative comparison of the performance of this emerging technology relying on the rationale design of devices is not available. Among the PENG architectures, the one based on ZnO nanowires is intensively studied and is the scientific and technology background of this PhD thesis.

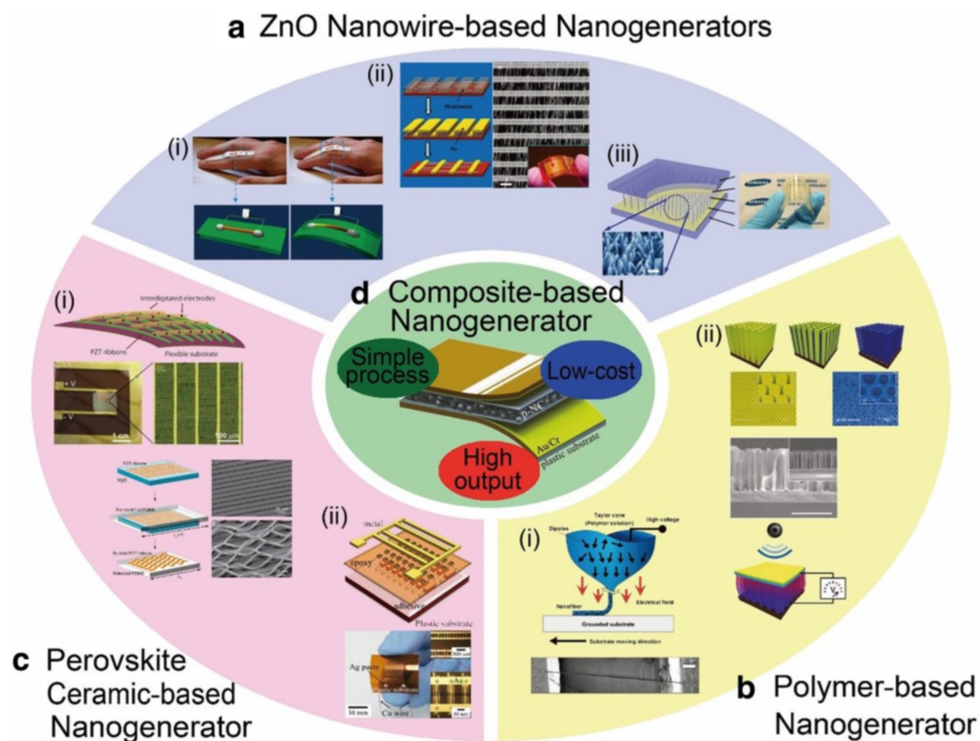

Figure 1-7: Piezoelectric nanogenerators based on a) ZnO nanowires, b) PVDF polymer, c) perovskite ceramic nanostructures from [5].

1.4. Nanogenerators based on ZnO nanowires

1.4.1. Working principle

The concept of piezoelectric nanogenerator emerged from the piezoelectric characterization of a single ZnO nanowire with an AFM tip by Z.L. Wang *et al.* in 2006 [29]. ZnO is piezoelectric in its wurtzite crystalline structure as shown in Figure 1-8a. The asymmetry of the unit cell drives the piezopotential under a compression or a tension of the material (Figure 1-8b). For a single crystalline nanowire uniaxial compressed or stretched, the piezopotential is linearly distributed along the c-axis. In the work of Wang *et al.*, ZnO NWs are grown on sapphire using a vapor-liquid solid (VLS) method with gold nanoparticles as catalyst remaining at the top of the ZnO NWs. The conductive Pt-coated AFM tip is slowly moving to bend the ZnO NW. First, a Schottky contact is formed at the Pt-ZnO interface as represented in Figure 1-8d when the tip contacts the NW. Then, the bending on the NW is driving an asymmetric piezopotential, changing the profile of the conductive band. The behavior is considered as a reverse-biased Schottky diode. From this positive piezopotential, a slow-flow of electrons accumulates charges in the tip. Then, the tip is scanning across the NW to the negative piezopotential, resulting in a back flow of the charges previously accumulated in the tip. At the end, the tip reaches the negative piezopotential. If this piezopotential is large enough, charges from the n-type ZnO can flow to the tip and an output voltage of 10 mV is measured. The behavior is considered as a forward biased Schottky diode [30]. This mechanism was strongly debated due to the confusion between the measurement of an open circuit voltage and an explanation based on a current flow [31]. Alexe *et al.* showed a similar output voltage measurement on Si NWs due to a fast change of impedance when the contact was made and lost between the tip and the Si NW. These works laid the foundation of the piezotronic effects applied to energy scavenging.

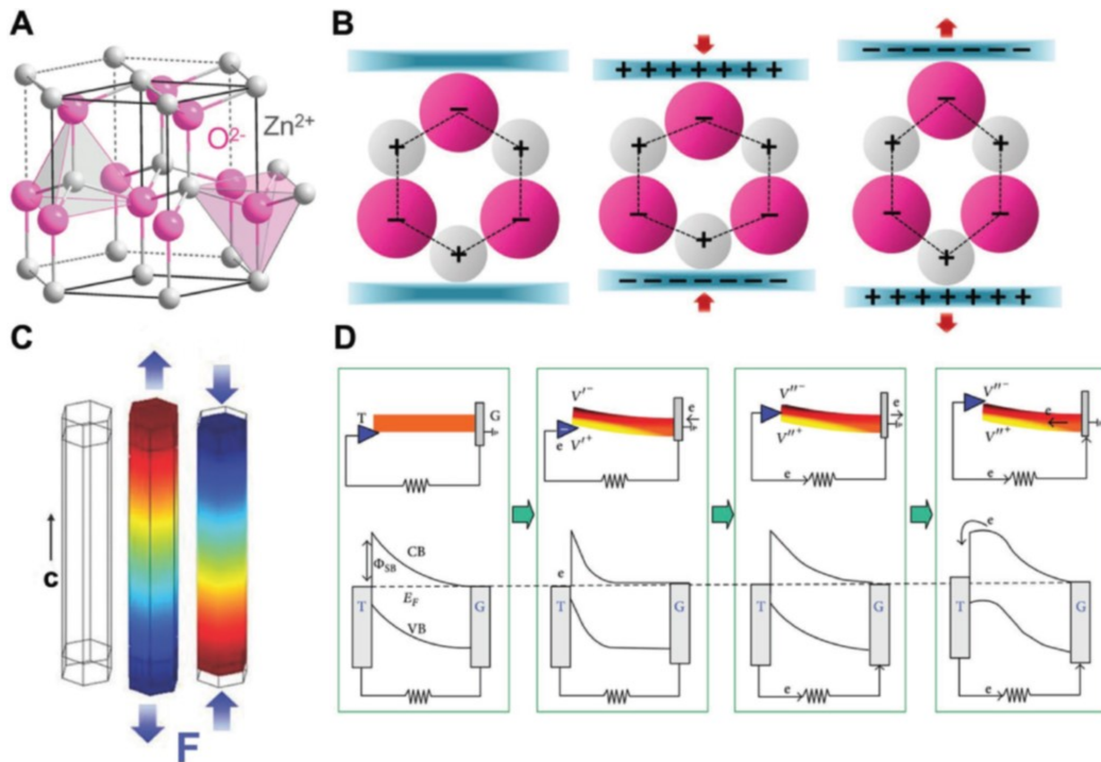

Figure 1-8: a) Atomic model of wurtzite ZnO. b) Different state of polarization and piezopotential of the material under tension and compression. c) Numerical visualization of the piezoelectric potential distribution in a ZnO nanowires under uniaxial stress. d) Band diagram behavior of the bended ZnO nanowire with a conductive AFM tip from [4].

Despite the still controversial debate about the working principle, many demonstrators of PENG based on ZnO were successfully fabricated. X. Wang *et al.* reported the first PENG based on ZnO nanowires [32]. Ultrasonic waves drive the mechanical solicitation of ZnO NWs as shown in Figure 1-9. The same working principle as previously used for the AFM tip is used to explain the observed behavior. A Pt-coated zigzag electrode shakes and bends ZnO NWs. Some other NWs can vibrate at their resonance and touch the electrode or can be compressed (Figure 1-9g). A maximum current of 0.5 nA and a maximum output voltage of 1 mV are measured (Figure 1-9i). The performance is low because of the limited amount of active NWs touching the electrode. A large majority of ZnO NWs does not produce electricity because of their non-uniformity of height, width and density decreasing significantly the yield of the devices when considering the volumetric output power.

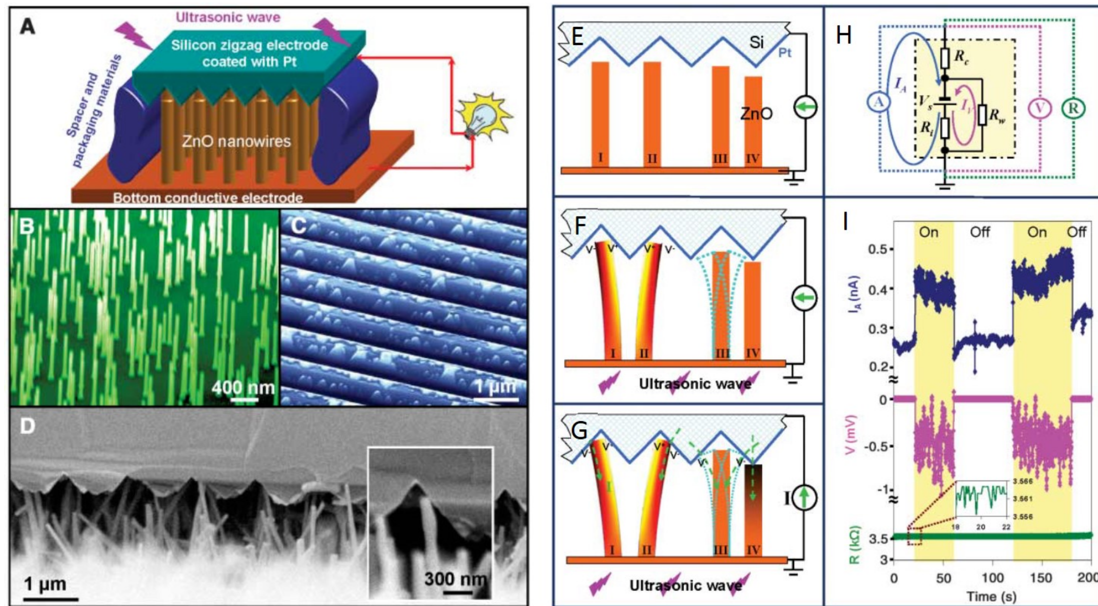

Figure 1-9: PENG based on ZnO nanowires driven by ultrasonic waves. a) Sketch of the device based on vertical ZnO NWs grown on a conductive substrate and covered with a zigzag top electrode. b) Aligned vertical ZnO NWs grown by VLS method. c) Zigzag electrode based on etched Si and coated with 200 nm Pt. d) Cross section SEM image of ZnO NWs in contact with the Pt zigzag electrode. e) Schematic view of the ZnO NWs at initial state. f) Ultrasonic waves create a piezopotential but without charges harvested because of the reverse biased Schottky contact at the ZnO/Pt interface. g) Ultrasonic waves create a piezopotential with charge harvested because of forward-biased Schottky contact leading to a current generated. h) Equivalent circuit model of the PENG with the setup measurement. i) Measurement of the current, output voltage and the resistance of the device as shown in (h) when the ultrasonic waves are on and off, from [32].

Beside this early device, other growth and transferable techniques allowed to use flexible substrate, in order to increase the strain applied on ZnO NWs. Based on this, there are three main kinds of ZnO PENGs: a first based on *lateral ZnO nanowires*, a second based on *vertical ZnO nanowires*, and a third based on *ZnO fiber structures*.

1.4.2. Lateral ZnO nanowires

Yang *et al.* reported the first example of a PENG based on a single ZnO NW [33]. The ZnO NW is laterally fixed with electrodes at each end on a flexible substrate (Figure 1-10a). The bending and unbending of the substrate fixed on a finger induces a cyclic uniaxial tensile strain in the NW. It generates a piezopotential between the ends of the ZnO NW. Positive and negative output voltages are measured for the bending and releasing of the substrate in open circuit (Figure 1-10b). Harvesting an intermittent "biomechanical" energy was demonstrated with this PENG on a finger bending, a running hamster or on a heart of a rabbit [33]. To further increase the output power, Xu *et al*. fabricated an array of laterally well aligned and c-axis oriented ZnO NWs. The array is composed of 700 rows with approximately 20000 lateral NWs as shown in Figure 1-10c,d. This PENG architecture generates a maximum output voltage pulse

of 1.2 V and a maximum current pulse of 26 nA under a controlled strain of the flexible substrate [34]. Zhu *et al.* developed another approach called the *sweeping-printing-method* to reach higher performance. First, ZnO NWs are grown vertically on a stiff substrate. Then, NWs are transferred laterally to a flexible substrate by sweeping, brushing the stiff substrate. Finally, gold electrodes are deposited by photolithography to connect NWs together (Figure 1-10e,f). An open-circuit voltage of 2 V and short-circuit current of 100 nA are measured under a strain of 0.1 % leading to a maximum area power density[2] of 22 µW cm^{-2}. A rectifying bridge is used to store the electrical energy generated by the PENG in a capacitor to light up a LED [35] (Figure 1-10g). Another process was developed by Hu *et al.* with conical ZnO wires. The conical wires are dispersed on a polymer and a thin layer of polymer is spin-coated. This step is being repeated several times. The result is a composite material composed a laterally aligned ZnO conical wire in a dielectric polymer (Figure 1-10h). The device produces an output voltage of 2 V under a compressive strain of 0.11 %. This PENG is able to drive a commercial LCD [36]. This last PENG device has a simple fabrication, is cost-effective and easily scalable for self-powered devices. One major limitation of the PENGs based on lateral ZnO NWs is the limited strain transferred to ZnO NWs due to its still high stiffness compared to the flexible substrate limiting the bending to 6 %.

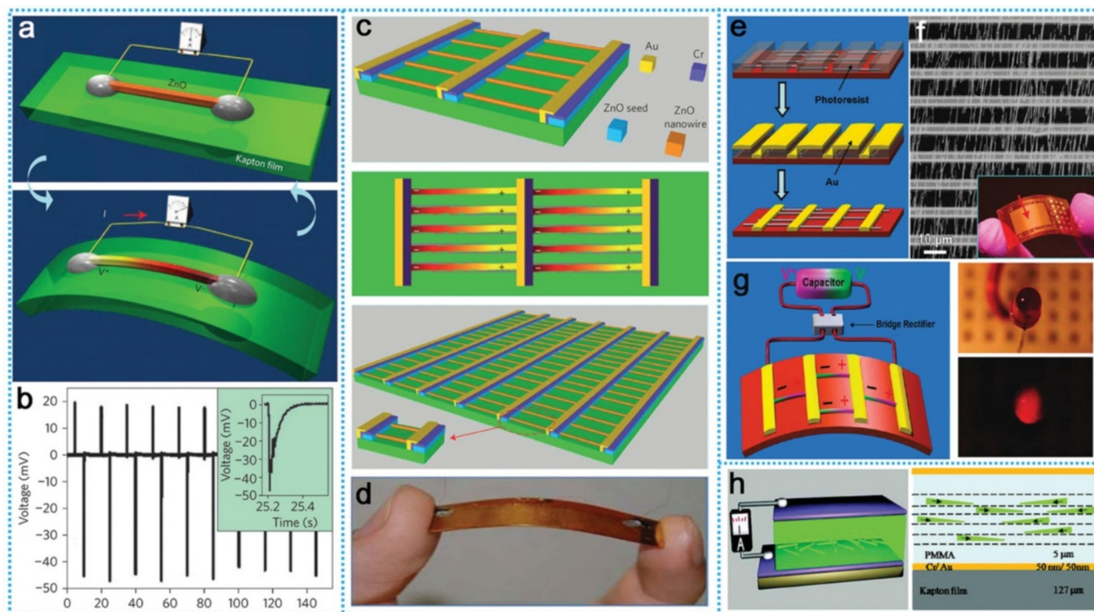

Figure 1-10: PENGs based on lateral ZnO NWs. a,b) Schematic and working principle of a single ZnO NW. The mechanical bending and unbending of the flexible substrate generate a piezopotential. c,d) Schematic of lateral ZnO NWs array on flexible substrate. e-g) Schematic and picture of the sweeping-printing fabrication of lateral ZnO NWs PENG able to light up a LED. h) Schematic of conical ZnO wires drop casted with PMMA to form a composite PENG from [17].

[2] The very definition of this power can be disputed as we will be discussed later

1.4.3. Vertical ZnO nanowires

As mentioned previously, the bending of the flexible substrate for lateral ZnO NWs PENG is limited. Using vertical ZnO NWs bypass this limitation to obtain a fully flexible device. A simple way to grow vertical ZnO NWs is the use of the solution-based wet chemistry method [37]–[44]. The NW arrays can be synthetized at 80°C on various substrates. A sputtered seed layer can control the uniformity and the polar orientation of the NWs. This fabrication technique provides a low cost material and a large scale approach for PENGs. Xu et al. reported the first PENG based on vertical ZnO NWs. Aspect ratio and density are approximately controlled and the polar axis of all NWs is well oriented. A polymer is spin-coated between the NWs to increase the robustness of the device. Then, a Pt top electrode forms a Schottky contact with ZnO NWs and a uniaxial stress is applied on it. An open circuit voltage and a short circuit current of 90 mV and 6 nA are improved by a serial and parallel connection of several devices [34]. Three devices connected in serial give a voltage of 243 mV and in parallel a current density of 18 nA cm^{-2} leading to a power density[3] of 2.7 mW cm^{-3}. Choi *et al.* fabricated a fully flexible PENG based on ZnO NWs with graphene electrodes (Figure 1-11a-c). The mechanical reliability for large strain is demonstrated by cyclically rolling the device (Figure 1-11c). The PENG exhibits a current density of 2 µA cm^{-2} but without any mention of an output voltage or power [45]. Lee *et al.* also confirm the possibility of a super-flexible PENG based on vertical ZnO NWs. In this fabrication process, ZnO NWs are totally encapsulated between dielectric polymers (PMMA). The substrate, acting as bottom electrode, and the top electrode are ultrathin layers of aluminum (Figure 1-11d). The output voltage of this PENG architecture, harvesting energy from a waving flag, is shown in Figure 1-11e. It demonstrates a high flexibility and conformability by also detecting the wrinkling of a human face. A maximum output voltage and current of 0.2 V and 2 nA are measured. This PENG can be used as a self-powered deformation sensor [46]. In order to drastically increase the performance, Hu *et al.* focused on pretreatment method of ZnO NWs. Vertical ZnO NWs are grown by wet chemistry method on both side of a polymer substrate (Figure 1-11f,g). Some polymers passivate the surface of the NWs, increasing the open circuit output voltage to 20V. This PENG is able to output a regulated voltage of 1.8 V with a constant current through a convertor, enough to power on an electronic watch [47].

[3] The very definition of this power can be disputed as we will be discussed later

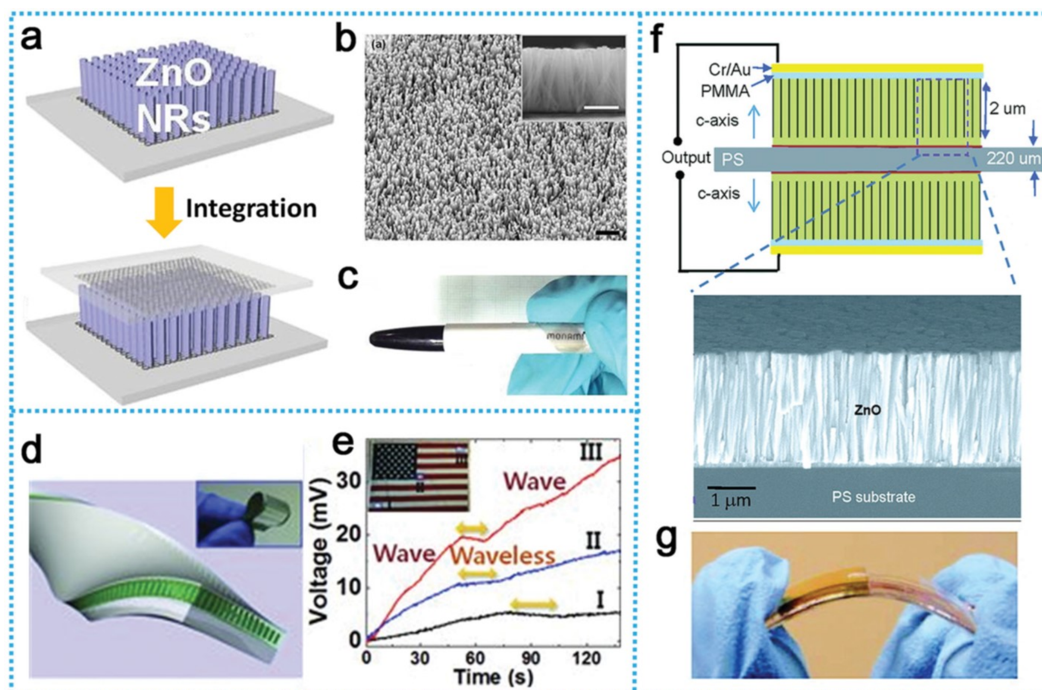

Figure 1-11: PENGs based on vertical ZnO NWs. a-c) Fully flexible PENG with ZnO NWs and graphene electrodes. d,e) Ultrathin Al substrate for highly flexible PENG to harvest energy from a waving flag. f,g) High output PENG with a bilayer of ZnO NWs from [17].

1.4.4. ZnO fiber structures

The relative easy wet chemistry processing of ZnO NWs allows to grow on various substrates, such as metals, polymers or curved substrates. Fibers are a good example of 3D substrates in the perspective of wearable self-powered devices in clothes. For this, Qin et al. demonstrated the feasibility with fibers coated with ZnO NWs. The device is composed of two fibers covered by NWs grown by wet chemistry, one with NWs coated by gold (Figure 1-12a,b). The working principle is still based on the Schottky contact between ZnO and gold while NWs are bending and brushing each other [48] (Figure 1-12c). A more reliable PENG based on fibers is developed by Lee *et al*. The fiber is a core-shell with an inner and outer electrode between ZnO NWs encapsulated in a PVDF matrix (Figure 1-12d). This hybrid fiber converts the intermittent and low frequency mechanical energy of the elbow into electricity. Folding and releasing the elbow produces an output voltage, current and power density of 0.1 V, 10 nA cm^{-2} and 16 µW cm^{-3}, respectively[4]. This fiber-based PENG demonstrates the feasibility to power wearable electronics [49]. Li *et al.* increase the performance of the core-shell fibers PENG with a textured ZnO thin film growth by physical vapor deposition (Figure 1-12f). When

[4] The very definition of this power can be disputed as we will be discussed later

the fiber is under pressure (Figure 1-12g), a piezopotential between the inner and the outer surfaces of the fiber is generated. This fiber exhibits an output voltage and a current density of 3.2 V and 0.15 µA cm^{-2}, respectively. This high performance allows to harvest mechanical energy from a small pressure variation, like flowing air and liquid. This fiber-based PENG shows a potential as ultrasensitive pressure sensors for monitoring the human heart [50]. Up to now, several PENGs based on ZnO fibers have been designed and developed on such different working principle to harvest mechanical energy from the human body or air flow [51], [52].

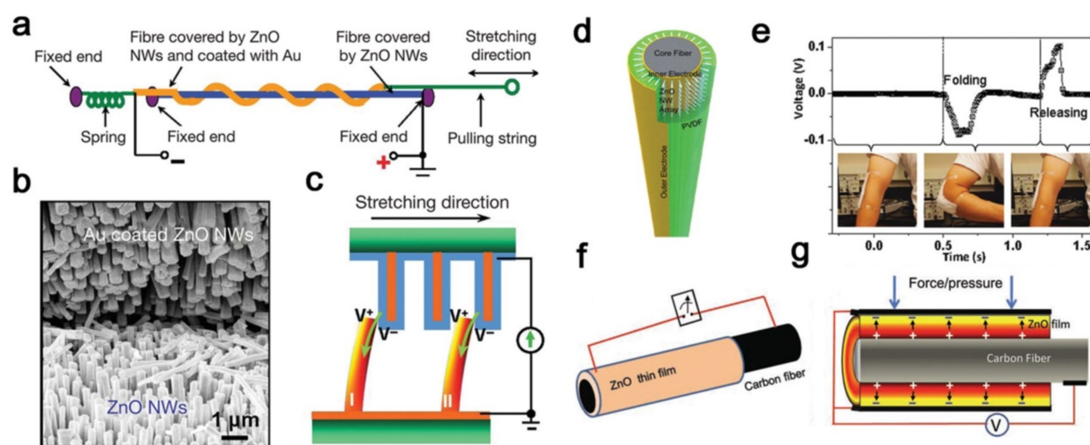

Figure 1-12: PENGs based on ZnO fiber structures. a-c) Schematic, SEM picture and working principle of brush-to-brush ZnO NWs and Au-coated ZnO NWs grown on fibers. d,e) Schematic and output voltage of a hybrid PVDF, ZnO NWs fiber harvesting energy from the elbow folding. f,g) Schematic and working principle of a carbon fiber coated with a ZnO film, from [17].

1.5. PENG performance optimization and characterization

The performance of PENG based on ZnO NWs increased rapidly since the first ZnO NW characterization with an AFM tip. The Figure 1-13 summarizes the evolution of the maximum output voltage measured from the early devices until the elaborated PENG [6]. This increase of the performance of PENGs based on ZnO NWs relied on three features: the increase of the piezopotential generated by the NWs, the optimization of the interface between ZnO and the electrodes, and the optimization the electromechanical coupling factor.

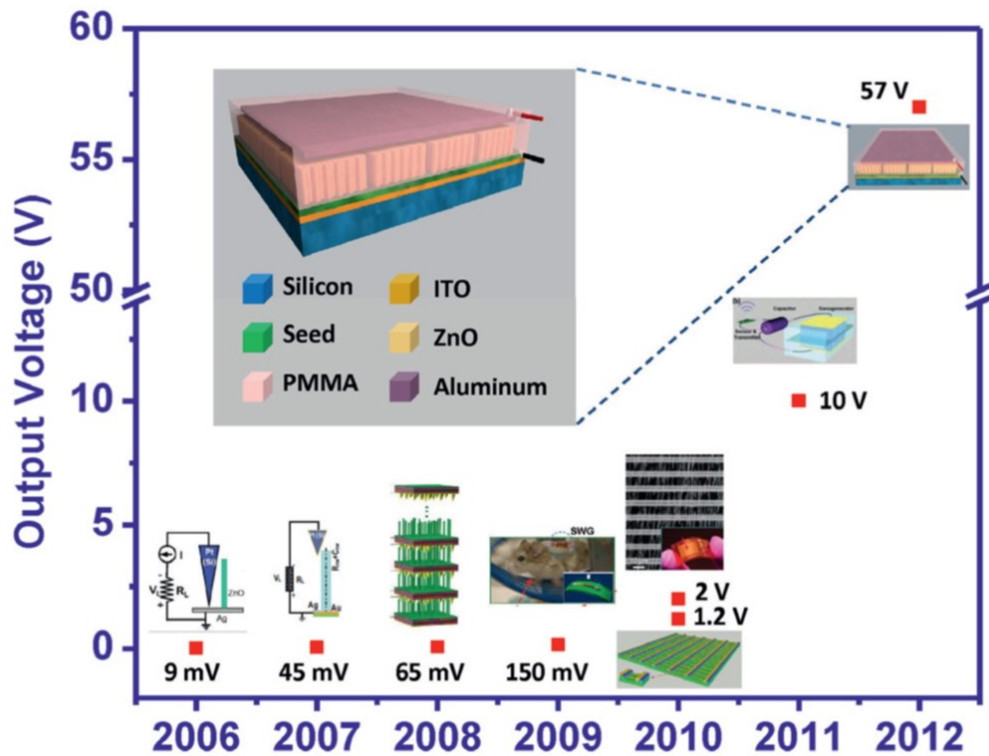

Figure 1-13: Summary of the PENGs from 2006 to 2012. The maximum output voltage in open circuit is reported, from the first characterization of a single ZnO NW bended with an AFM tip to the PENG based on vertically aligned ZnO arrays, from [6].

First, the piezopotential can be tuned with the carrier density of NWs. Generally, ZnO has a high carrier density, which can lead to an internal screening effect. Based on calculation of a bent ZnO nanowire, Shao *et al*. demonstrated a significant decrease of the piezopotential when considering a moderate carrier concentration of 10^{17} cm^{-3}. Above 10^{18} cm^{-3}, the piezopotential is almost completely screened by the redistributed carrier along the NW [53]. As-grown ZnO NWs by wet chemistry method have a typical carrier density of 10^{17} cm^{-3} [54]. Therefore, decreasing the carrier density will increase the output voltage. ZnO is intrinsically n-type. A counter-doping during the growth process with a p-type dopant can reduce the carrier density. Lithium and phosphorous dopants have shown an increase of the piezopotential generated [55], [56]. Even other doping element like silver can increase the PENG performance [57]. Doping ZnO with halogen element like bromine increases the output voltage of the PENG due to a lattice expansion of ZnO [58]. Another source of free carrier in ZnO NWs is provided by some surface-related defects coming from the wet chemistry growth process [59]. A thermal annealing at 350°C for 30 min in air can be used to reduce such intrinsic defects. A surface encapsulation of ZnO NWs with a layer-by-layer polyelectrolyte with poly

(diallydimethylammonium chloride) (PDADMAC) and poly (sodium 4-styrenesulfonate) (PSS) seems even more efficient [47]. Various technique of surface treatment of ZnO NWs can increase the output voltage [59].

Then, after the reduction of the internal screening of the piezopotential, the external screening of the piezopotential should be slow enough in open circuit to measure an output voltage. It can be tuned by the choice of the contact. An ohmic contact offers a high mobility for carriers, leading to a quasi-instantaneous screening of the piezopotential. When both contacts of ZnO NWs are ohmic, no output voltage is measured. This is why a Schottky contact is required as explained for the working principle of the PENG in Figure 1-8d. A stable, reproducible and uniform Schottky contact between metal and ZnO is still an issue. The Schottky barrier is known to depend on the difference of the work function between ZnO and metal but is also significantly impacted by the interface states, the environment, humidity etc. This usually modifies the value of the Schottky barrier. In particular, in the case of mechanical energy harvesters, the cycling deformation of the device induces a modification of the interfaces; this was attributed to the hard contact between the metallic electrode and the NWs [18]. To solve those reliability issues, Hu *et al.* used a blocking contact made of a dielectric polymer, the PMMA [36]. Therefore, the working mechanism of a PENG with ZnO encapsulated in a dielectric material differs from the Schottky contact, as shown in the Figure 1-14d. Under strain, the piezopotential induces aligned electrical dipole moments in the dielectric material. Thus, electrical charges move to the electrodes to screen the built-in electric field (Figure 1-14e). When the stress is released, the induced dipole vanishes in the dielectric material and the external charge flows back, as described in Figure 1-14c. A work from Hinchet *et al.* demonstrated that the use of stiffer dielectric material like Al_2O_3 instead of PMMA seems to increase the output performance of the PENG based on vertical ZnO NWs [60]. A p-n junction was also demonstrated to reduce the external screening by creating a depletion layer at the p-n interface [61], [62].

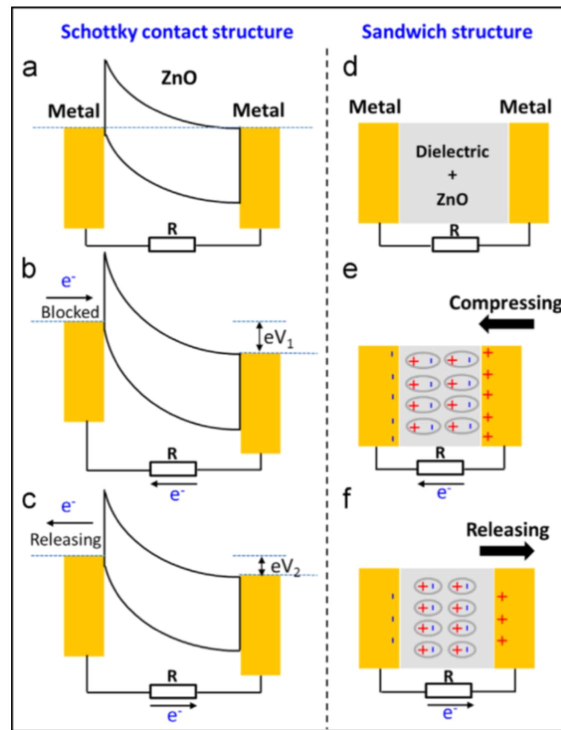

Figure 1-14: Comparison of working principle between PENG based on a Schottky contact (a-c) and a blocking barrier (d-f) from [18]

Beyond the optimization of the device architecture, Briscoe *et al.* questioned the usual characterization of PENGs which usually deals with the measurements of the maximum open circuit voltage (V_{oc}) and the maximum short circuit current (I_{sc}) [63]. Two PENGs with the same ZnO NWs are grown by wet chemistry on ITO electrode for an ohmic contact. On one hand, a blocking contact is fabricated with PMMA for the first device and on the other hand, a p-n junction is fabricated with PEDOT:PSS for the second device. Following the characterization, PENG with a blocking barrier exhibits a higher V_{oc} than the p-n junction. The PENG with the p-n junction shows a higher I_{sc} than the blocking barrier. The comparison of V_{oc} and I_{sc} is therefore inefficient to compare power performances.

Based on this it becomes clear that the comparison of the power performance of different PENG devices requires a particular attention. Many studies consider the maximum output power of their PENG simply as the product of V_{oc} (voltage output at infinite resistive load) and I_{sc} (current output at a null resistive load) [34], [35], [47]–[49], [52], [57], [61], [64]–[66]. Some of these works exhibit surprisingly large output performance but, unfortunately, the calculated performance is unrepresentative for the real power output. Generally speaking, a

power output is function of a resistive load like the voltage output and the current, as represented in Figure 1-15. Therefore, the maximum output power figured out by a PENG is the product of the output voltage and the current at an optimum resistive load. This real power is several times lower than the "apparent" power (V_{oc} x I_{sc}). A work of Stassi *et al.* shows a real power output estimation of 11.25 mW cm^{-3} with an optimum resistive load of 50 kΩ [67]. They also estimate an "apparent" output power more than 500 times larger with a value of 287.5 mW cm^{-3}. This demonstrates the importance to characterize a PENG performance at a specific resistive load. Some studies use this characterization method with a resistive load, showing some realistic output performance [51], [63], [67]–[74].

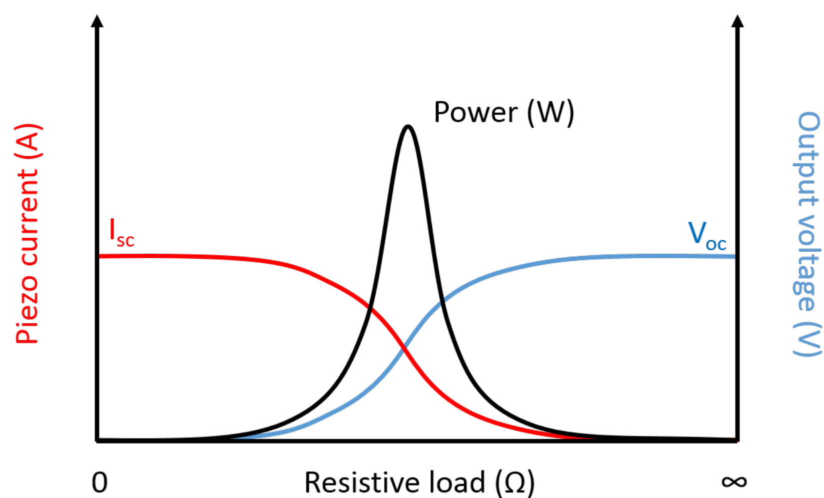

Figure 1-15: Schematic of the real power output of a PENG through a resistive load varying from zero to infinite.

The performance of PENGs can be also significantly increased by optimizing the energy conversion from mechanical to electricity. The transduction from the intermittent source of vibrations to the piezoelectric nanostructures determines two different conversion mechanisms: a *stress-driven* conversion and a *strain-driven* conversion [75]. Different examples of PENGs actuation based on nanowires are illustrated in Figure 1-16. Figure 1-16a shows the displacement of NWs fixed on a vibrating structure. To harvest energy, this system should vibrate at the resonance frequency of the NWs, above the MHz, far above all vibration mechanical system, and can be neglected. Figure 1-16b shows a PENG implanted in a running shoe. The PENG is composed of NWs vertically aligned in a template. Both stress and strain conversion are here possible. If the stiffness of the template is bigger than the stiffness of the NWs, this is a stress-driven conversion. In the contrary, if the stiffness of the NWs is bigger

than the stiffness of the template, this is a strain-driven conversion. In the Figure 1-16c, a stretchable substrate is fixed on an expandable organ. The conversion is strain-driven due to the strain induced in the NWs by the substrate. Figure 1-16d shows a nanowire fixed on an oscillating substrate. This case can be reported as a vibrational piezoelectric energy harvester and is a strain-driven conversion. The Figure 1-16e shows a composite system of NWs embedded in an oscillating cantilever. This system is mimicking a vibrational system but is far from the resonance frequency of the NWs. This PENG is strain-driven, even if a consequent amount of NWs can influence the mechanical properties of the cantilever.

Based on those examples, an energy conversion efficiency, χ, can be defined as the ratio between the electrical work performed by the PENG and the net energy supplied to the PENG [75]. This energy conversion efficiency is different from the electromechanical coupling factor, k^2, defined as the ratio the between the electrical work performed by the PENG and the energy supplied to the PENG, excluding losses. The energy conversion efficiency of both piezoelectric ceramic and polymer has been reported to be in the same order of magnitude. Nevertheless, the energy conversion efficiency normalized by the stress or the strain energy source shows a difference about one order of magnitude between ceramics and polymer. A mechanical stress is ten times better converted by a polymer than a ceramic and a mechanical strain is ten times more converted by a ceramic than a polymer.

This energy conversion analysis highlights the difficulty to quantitatively compare the PENG performance with different design and energy sources.

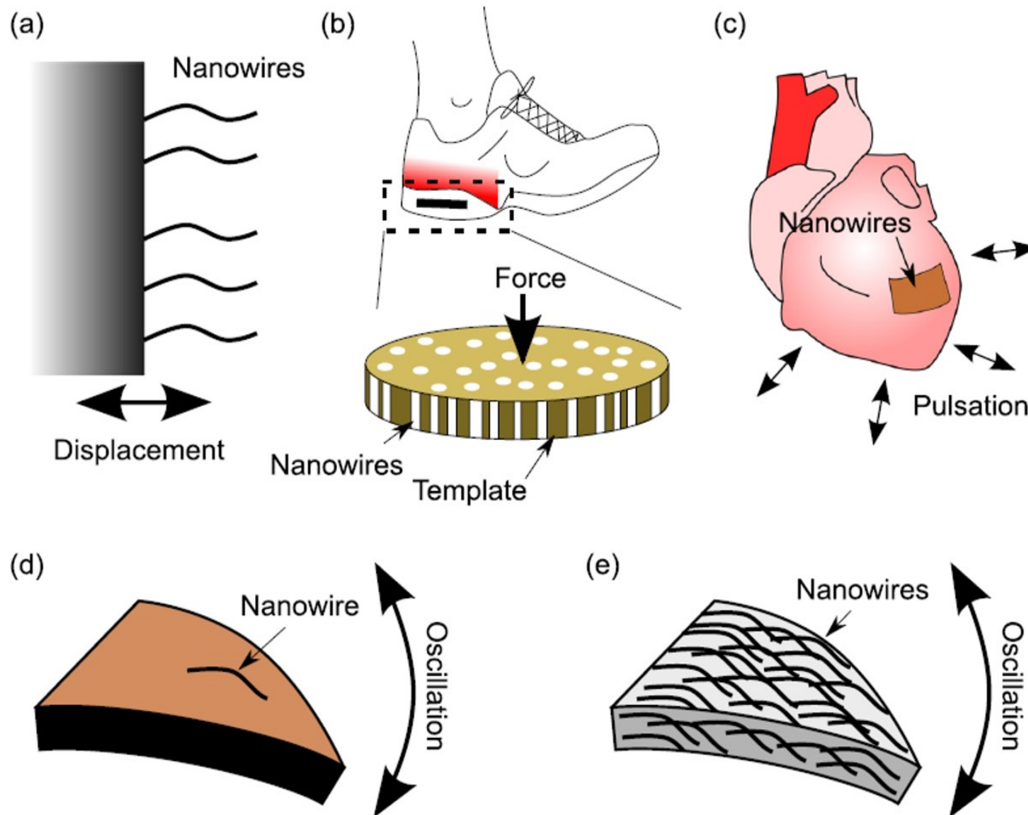

Figure 1-16: Examples of different conversion of kinetic-to-electrical energy based on piezoelectric nanowires from [75].

1.6. Aim and approach of this project

This work stands in the overall context of devices for energy harvesting. Among the different types of energy which can be harvested, mechanical energy is particularly appropriate to power small wearable devices with low energy requirements. Out of various mechanical energy harvesters, those based on piezoelectricity exhibit interesting performances.

Previous literature work has shown that piezoelectric nanogenerators based on ZnO nanowires are a promising technology. Despite their performances, different drawbacks have been identified. First, the bottom-up approach to grow the NWs results in a non-uniformity of height, width and density that can barely be controlled. Secondly, the semiconducting behavior of ZnO requires to decrease the carrier concentration of NWs to avoid a charge redistribution, screening the piezopotential [53].

To the best of our knowledge, the currently used materials and device fabrication process do not allow to control the aspect ratio, the density, and the carrier density of ZnO NWs simultaneously, all of which are needed for the tuning and optimization of performances.

This context and diagnosis is the foundation of the present work.

The aim of our work is to conceptualize by models, to fabricate and to investigate a new kind of piezoelectric nanogenerator based on tailored ZnO nanostructures to rigorously investigate the interplay between tunable piezoelectric materials properties, device architectures and the output power performance. Based on literature, the output power performance requires a specific attention to extrapolate realistic values and compare devices.

To achieve this goal, we have chosen to privilege a top-down process that allows an accurate control of the aspect ratio and density of ZnO nanowires with Nano-Imprint Lithography. Then, using Atomic Layer Deposition as a low-temperature process of ZnO we intend to tune the electronic transport and the local structure of ZnO with nitrogen doping to optimize the piezoelectric properties. We will show that this approach enables an easy scale up for the fabrication of large flexible piezoelectric nanogenerators showing original properties.

2. Experimental Part

This chapter describes the machines and tools used to fabricate and characterize the piezoelectric nanogenerators based on ZnO, by providing representative examples and characteristics of the used techniques. Substrates, precursors and materials used for the fabrication/characterization are also presented.

2.1. Experimental process

The fabrication of the investigated piezoelectric nanogenerator for large scale production requires rather few steps and machines. The flowchart for the spin-coating, the NIL and the ALD is described in Figure 2-1. The process is realized in a cleanroom environment ISO 5, and ISO 4 for the deposition area.

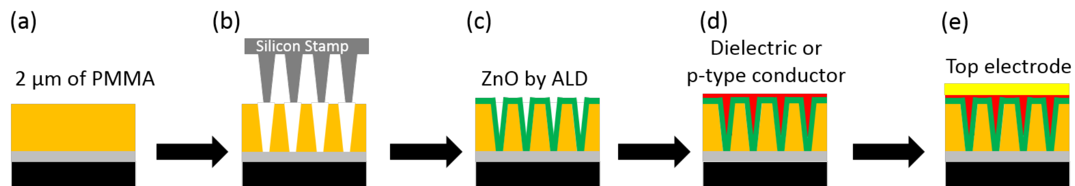

Figure 2-1: Flowchart of the piezoelectric nanogenerator process. a) Spin coating process of PMMA polymer on substrate with or without a bottom electrode. b) Nano-imprint lithography. c) Atomic Layer Deposition of ZnO. d) Deposition of dielectric or p-type conductor. e) Deposition of the top electrode.

2.1.1. Spin coating

Spin coating is a technique used to deposit a uniform thin film of a material dissolved in a solvent. In this work, we aim at a uniform layer of polymethyl methacrylate (PMMA) of 2 µm (custom solution of “mr-I PMMA 35K 2µm” from Microresist Technology for nanoimprint application). Due to the high viscosity of the solution and to avoid any residual defect, a 2-step spin coating is performed. First, a small amount of the viscous solution is applied on the center of the substrate and is spread at low speed spinning. Then, the substrate is spun at higher speed (around 2000 – 3000 rpm min^{-1} for 60 s) to reach the desired thickness of 2 µm, spreading outside the exceeding material due to the angular moment of the spinning. The solvent of the solution is usually volatile and evaporates during the spinning but a post bake at 120°C during 3 min is required to fully degas the solvent kept inside the film. Another material spun is the PEDOT:PSS (Poly(3,4-ethylenedioxythiophene)-Polystyrene sulfonate

1.3 wt % dispersion in H_2O, conductive from Sigma Aldrich). This polymer with a conductivity of 1 S cm^{-1} is spin-coated on ZnO thin film.

The size and the nature of substrates (i.e. flexible or rigid) are easily adjustable for this technique. Potential drawbacks of this technique are the lack of adhesion, the delamination or the incomplete filling of holes for highly rough substrate: this is specifically true for the PEDOT:PSS spin coated on ZnO nanowires (obtained after the ALD process).

2.1.2. Nano-imprint Lithography (NIL)

The NIL is a technique designed for patterning at the nanometer scale. It is a simple nanolithography process with a higher resolution and a lower cost than the classical UV lithography process. The working principle of the NIL process is based on a stamp embossing a resist. There are two kinds of NIL processes regarding the resist used: the thermal NIL or the UV photo NIL. In our work, NIL processes were performed on an Eitre® 6 from Obducat (Figure 2-2). The substrate size can vary from 10 mm to 152 mm (6 inch) diameter. A UV module allows combining both UV and thermal imprint in the same platform. The maximum imprint pressure and temperature are limited to 80 bar and 200°C.

Figure 2-2: Picture of the Eitre® 6

The design of the stamp is critical to achieve a high quality of NIL. The stamp can be made of a hard material (e.g. silicon, nickel, …) or a soft material (e.g PDMS). Usually the stamp is covered with an anti-sticking layer to easily demold the stamp after imprint without damaging it.

In this work, all master stamps used are made of silicon and ordered from *Eulitha*. The Figure 2-3 shows optical SEM pictures of the used stamps. The dimensions of these stamps will be discussed in the last chapter and are based on an electromechanical optimization. The stamp in Figure 2-3a & c has a length of 2 µm and an average diameter of 200 nm (small and large diameter of 120 nm and 400 respectively), leading to an aspect ratio of 10. The anti-sticking layer used is a silane, the F17-DTCS, (heptadecafluoro-1,1,2,2-tetrahydrodecyl)trichlorosilane (from Gelest). The deposition of the silane occurs in a closed desiccator at 1-2 mbar by vapor phase during 4 hours due to its high reactivity with water and slower reactivity with hydroxyl group of the native silicon oxide.

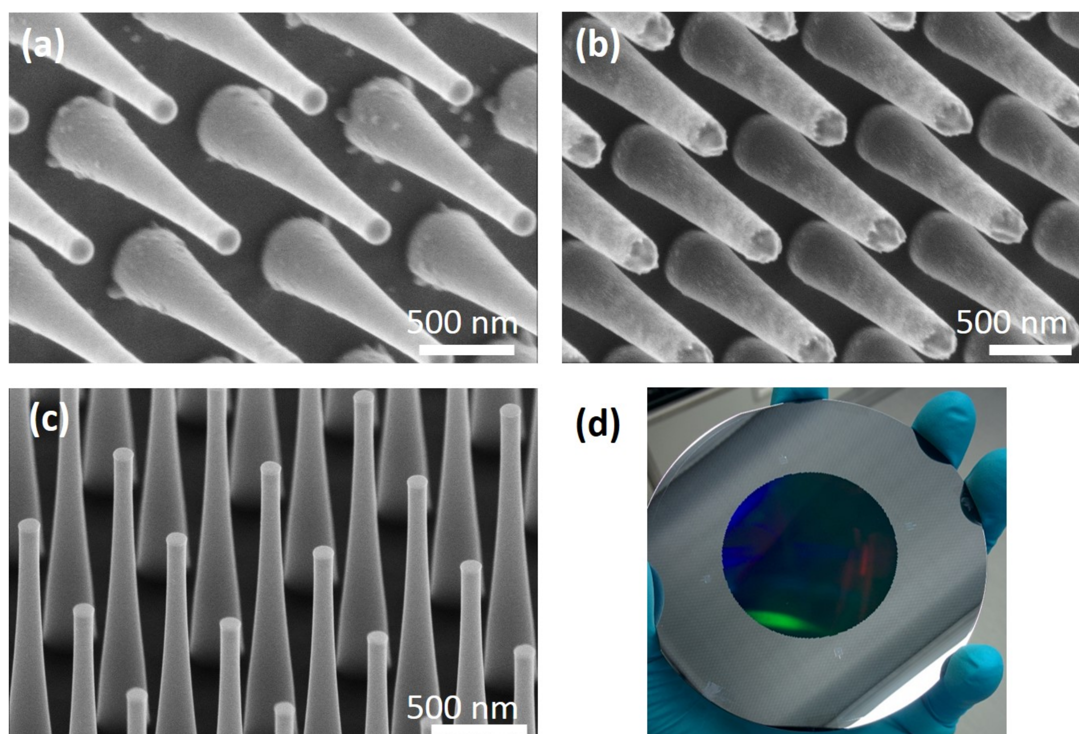

Figure 2-3: SEM and optical picture of the used stamps in this work. All nanostructures are 2 um height. a) Area of 5x5 mm² with a pitch of 840 nm. Average diameter of 200 nm with a small and large diameter of 120 and 400 nm, respectively. b) Area of 7.5 x 7.5 mm² with a pitch of 800 nm. Average diameter of 250 nm with a small and large diameter of 200 and 400 nm, respectively. c) Area of 5 cm diameter with a pitch of 780 nm. Average diameter of 200 nm with a small and large diameter of 120 and 400 nm, respectively. d) Optical picture of the 4-inch silicon stamp of c) covering an area of 5 cm of diameter.

Thermal NIL

All devices presented in this work are made with the thermal NIL process. The PMMA used for NIL is a thermoplastic polymer and has a glass-transition temperature (T_g) of 105°C. The T_g is defined as the transition temperature where, below the amorphous (or semi-crystalline) material is hard and relatively brittle (i.e. like a glass), and above, the material becomes a

viscous liquid (or acts like a rubber). Usually, the working temperature of the NIL process is set 50°C above the T_g, 155°C in our case. When the temperature is reached, a pressure of 40 bar is applied during 120 s for the hot embossing of the stamp on the substrate (Figure 2-4). Then, the system is cooled down below the T_g at 70°C and the pressure is released. The Table 2.1 summarizes the steps of temperature, pressure and time. Usually, a residual thin film of resist of 10 to 20 nm remains after NIL, requiring an additional etching-step to remove it. In our case, the pattern of the stamp enables an imprint without any residual layer because of the high aspect ratio combined to the conical shape. The development of the residual-free layer process in this work lead to a filed patent ("*Mould for nanoimprint lithography - LU100433*"). The Figure 2-5a-c shows SEM pictures of the imprinted PMMA.

Table 2.1: Steps of the thermal NIL process with PMMA

Step	**T(°C)**	**P(bar)**	**t(s)**
1	155	7	60
2	155	40	120
3	70	40	10

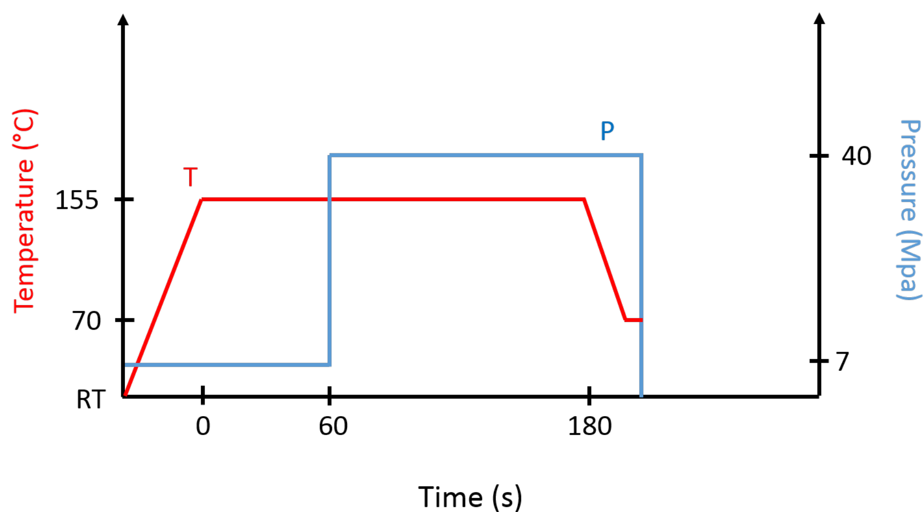

Figure 2-4: Schematic of the pressure and temperature time variation during the thermal NIL process.

UV NIL

The UV NIL requires a UV transparent stamp due to the position of the UV lamp on the top during the NIL. For this, the stamp is replicated with the IPS® technology (Intermediate Polymer Stamp, Obducat) by thermal NIL. The IPS® is a thermoplastic polymer UV transparent containing anti-sticking element. The UV NIL does not require a high pressure and temperature as the thermal NIL. The IPS replication stamp embosses at low pressure (7 bar, the lowest pressure applied) on a UV sensitive resist. Then the UV lamp activates the polymerization. This technique allows to perform several imprints on the same substrate to obtain a multi-stack, compared to the thermal NIL. In our case, the IPS replication is a negative pattern of the stamp that needs to be replicated again. For this, we use the Ormostamp®, a specific UV sensitive resist designed for UV NIL and replication. The Figure 2-5d shows the Ormostamp® imprinted from IPS and compared to the original stamp, the pattern is not perfectly replicated because of the high aspect ratio.

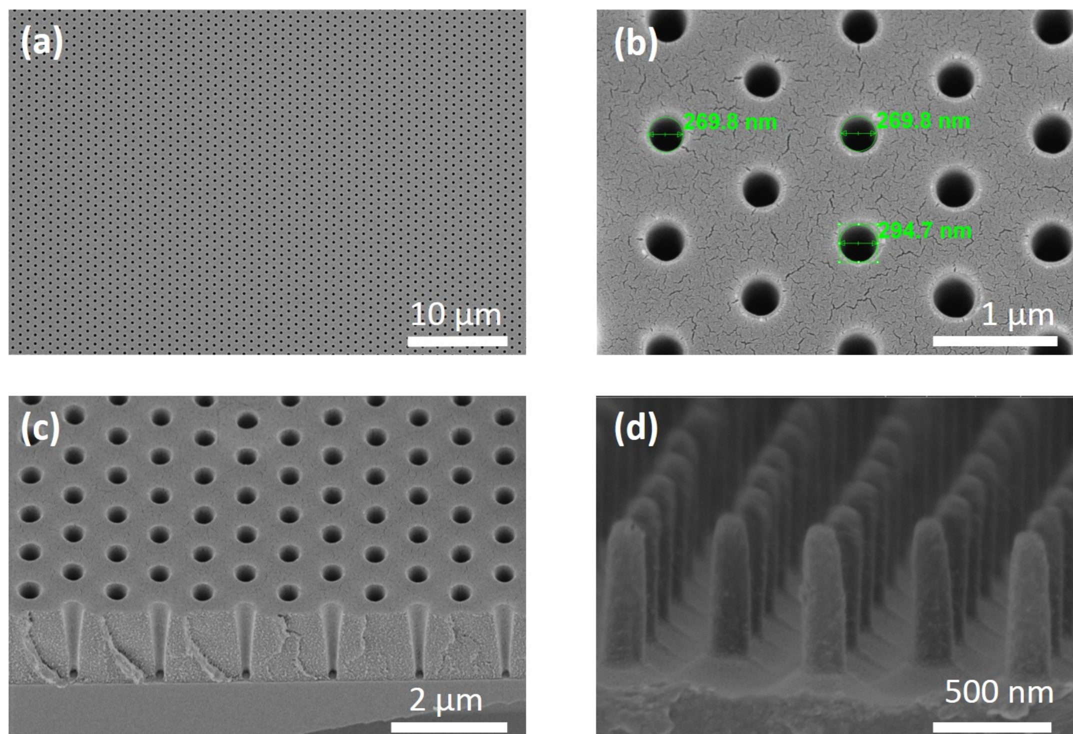

Figure 2-5: a-b) SEM top view of imprinted PMMA metallized a few nanometers top view at different magnification. c) Tilted SEM view of metallized imprinted PMMA. d) Replication of the stamp in Ormostamp®.

2.1.3. Reactive Ion etching (RIE)

The reactive ion etching (RIE) is a very common tool used in micro and nano-fabrication. This dry plasma etching ensures an isotropic or an anisotropic clean etching because of the gaseous products from the plasma reaction with the surface. The RIE reaction depends on the nature of the plasma (i.e. the reactive gas) and its interaction with the substrate. Inert gas (Ar, N_2) are usually used for sputtering. Halides (Cl_2, Br_2), fluorine-based (CF_4, SF_6, CHF_3, …) and oxygen-based gas react chemically with the substrate through a plasma generated by a RF system at low pressure.

The Plasma-Therm 790 RIE is used to remove the residual layer of PMMA after NIL. The reactive chamber is sized for a 8 inch (200 mm) diameter substrate. Four gases are available: oxygen, nitrogen, argon and CF_4. A plasma, based on oxygen, easily etches organic compounds such as PMMA. If needed, the etching conditions to remove the residual layer of PMMA are the following: a O_2 gas at a pressure of 60 mTorr with a power of 50 W give an etching rate of 100 nm/min. Nevertheless, the whole PMMA template is etched and affected by the RIE. Some side effects as an increase of the roughness, or the chemical modification of the surface of the PMMA or the bottom electrode can strongly affect the properties of the final device. Indeed, the oxygen-plasma can oxidize the bottom electrode and modify its electronic properties at the interface with the ZnO processed by ALD. This RIE step is facultative and can be skipped with the NIL without residual layer.

2.1.4. Atomic Layer Deposition (ALD)

The advantage of the ALD technique is a highly conformal thin film growth on flat, porous, complex 3D substrates or even on powders. The working principle is based on the self-limiting reaction on the surface of injected precursors. Those precursors chemisorb on the surface and are carried and purged with a nitrogen flow. The ALD process is performed in a commercial reactor TFS200 from Beneq (Figure 2-6 [76]). The reaction chamber is adaptable regarding the geometry of the substrate. Four configurations are possible:

- **Thermal planar configuration**: the diameter matches for 200 mm silicon wafer (8 inch). Only substrates with a thickness below 2 mm can fit-in because of a chamber height of 3 mm. This small volume for the reaction chamber enables a quick saturation of the precursors, even for a low exposition time, and a fast rate of deposition, compared to larger volume of the reaction chamber. Possible temperatures of

deposition start from room temperature up to 400°C. A heating element surrounds the reaction chamber for a homogeneous temperature distribution.

- **Plasma planar configuration**: a RF plasma is generated in order to initiate the reaction between the precursor and the surface of the substrate instead of using a thermal activation.
- **Internal fluidized-bed configuration**: a fluidized-bed suspends the powder with an inert gas (usually nitrogen) for a conformal deposition.
- **External fluidized-bed configuration**: same working principle than then the internal configuration, but enabling the reach of higher temperature up to 1000°C if a higher thermal activation is required.

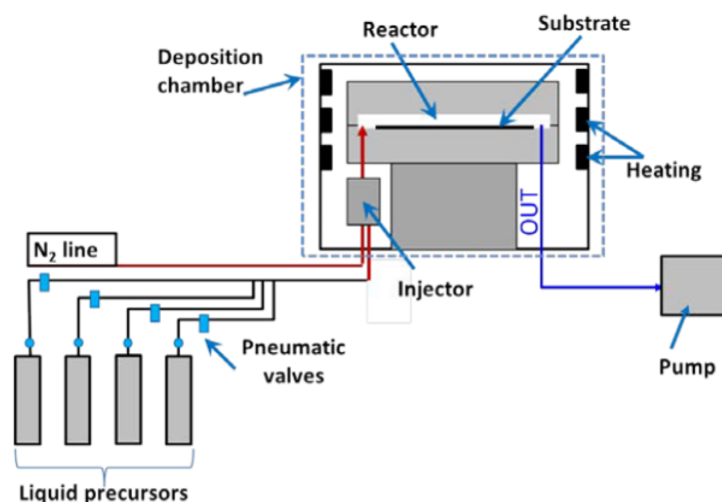

Figure 2-6: Graphical representation of the ALD from [76]

ALD is generally a vacuum-based process with a typical pressure around 1-5 mBar in the reaction chamber maintained with the carrying/purging gas. Precursors used can be solid or liquid and are stocked at room temperature. If they are volatile, they form a vapor phase that is injected in the reactor with a carrying gas (usually nitrogen). Some liquid precursors with a low pressure vapor phase can be heated with a hot source up to 250-300°C and up to 500°C for solid precursors. The quantity of the vaporized precursors is controlled accurately by pneumatic valves. The shortest time of pulse is 50 ms and can be longer than several seconds to completely react and saturate the surface of the substrate. The time of purge is the required time to totally remove exceeding precursor and products of the reaction before the next pulse of the precursor in order to avoid a chemical vapor reaction deposition in the chamber (Figure 2-6). The ALD temperature-window is defined as the range of temperatures

where the rate of deposition is constant. Above this temperature-window, some desorption or pyrolysis can occur. Below, some condensation or an incomplete reaction may be present because of an insufficient reactivity.

In our case of study, the highly conformal deposition easily fills the high aspect ratio (10) of the polymer template. The planar thermal configuration is used and a low temperature is mandatory to avoid the melting of the polymer (below 120°C). Precursors used are the diethylzinc (DEZ) (Sigma Aldrich) and deionized water as zinc and oxidant source, respectively. A previous thesis by Vincent Rogé already investigated the ZnO ALD in this reactor with such precursors, determining the ALD window and the minimum time of pulse and purge [77]. For all the experiments, the time of pulse for the DEZ and water are fixed at 250 and 200 ms, respectively (Figure 2-7). The minimum time of pulse saturating the surface reaction of substrates for a homogeneous thin film starts at 5 ms. The process remains in the standard ALD regime, without any CVD process, for purging time above 500 ms. The time of purge is investigated in this work, between 1 to 60 seconds. The number of cycles determines accurately the thickness of ZnO thin films with a mean growth rate of 0.2-0.3 nm per cycle. A calibration of the rate of deposition is required for each temperature because of the unconventional work below the temperature window.

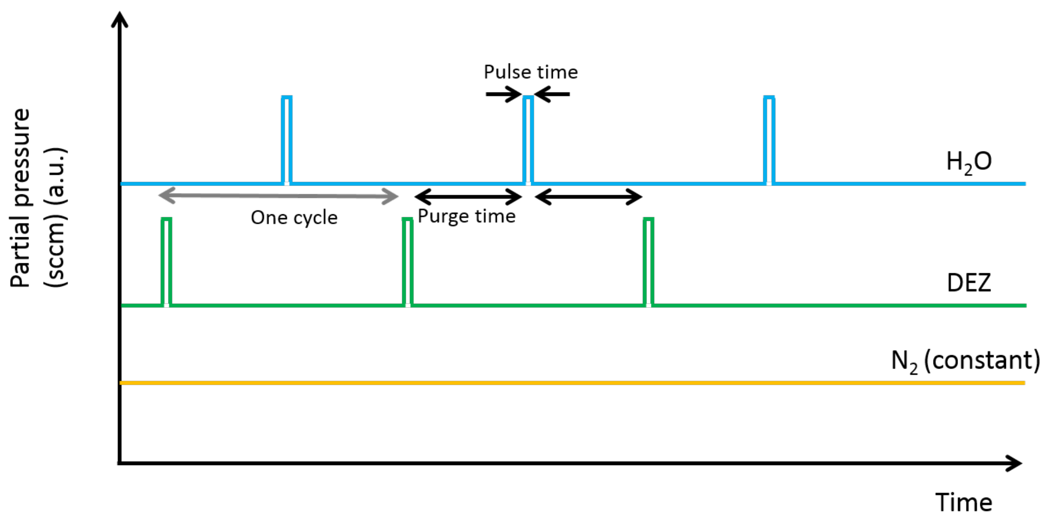

Figure 2-7: Schematic of the ALD process for the different partial pressure of precursors and gas carrier.

Another common liquid precursor, the trimethylaluminum (TMA) is reacting with water to deposit a passivation layer of Al_2O_3. The usual temperature of this process is 200°C but the sensitive temperature substrate forces to deposit below the temperature window, at 80°C,

requiring an experimental thickness calibration due to the lower thermal activation of the TMA precursor.

2.1.5. Metal Evaporator/Sputtering

An e-gun metallization is possible for samples smaller than 4x4 cm². Different metals (Au, Ti, Cr, Pt) can be evaporated in a e-gun evaporator from Meca 2000. An ultra-high vacuum around 5×10^{-9} bar is required for a high quality metallization. The top-electrode in this work is composed of Ti and Au with a thickness of 5 and 50 nm, respectively. The thin layer of Ti promotes a good adhesion and prevents the delamination between Au and the substrate. The sample is selectively metallized with some Kapton tape covering the unwanted metallized area.

Larger samples than 4x4 cm² up to 10 cm diameter can be metallized by sputtering. Pt or Au are sputtered on the substrate without adhesive layer compared to the evaporator. An Argon plasma is generated at 5 mbar. This plasma erodes the metallic target and the metallic particles are deposited on the substrate. An average thickness around 80 nm is deposited on the substrate.

2.1.6. Plasma Radical Assisted Polymerization Chemical Vapor Deposition (PRAP-CVD)

The working principle of the PRAP-CVD is based on the simultaneous reaction between an oxidative radical initiator (Br_2) and a vaporized monomer (EDOT) to deposit a conductive thin film of PEDOT, as shown in the Figure 2-8. A plasma with the radical initiator is generated before the mixing with the monomer, avoiding any surface modification of the substrate by the plasma [78]. Another advantage is the low temperature of the process at 80°C, compatible with the temperature sensitive resist of PMMA. The 100 nm thin film of PEDOT deposited is highly conformal [79], providing a good contact interface with the substrate. The maximum size of the substrate is 200 mm diameter. The PEDOT is known as a p-type conductor and its conductivity is in the range of a few $S.cm^{-1}$.

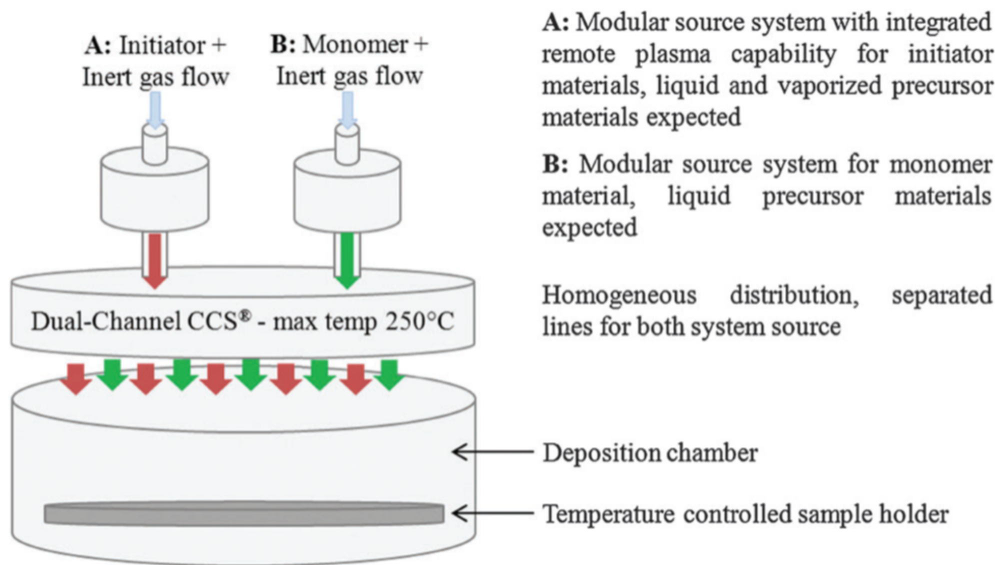

Figure 2-8: Schematic representation and working principle of the PRAP-CVD from [78]

2.1.7. Wet etching

Different wet etching are used to access to the bottom electrode. Diluted hydrochloric acid in deionized water (1:60) etches ZnO and Al_2O_3 with a rate around 2 µm min^{-1}. An organic solvent, dichloromethane (CH_2Cl_2) etches the PMMA at a rate faster than 10 µm min^{-1}.

2.2. Techniques for material characterization

Each step of the fabrication requires appropriate characterization techniques to fully understand, control and optimized the properties of materials used for the piezoelectric nanogenerator.

2.2.1. Ellipsometry

Thicknesses of the PMMA or ZnO are measured by ellipsometry. This characterization tool is based on the change of polarization and reflection of an incident light beam reflected on a material structure. This measurement gives information about the thickness, the roughness and the refractive index *n* of the material. The ellipsometer used is a M2000 from the J.A. Woollam Co. The thickness measurement of the PMMA and ZnO are calculated from an optical Cauchy model. For such measurements, the materials were deposited on reflective substrates such as silicon or platinum.

2.2.2. Scanning Electron Microscopy and Focus Ion Beam (FIB-SEM)

Scanning Electron Microscopy (SEM) is a high-resolution imaging technique with a lateral resolution close to 10 nm. The working principle is based on the electron-matter interaction. SEM is composed of an electron beam focused on the sample surface by electromagnetic lenses. This electron beam interacts elastically and inelastically with the sample leading to different emitted signals. The most common SEM mode is based on the detection of the secondary electrons from the sample surface. Multiples information about the topography, morphology and chemical composition can be extracted. This technique can affect and modify the surface depending on the nature of the sample and the electron beam energy. Conductive and semi-conductive samples are not electronically charging instead of insulated substrates such as polymers. A low energy of the electron beam combined with a thin metal coating (2-5 nm) are required to image easily insulating layers and materials. An example of melted polymer without metallic coating by the electron beam with ZnO nanostructures is shown in Figure 2-9. Most of the SEM pictures are performed with a voltage and a current of 2 kV and 25 pA, respectively. In this work, the SEM equipment is a dual beam Helios NanolabTM 650 from FEI. The SEM is also equipped with an OmniProbe micromanipulator enabling the sample transfer on lamella for TEM analysis. A Focused Ion Beam (FIB) unit is combined to the SEM for the deposition and ablation of materials. High energetic gallium ions are used to etch the sample to perform a thin nanometric slice for TEM. To protect the surface of the sample from Ga^+ etching, a cap of platinum is deposited from an organic vapor precursor, ($CH_3PtC_p(CH_3)_3$). The first 50 nm of Pt are deposited by electron beam assisted chemical vapor deposition (EBA-CVD) and then 300 nm are deposited by ion beam assisted chemical vapor deposition (IBA-CVD), as shown in Figure 2-10 in red. An example of a complex sample of ZnO in a PMMA matrix processed by FIB-SEM is shown in the Figure 2-10. The grey area shows the etched surface from the FIB characterization.

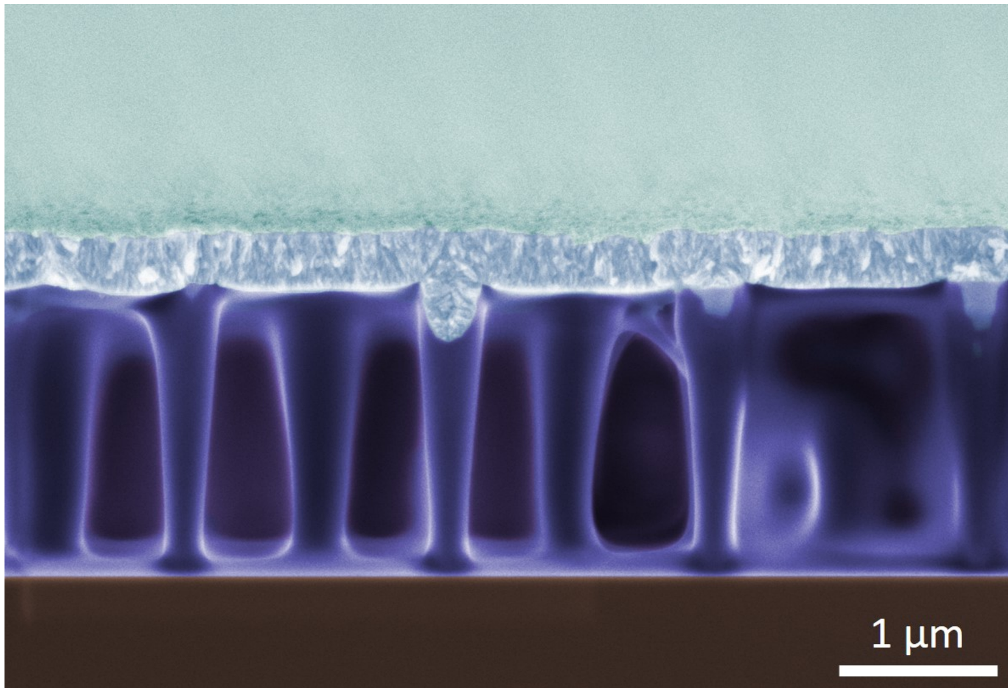

Figure 2-9: SEM cross section of ZnO NWs network (in light blue) with melted polymer (in purple). The melting polymer brings out the second line of the NWs array.

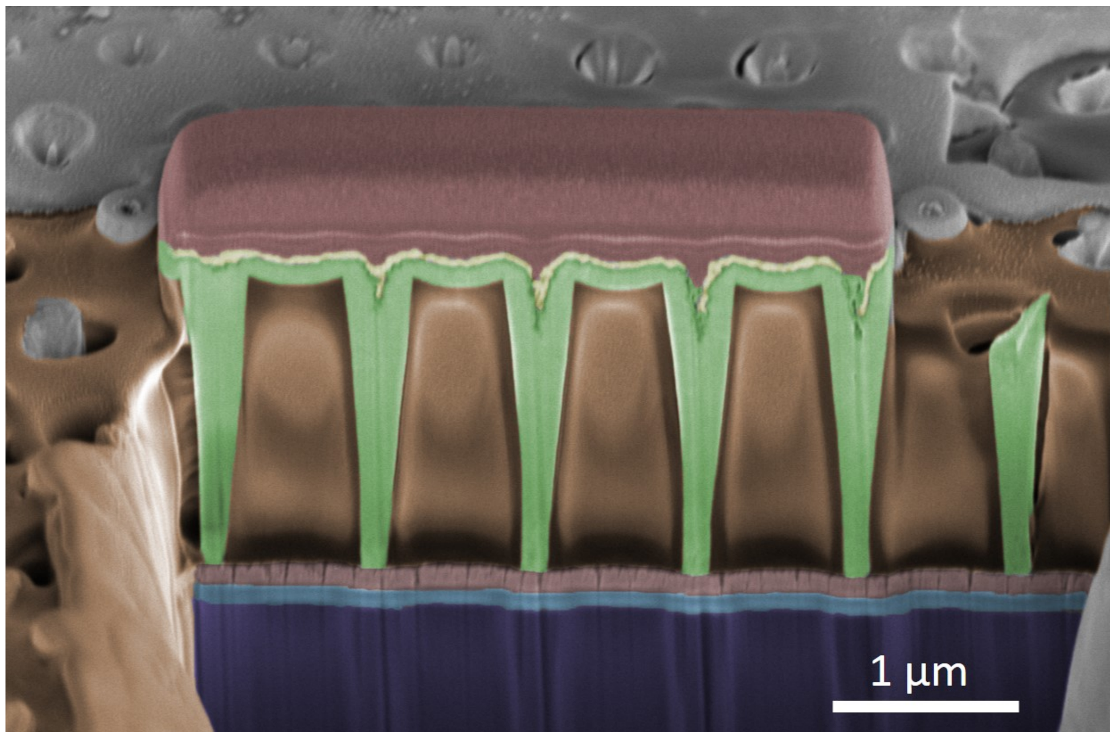

Figure 2-10: FIB-SEM cross section of ZnO NWs in a patterned polymer (in false color). From down to up: silicon substrate (purple), dielectric layer of Al_2O_3 (light blue), sputtered Pt (red), patterned PMMA (orange), ZnO (green), evaporated Au (yellow) and EVA/IBA-CVD Pt (red).

2.2.3. Transmission Electron Microscopy (TEM)

Transmission Electron Microscopy (TEM) is based on a beam of electrons transmitted through the sample, with an imaging resolution down to 0.1 nm. The ultrathin sample has usually a thickness lower than 100 nm. In this work, the TEM used is a Titan G3 from FEI to characterize the ZnO nanowires. The analysis is performed on a lamella prepared by FIB-SEM (Figure 2-10). Different modes of imaging are possible. First, the bright field TEM visualizes the sample by a direct transmission of the electron beam. Then, the high resolution TEM (HRTEM) allows to observe the interaction of the electron beam with the lattice of the material. Unfortunately, our lamella is too thick to determine any relevant information from HRTEM. Another mode is the dark field, visualizing the diffracted beam. Materials diffracting the beam appears brighter when selecting a specific orientation. In the case of ZnO, it allows to determine the grain-orientation. The last mode used in this work is the high-angle annular dark-field (HAADF), visualizing in grey scale the atomic composition. As an example, this mode displays a perfect continuity between the bottom of the ZnO nanowire and the bottom electrode, demonstrating the free-residual layer processed by NIL (Figure 2-11).

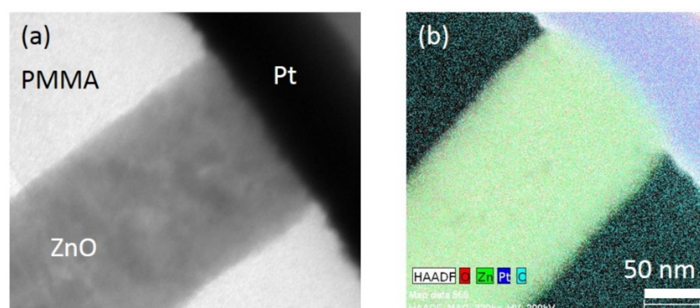

Figure 2-11: TEM of a lamella of ZnO nanowire in PMMA. a) Bright field TEM interface between ZnO and Pt. b) HAADF interface between ZnO and Pt.

2.2.4. X-Ray Diffraction (XRD)

X-ray diffraction (XRD) is a common method providing information about the crystal structure. The extracted information are the crystalline phase, the lattice parameters, the crystallite size and the texture regarding a preferential growth orientation. These information come from the diffraction of X-rays following Bragg's law: the incident X-ray with a specific wavelength is refracted by lattice planes, spaced with a specific distance, with a determined angle. The crystallite size can be determined with the Scherrer equation. In this work, a diffractometer

D8 discover from Bruker characterizes ZnO thin films. It uses a copper X-ray source with a wavelength K_α of 0.1542 nm. Diffractograms are characterized following a θ-2θ mode from 20° to 70° with a step resolution of 0.02°. The lattice parameters of wurtzite structure of ZnO, *a* and *c*, are determined using the interplanar spacing *d* with the Miller indices *h,k,l*, according to the equation:

$$d_{hkl} = \frac{1}{\sqrt{\frac{4}{3a^2(h^2+k^2+hk)+\frac{l^2}{c^2}}}}$$

2.2.5. X-Ray Photoelectron Spectroscopy (XPS)

The X-ray photoelectron spectroscopy is a surface characterization technique providing a qualitative and quantitative information about the chemical composition, bonds and the stoichiometry of the material. The typical depth analysis is a few nanometers (<15 nm). The working principle is based on the interaction between X-ray photons and electrons of the valence band of the material. Then, numerous photoelectrons are emitted with a specific energy, ratio, regarding the atomic composition of the material. The count and the specific kinetic energy detected provides information of the concentration and the chemical state of the atoms in the material.

In this work, ZnO thin films are characterized with an AXIS Ultra from Kratos using a hemispherical energy analyzer. The working energy of the monochromatic X-ray beam source (Al Kα, E = 1486.6 eV) is 150 W and the spot size analysis can be of 110 µm diameter or 300 x 700 μm^2. An argon sputtering of the material surface is possible to etch a few nanometers, removing the surface contamination as carbon based compounds. The depth analysis for the ZnO is 6 nm [80]. The samples are characterized under an ultra-high vacuum of 10^{-9} bar.

Nevertheless some water molecules may contaminate the etched surface of ZnO, leading to a monoatomic hydrogen contamination of the surface. The Figure 2-12 shows a kinetic analysis of the peak O1s (O-Zn binding energy) at 530.5 eV of an etched ZnO thin film. A shoulder appears around 532.5 eV that is the O1s of the O-H binding energy. One hour after the Ar sputtering, the atomic concentration of H reaches 7 % at. in the ZnO thin film. In reality, the OH monolayer covering the ZnO represents 1 over the 12 analyzed atomic layers showing a biased characterization (lattice parameter c = 0.52 nm). Indeed, 60 s after the etching, no shouldering is observed leading to an atomic concentration of H lower than 1 % at. that is the

atomic resolution of this XPS. This kinetic study shows how carefully the hydroxylated surfaces of metal oxides have to be analyzed.

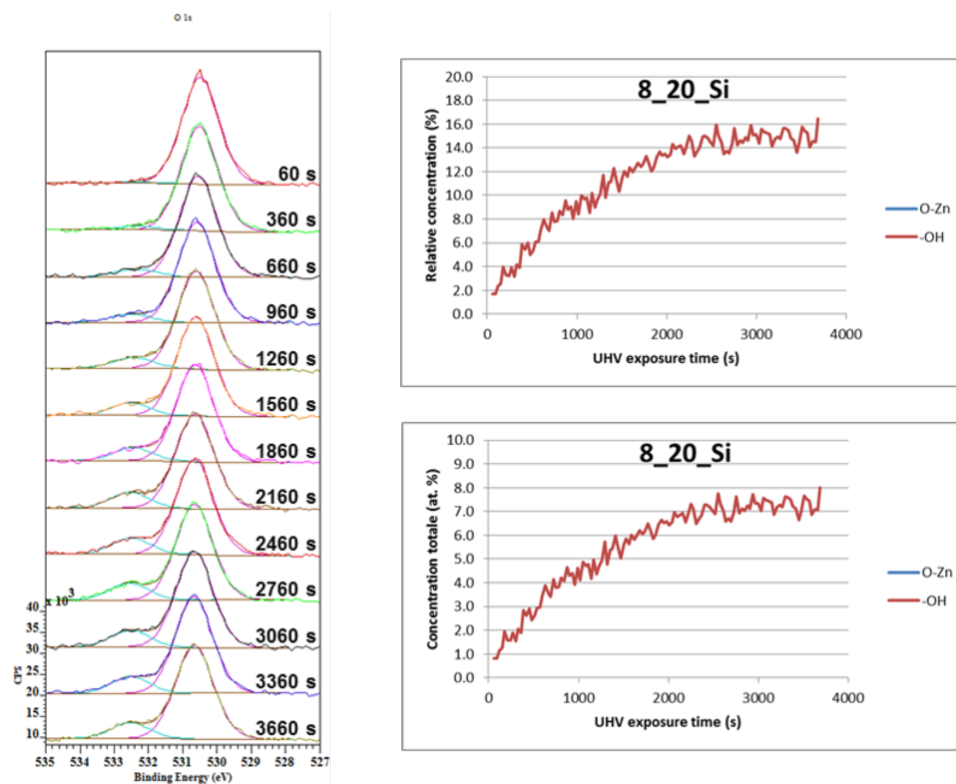

Figure 2-12: XPS dynamic analysis determining the hydroxylation of the ZnO surface after sputtering.

2.2.6. Secondary Ion Mass Spectroscopy (SIMS)

SIMS is a surface analysis technique that sputters a primary ion beam and analyzed the secondary ions emitted from the material. A mass spectrometer analyses those secondary ions according to their ratio mass/charge. A CAMECA SC-Ultra instrument is used for the surface and depth analysis of ZnO thin films. The different elements of interest are analyzed as MCs_x^+ clusters (M = H, C, N, O, F, Cl, Zn with x = 1 or 2) to avoid any matrix effect. Complementary analysis of negative ions M^- increases the sensitivity and the detection limit. In this work, all the compounds of ZnO films are normalized to Zn^{2+} signals for a comparative analysis.

2.2.7. Raman Spectroscopy & Photoluminescence

Raman spectroscopy is based on an inelastic scattering of light by a material. One of the main interest is the information relative to structural properties of the material. These structural properties are investigated by the vibrational (phonon) interaction of the material and light. This interaction changes the frequency of the scattered Raman light due to a modification of the electronic polarisability in the material. In this work, Raman spectra are recorded by a Renishaw inVia confocal Raman microscope. Laser beams with different wavelength can be used. A laser beam with a 532 nm incident wavelength is used to characterize ZnO.

Photoluminescence is the light emission of a material after absorption of photons. In the case of a semiconductor material like ZnO, the absorption of photons with energy higher than the bandgap leads to generate electrons-holes pairs at the conduction and valence band, respectively. The light emission from the material has a wavelength equivalent to the energy of the bandgap. If intermediate states between the conduction and valence bands are present, they may also emit light, with a lower energy. Photoluminescence spectra are also recorded with the Renishaw inVia confocal Raman microscope. A UV laser beam with a 325 nm wavelength is used. Experiments are performed at room temperature.

2.2.8. Scanning Probe Microscopy

Scanning probe microscopy (SPM) is based on the interface interaction between a sharp tip and the sample surface. In this work, three modes are used to investigate ZnO and device properties: tapping atomic force microscopy (AFM), piezoresponse force microscopy (PFM) and conductive atomic force microscopy (c-AFM) as *Resiscope*. We use a commercial AFM Innova from Bruker for the AFM and PFM characterization.

AFM

Atomic force microscopy is one of the most used mode in SPM. It determines the surface topography of the sample with a very high resolution, lower than 1 nm in depth. The lateral resolution is determined by the tip radius (around a few nanometers) and the scan method. In tapping mode, the cantilever of the tip oscillates at a frequency close to its resonance. The amplitude of the oscillating cantilever is changing with the distance tip-surface. The reflection of a laser on the cantilever to a photodetector controls a feedback loop. This variation of amplitude determines the topography of the sample when the tip is scanning the surface of the sample.

PFM

Piezoresponse force microscopy is based on the contact mode AFM. A constant force is applied on the tip to maintain the contact. An alternative current (AC) bias is applied on a conductive Pt/Ir tip or on the piezoelectric material. This AC current induces a deformation of the sample through the converse piezoelectric effect. This deformation modifies the cantilever deflection, detected by the laser reflection on the photodetector. The amplitude of deformation increases linearly with the amplitude of the AC current applied. The linear increase of deformation is directly linked to the piezoelectric coefficient of the material. This technique is often used to determine inverse piezoelectric coefficient. This technique determines also the orientation of polarization of piezoelectric materials with the phase of the AC current. If there is no phase difference between of the AC signal and the deformation, the polarization of the piezoelectric material has the same orientation than the generated electric field by the tip. In contrary, if there is a phase difference of 180°, the polarization orientation is inverted compared to the electric field.

Resiscope (c-AFM)

The *Resiscope* is a conductive atomic force microscopy technique characterizing the local resistivity (or conductivity) of a sample. This characterization is based on contact mode AFM. A stiff conductive tip is required to ensure a good electrical contact and avoid any artefact measurement due to the surface contamination of the sample during the scan. For this, a conductive diamond tip *DDESP* is slightly scratching while scanning to maintain a good contact. A bias voltage is applied and the measured current determines the resistivity following the Ohm's law. The *Resiscope* is a home-made technique developed by the *Unité Mixte de Physique CNRS-Thales* in Paris and these measurements were performed by S. Fusil.

2.2.9. Four Point Probe Resistivity Measurement

The four point probe setup measures the resistivity of a sample. It is composed of four metal tips with a finite radius, aligned and spaced equally. A high impedance current is applied between the two external tips meanwhile a voltmeter is used on the two inner tips to measure the voltage. This voltage measurement determines the resistivity of the sample, following the Ohm's law and the geometry. In this work, the equipment used is a Jandel four point probes. The current source and voltmeter used is a Keithley 2614B.

2.3. Techniques for device characterization

2.3.1. Impedance meter

A LCR meter and impedance analyzer is an electronic instrument used to measure the electrical impedance of an electronic component or a device. It determines the inductance, capacitance and resistance. An impedance analyzer, IM3570 from Hioki, measures these values between 4 Hz to 5 MHz with an impedance accuracy of ± 0.08 %. It measures many different parameters as for example Z (impedance in Ω), θ (phase angle), R_s (series-equivalent resistance in Ω), R_p (parallel-equivalent resistance in Ω), C_s (series-equivalent static capacitance in F), C_p (parallel-equivalent static capacitance in F), D (Loss coefficient = tan δ (delta)).

2.3.2. Small device setup

A home-made setup is built to characterize small devices with a substrate size of 1 to 4 cm². The setup is composed of two plates screwed together and tightening the anchor of the device as described in Figure 2-13a. The contact for the bottom electrode of the device is ensured by the clamped anchor between the two plates. The bottom electrode is the ground of the BNC connector. A gold wire of 0.05 mm diameter (99.99 % purity from GoodFellow) bonds the top electrode with silver paste to a copper wire, connected to the BNC connector. The device is characterized by bending the end of the cantilever. The output voltage characterizing the piezoelectric device is observed with an oscilloscope Tektronix TDS 2004C through a 1MΩ impedance, as shown in Figure 2-13b.

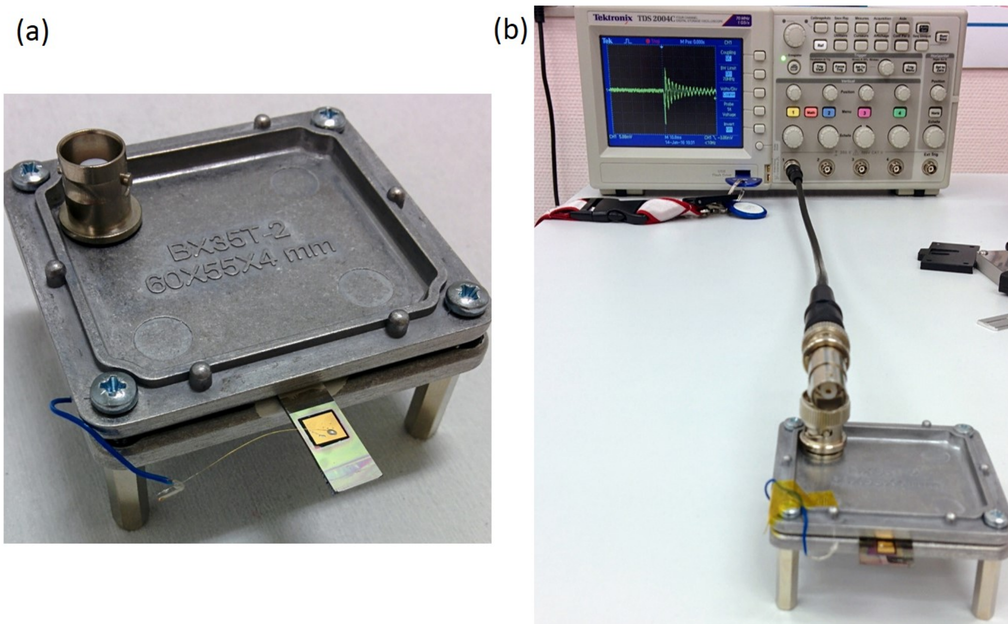

Figure 2-13: a) setup for small devices characterization with top and bottom electrodes connected to a BNC connector. b) Piezoelectric characterization performed with an oscilloscope with a 1MΩ impedance.

2.3.3. Setup for large membrane device

Large scale PENGs with a 5 cm diameter imprinted area require a large setup for an accurate characterization. For this, a substrate holder is designed in a stiff polymer, PEEK (polyether ether ketone). The two PEEK plates clamp the PENG membrane with an annular rubber seal of 78 mm diameter. A semi-transparent cross section of the device is represented in the Figure 2-14. The red layer represents the piezoelectric device with the imprinted area in orange. The plates are joined together with a speaker (Visaton SC8N), used to actuate the PENG membrane with an acoustic pressure. The speaker is powered by a power amplifier (LA50B from Prism Audio), as described in the Figure 2-15. The power amplifier is powered by a source power Keithley 2231A with a DC ± 5V. An arbitrary function generator Tektronik AFG1062 generates waves function for the speaker through the power amplifier. The PENG is connected in parallel with a variable resistance. This resistive load varies from 10 Ω to 10 MΩ. The PENG inputs an operational amplifier OPA604. This operational amplifier is used to amplify by a hundred time the output voltage of the PENG. It also lowers the noise of the measurement by increasing the ratio signal/noise. It requires a DC power supply of ± 12V provided by a Keithley 2231A.

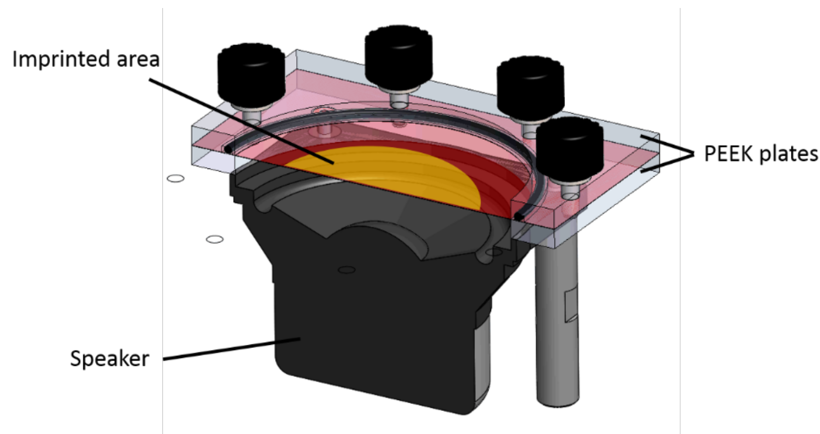

Figure 2-14: Cross section of the large device sketched and clamped between 2 PEEK plates and fixed on a speaker. The red semi-transparent layer with the orange part represent the substrate of the device and the 5 cm diameter active area, respectively.

A vibrometer measures the displacement of the center of the PENG by Laser Doppler vibrometry, based on the Doppler Effect. The vibrometer is composed of a controller with a decoder and a laser unit from Polytec, OFV 5000, DD-900 and OFV 534 respectively. The laser is pointing at the center of the PENG to measure the largest displacement with a resolution close to the nanometer. A drift of the displacement measurement can occur and cutoff some values. Therefore, the function generator triggers the vibrometer to reset the displacement value after each period to avoid cutoff. The displacement is converted into a voltage with a range of 200 µm V^{-1} and a resolution of 60 nm. An Oscilloscope Lecroy Wavesurfer 3024 displays and registers output signals of the function generator, output voltage of the device through the operational amplifier and the displacement measurement from the vibrometer. The Figure 2-16 is a picture of the experimental test bench assembled with the different components highlighted.

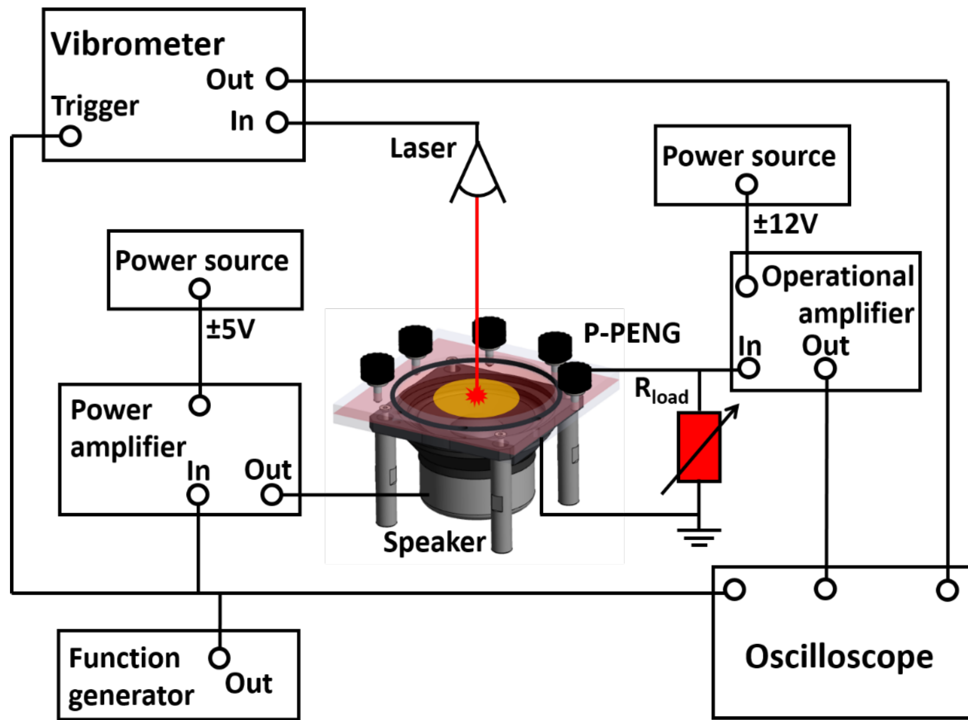

Figure 2-15: Schematic of the setup for the membrane characterization.

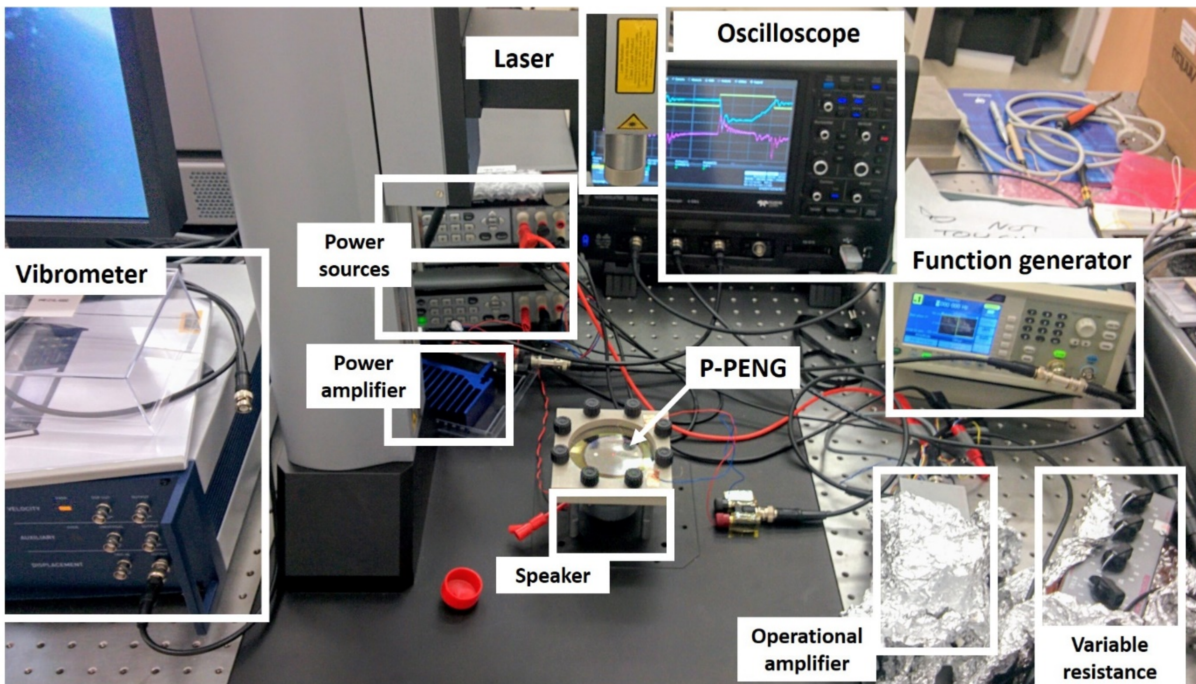

Figure 2-16: Picture of the experimental test bench for large piezoelectric nanogenerator. Labels identify each part of the setup.

2.4. Conclusion

This chapter described the different equipment used for the fabrication of the ZnO piezoelectric nanogenerator. The materials characterization methods are described to focus on the information they have provided in the context of this thesis. For several of them we remind their limitations and/or artefacts allowing to accurately interpret the results in following sections. The description of an original electromechanical test bench used to accurately characterize large piezoelectric nanogenerators is also given.

3. Study of ZnO by Atomic Layer Deposition

This chapter presents the atomic layer deposition of thin films of ZnO. This study sets the necessary basis for the later integration of such ZnO films in piezoelectric nanogenerators. Most parts and the structure of this chapter are similar to a manuscript submitted for publication to *Applied Materials Today*.

3.1. Introduction

In recent years, the development of portable electronic devices focused on new technologies to harvest energy from ambient mechanical energy into electric energy [4], [5], [81]. Piezoelectric nanogenerators and triboelectric nanogenerator show a great potential to harvest ambient energy and are promising to power future portable electronic devices [16], [82]. Performance outputs of nanogenerators depend mostly on the active material chosen [5] and on the device architecture. Lead-free materials for nanogenerators open opportunities for implantable or human-skin wearable devices due to their biocompatibility and environmentally friendly but still need to enhance their overall performances [4]. Zinc oxide (ZnO) is among the lead-free materials considered for PENGs [29], [32] and remains under investigation to improve the performance of PENGs [58].

Wurtzite-type ZnO is a well-known n-type semiconductor with a wide direct gap of 3.37 eV. Within recent years, ZnO has attracted increasing attention because of its high potential for a large variety of applications such as gas sensors, piezoelectric transducers, nanogenerators, ultraviolet light emitters, transparent electronics, optoelectronic, solar cells, photocatalysis, piezotronic and spintronic or optoelectronic applications [6], [83]–[85].

It has been shown in literature that the electrical properties of ZnO strongly depend on defects and that its conductivity can vary from insulator to almost metallic. Undoped ZnO is intrinsically a n-type semiconductor with shallow donor levels attributed to defects such as zinc interstitials, oxygen vacancies and/or hydrogen. When doped, and depending on the growth process, metastable ZnO may also become a p-type semiconductor, although this

point is debate in literature [86]–[91]. Among different types of doping, it has been proposed that doping ZnO with nitrogen (ZnO:N) is the best candidate for p-type semiconductor [92].

Several deposition techniques have been reported for fabricating ZnO films, ranging from pulsed laser deposition, magnetron sputtering, electrodeposition and chemical bath deposition to molecular beam epitaxy or atomic layer deposition (ALD) [37], [93]–[97]. In recent years, ALD has attracted particular interest for integrating ZnO into flexible electronics, which are based on polymers that require a temperature of deposition lower than 100°C [83]. However, experimental reports for ZnO films synthesized by ALD in this low-temperature without a post-annealing process on polymer substrates remain scarce [90], [91], [98]–[106]. To the best of our knowledge, defects free ZnO thin films have been grown by ALD above 140°C [83]. One of the main challenges in the low-temperature regime (<100°C) is the control of optical and electrical properties of ZnO because of uncomplete chemical reactions, low crystallinity and related defects [104]. Also, interesting concepts such as the effect of the purge-time on the growth [107] or the effect of nitrogen doping in plasma-enhanced ALD to change the properties of ZnO thin film are limited to temperature higher than 150°C [108]. Until now, ZnO:N by ALD was processed by plasma-enhanced or ammonium hydroxide that can significantly modify the interface properties of polymer substrates [89]–[91], [108]. So far, no application related to ZnO:N grown by thermal ALD on temperature-sensitive substrate below 100°C without post-annealing process has been reported [89]–[91], [98]–[108]. Such process conditions are mandatory to envisage the deposition on temperature sensitive substrates while keeping a high quality of the thin film.

Our work is therefore motivated by the high potential of low-temperature deposition of ZnO for a variety of applications on temperature- and charge-sensitive supports like insulating polymers. A Conformal thin film by ALD is mandatory for high aspect ratio template. Here, we optimize an ALD process to tailor the n-type resistivity of ZnO, inspired by the former work of Chien *et al.* and Lim *et al.*, highlighting the influence of nitrogen [108], [109]. We investigate a very low-temperature thermal ALD process, combined with the effect of the time of purge with nitrogen as purge gas to incorporate nitrogen into ZnO. We show that crystallized samples can be obtained at temperatures as low as 80 °C and that, even in this regime, the time of purge allows tuning the N-doping level allowing to modify structural, optic and electric properties of ZnO. This significantly impacts the overall performance of the fabricated PENGs.

3.2. Experimental

N-doped ZnO thin films are grown in a laminar-flow thermal atomic layer deposition reactor (ALD, TFS 200 Beneq) on three substrates for characterization: Si, PMMA(2µm)/Si and Pt(100nm)/TiO_2(20nm)/SiO_2(500nm)/Si. Si wafers are used as model substrates for thin-film characterizations, PMMA-coated Si aim at investigating the deposition on temperature-sensitive polymer layer and Pt on a multi-layer on Si is used to remove the Si background signal for some characterization technique like Raman spectroscopy and photoluminescence, and to demonstrate the deposition over a metallic-ended stack. The reactor temperature was set at 80°C. Diethylzinc (DEZ, Sigma-Aldrich) and deionized water are used as Zn precursor and oxidant gas, respectively. A 200 sccm dry nitrogen gas flow is continuously flowing into the chamber to maintain a constant pressure around 5 mbar. One cycle of a ZnO monolayer deposition consists of four steps: 1- DEZ pulse (0.25 s), 2- purge with nitrogen (1 to 20 s), 3- H_2O pulse (0.2 s), 4- purge with nitrogen (1 to 20 s). Both precursors saturate the surface reaction after 5 ms. The process remains in standard ALD regime for purging time above 0.5 s. The thickness of the film deposited is 100 to 165 nm depending on the number of cycles. Table 3.1 presents a summary of the purge time parameters used for the films deposition and the resulting thicknesses. The film thickness is measured by ellipsometry on Si and Pt substrates. The crystallization and texture of the ZnO film is examined by XRD on Si and Pt substrates. The chemical composition is investigated XPS on Si and Pt substrates. Raman spectroscopy and photoluminescence are realized on a Renishaw spectrometer with a 532 nm and 325 nm wavelength laser, respectively, on Pt substrate. Electrical conductivity measurements are performed by 4-point probe on PMMA samples.

3.3. Results and discussion

3.3.1. Chemical composition

The ALD process employed in this work is not in the classical ALD window [77], [83], [105]. A classical ALD window for the growth of oxide materials may be defined by a step-growth of half-a-monolayer of oxide which relies on the complete hydrolysis of precursors fully saturating the substrate surface. For our chemistry, the range of temperature where the reaction is complete between precursors, is typically between 100 and 250°C. In the case of an incomplete reaction between precursors, carbon contamination is expected to appear due to an incomplete reaction of the DEZ at low temperature. Working in an unusual temperature range, we have used X-ray Photoelectron Spectroscopy (XPS) to evaluate the stoichiometry of our different samples and to detect potential contaminations. Table 3.1 shows the XPS stoichiometry before and after *in situ* argon sputtering, which is used to etch a few nanometers. The results indicate a carbon contamination at the top-surface of the thin films, while very interestingly no carbon contamination is observed inside the film indicating a complete reaction of the DEZ during the ALD process at 80°C. The H concentration can be analyzed through a deconvolution of the O1s peak at 532.5 eV, which allows evaluating the oxygen bonds ratio between hydrogen and zinc [77]. We measure a significant concentration of hydrogen into the film after argon sputtering. A similar behavior occurs on a pristine ZnO monocrystal (from MTIXTL) and is actually attributed to the fast hydroxylation of the Ar-sputtered ZnO surface during the XPS scanning. Such a measurement-artefact has been already reported [110]: 6 % of hydrogen concentration typically corresponds to the full passivation of the dangling bonds of the ZnO surface by the residual water molecules of the XPS chamber, when considering a probing depth of 6 nm for the O1s in ZnO [80]. To further assess the hydrogen content into the films, dynamic SIMS analyses have been performed.

Table 3.1: Thickness, XPS and SIMS analysis of ZnO films deposited by ALD for various times of purge. The error bar for XPS is ±1 % atomic. The error bar for the SIMS corresponds to the standard deviation of the average plateau value.

Time of purge (s)		1	3	5	20	Single crystal
Thickness (nm) Number of cycles		155 nm 1000	100 nm 650	155 nm 1000	165 nm 1000	
XPS before sputtering (% atomic)	Zn (±1)	41.1	40.9	41.7	42	23.4
	O (±1)	40.9	41.9	42.1	41.3	32.5
	C (±1)	18	17.2	16.2	16.7	44.1
XPS after sputtering (% atomic)	Zn (±1)	47.9	48.4	48.6	48.4	**50.4**
	O (±1)	45.2	45.6	45.2	44.9	**43.5**
	H (±1)	6.9	6	6.2	6.7	**6.1**
	C (±1)	Below limit of detection				
	N (±1)	Below limit of detection				
SIMS (counts)	H	1273 (±48.5)	915 (±66.8)	888 (±61.2)	857 (±46.1)	
	N	7.46 (±2.47)	4.56 (±2.8)	9.69 (±3.76)	37 (±7.91)	
	C	As low as the substrate value, Below limit of detection				

The detection limit of XPS does not allow investigating the presence of interstitial nitrogen inside the film. For this, we have also turned to SIMS, which is a very sensitive probe of even small doping elements such as hydrogen and nitrogen. Table 3.1 shows that the hydrogen content of the films decreases with increasing purge time from 1, 3, 5 to 20 s. Further to this, SIMS provides evidence for nitrogen doping at a rather low level, below the XPS sensitivity of 1 %. Unfortunately, the quantitative level of doping (i.e. % atomic or concentration of atoms/cm³) is inaccessible but a qualitative comparison through the number of counts per second is realized. The amount of nitrogen lowers for a purge time of 3 seconds and increases for longer purge time. The typical SIMS profile, recorded into our film and as described in Figure 3-1, shows that this nitrogen concentration is constant throughout the whole thickness of our ZnO films (zone 1 & 2 in Figure 3-1a) suggesting that N has been continuously incorporated during the ALD process. Figure 3-1b shows the SIMS profile of the ZnO processed at 20 s of purge on Pt. The SIMS signal of nitrogen is constant except for the surface contamination and when the Pt substrate is reached, where the signal corresponds to the background noise of the detector. Based on the fact that both precursors, diethylzinc and water, are nitrogen free, the variation in the nitrogen concentration is mainly dependent on the purging dinitrogen gas. Carbon contamination is also detected on surface and interface between ZnO and Si substrate (zone 1 & 3) but no more after a few nanometers etched. Figure 3-1b shows a level of carbon in ZnO as low as the Pt substrate, meaning no carbon contamination. The temperature of 80°C is the lowest processed without any carbon contamination reported until now [89], [90]. As a wrap-up, we conclude from XPS and SIMS

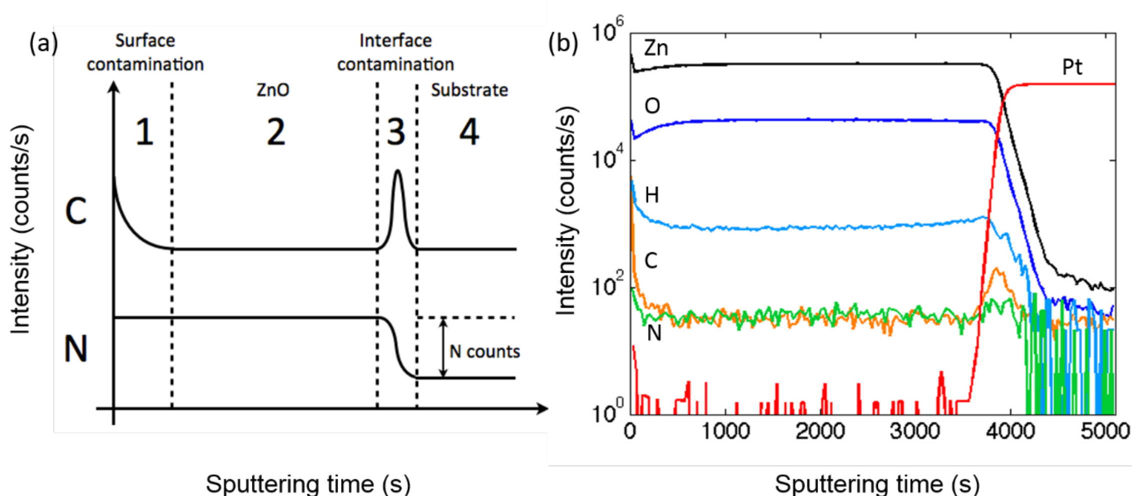

Figure 3-1: (a) Schematic representation of the SIMS profile for carbon and nitrogen content in function of the sputtering time. Zone 1 represents the surface contamination, zone 2 the film content, zone 3 the interface contamination and zone 4 the substrate. (b) SIMS profile of the ZnO processed with a time of purge of 20 s on the Pt substrate. Zn, O, H, N, C and Pt are count with Cs⁺ ions sputtered.

on close stoichiometric ZnO samples which present a low level of doping with hydrogen and nitrogen which can be tuned with the time of purge without plasma process of annealing.

3.3.2. Average structure, local structure and defects

We now turn to the structural properties of our films. According to literature, crystalline ZnO thin films processed by ALD below 100°C are rare [83], [103], [111]. In contrast to this, Figure 3-2 illustrates through the presence of well-defined diffraction peaks that all films, whatever the time of purge, are crystallized. An analysis of the relative intensity of the Bragg reflection shows that the texture is preferentially along the (002) orientation (JCPDS #00-036-1451). Interestingly, we observe a shift of the (002) reflection to higher angles indicating a decreasing lattice parameter with increasing time of purge from 1, to 5 and 20 s. This observation is similar and repeatable for the three substrates but easier to visualize and compare to SIMS on the Pt substrate. The behavior with a time of purge of 3 s is slightly different after the calibration of the intensity on the peak (111) of the Pt (almost no shift of the (002) reflection) and is attributed to the lower signal resolution due to the lower thickness of the film (100 nm). There is no influence of the thickness between 100 and 165 nm and the Scherrer equation determines an average crystallite size around 25(±3) nm for all thin films.

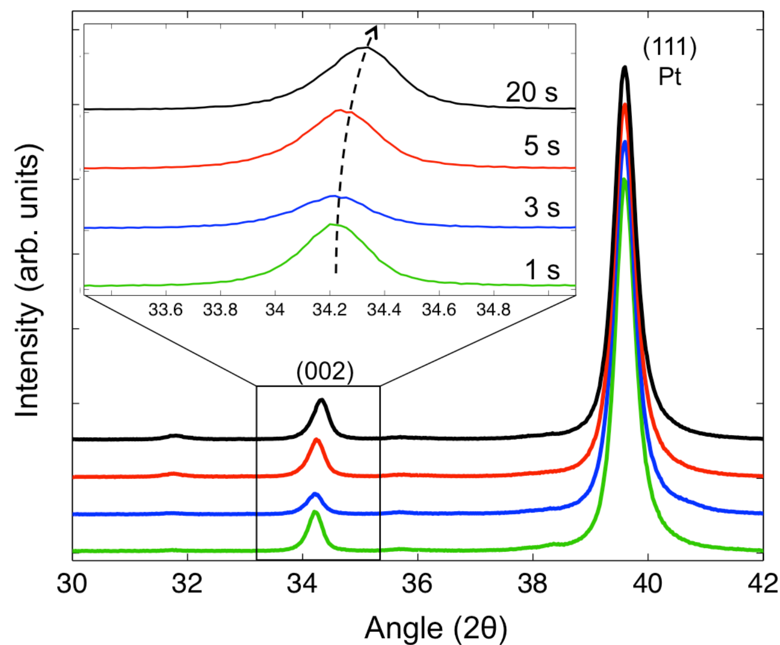

Figure 3-2: X-ray diffraction pattern of ZnO thin films processed by ALD with different times of purge. The inset illustrates a shift of the (002) reflection towards higher diffraction angle with increasing time of purge. All diffraction patterns are normalized to the (111) Pt peak, both in intensity and position.

However, by relating this result with the observed chemical composition of the different films, we observe that the *c* lattice is inversely proportional to the nitrogen content in the films, as illustrated in Figure 3-3, where the *c* lattice parameter is plotted against the nitrogen doping level. Such behavior is reminiscent of literature reports for N-doped ZnO films processed by other chemical deposition techniques [84], [112]. Namely, the work of Park *et al.* discusses the substitution of oxygen by a nitrogen in p-type doped ZnO [92] and concludes that the Zn-N bond is shorter than the Zn-O bond, 1.88 Å compared to 1.93 Å, respectively. On the other hand, other reports suggest that interstitial implanted nitrogen leads to an increase in the lattice parameter of ZnO [113]. Based in this, we suggest at this stage that the nitrogen in our films substitutes oxygen atoms rather than acting as interstitial defects.

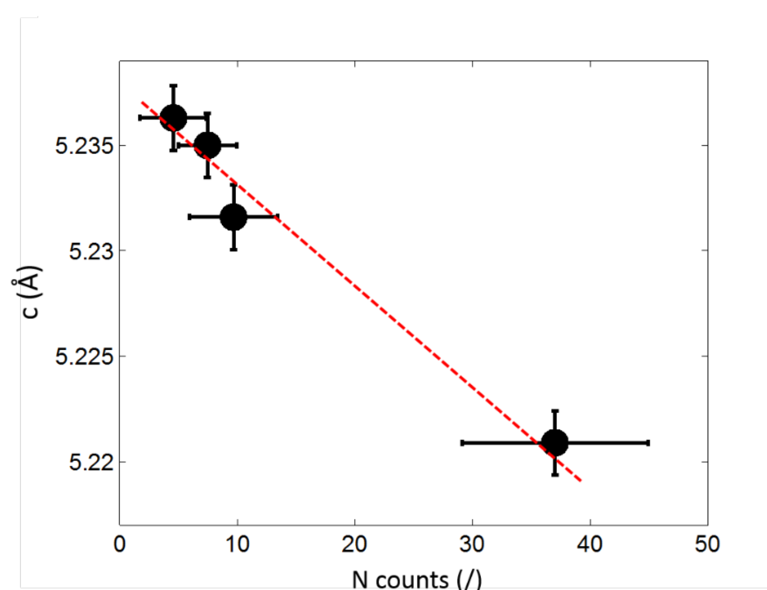

Figure 3-3: Decrease of the c lattice parameter of the wurtzite unit cell of ZnO in function of the nitrogen content by SIMS. The linear red dashed line is a guide to the eye.

The above-discussed chemical composition and average structure requires to be complemented by a view on the local structure and actual position of the nitrogen. Raman spectroscopy and photoluminescence characterization can provide such insights. ZnO on Pt is preferred rather than Si or PMMA/Si substrates because Si and PMMA/Si exhibit a Raman and photoluminescence spectra that hide partially the ZnO spectra.

Wurtzite ZnO crystallizes in a hexagonal C_{6v} space group [114], [115] with four first-order Raman-active phonon modes $A_1 + E_1 + 2\ E_2$, out of which the E_2 modes are reported to display the strongest intensity. The weaker polar modes A_1 and E_1 split into LO-TO components. Further to this, the C_{6v} space group leads to two silent optical phonon modes of B_1 symmetry. Figure 3-4 presents Raman spectra of ZnO films for four different times of purge. Five spectral features are observed at 275, 437, 511, 580 and 620 cm^{-1}. The feature at around 437 cm^{-1} can be assigned to one of the expected E_2 modes [116], [117]. The other expected first-order Raman modes are not observed, likely because they are too low in intensity (A_1 + E_1 modes) or below our spectral cut-off (second E_2 mode). Based on literature, the remaining features are assigned to modes of silent B_1 symmetry (275 and 580 cm^{-1}), to a $2B_1$ harmonic (511 cm^{-1}) and a TA+B_1 combination [118], [119]. We note that the intensities of the silent modes at 275 and 511 cm^{-1} increase with increasing purge time, when compared to the E_2 mode at 437 cm^{-1}, specifically for a time of purge of 5 and 20 s.

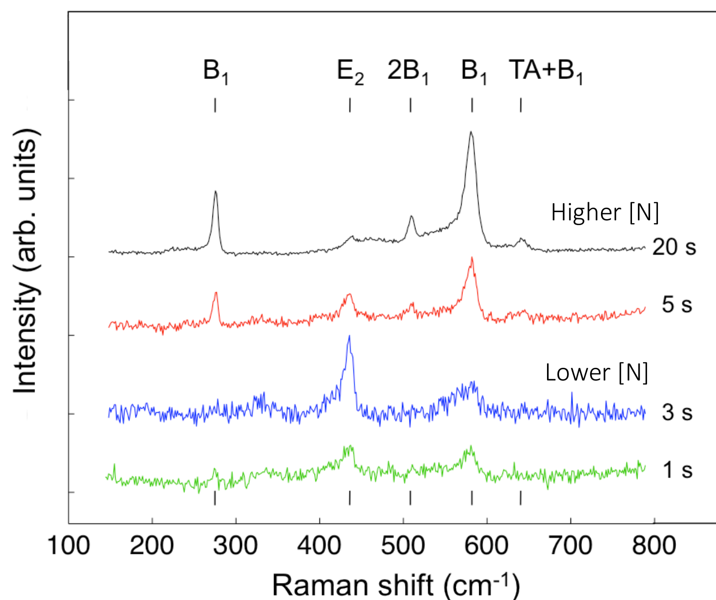

Figure 3-4: Raman spectra of ZnO thin films on Pt substrate for different times of purge by ALD.

The Raman activity of otherwise silent modes has been much discussed in literature. Manjon *et al.* propose that the observation of silent modes in ZnO is due to disorder-activated Raman scattering [118], i.e. some kind of defects breaking the translation symmetry of the lattice. Using zinc isotopes, Friedrich and co-workers observed silent vibrational modes around 275 and 511 cm^{-1} for N-doped ZnO [120]. They assigned the mode at 275 cm^{-1} to the vibration of an interstitial zinc atom bound to a substitutional nitrogen atom on an oxygen site (Zn_i-N_O),

while the mode at 511 cm^{-1} is suggested to be linked to Zn_i-O_i complexes. Gluba *et al.* demonstrated the link between interstitial zinc in the ZnO lattice and the peak at 275 cm^{-1} using zinc isotopes [121]. Finally, Kaschner *et al.* report a proportionality between the nitrogen concentration in ZnO films and the scattering intensity of silent modes, which increases in intensity when normalized to the E_2 mode at 437 cm^{-1} [122]. We observe a similar qualitative trend for our spectra. Finally, a study from Friedrich and Nickel establishes vibrational modes around 1700 and 2300 cm^{-1} as a typical signature of interstitial nitrogen or hydrogen ions on ZnO [123]. In our own spectra, we observe none of these vibrational modes. Based on this and the above reported literature background, we assume that two mechanisms break the local symmetry: nitrogen ions, which substitute oxygen ions and interstitial Zn cations. While we cannot entirely rule out small amounts of interstitial nitrogen ions, we consider that they constitute, if present at all, only a negligible fraction in doping in our ALD process with different times of purge.

A photoluminescence characterization with a 325 nm laser allows investigating the optical and the luminescence properties of our films (Figure 3-5). ZnO is known to exhibit two luminescence features [124], [125]. First, a rather well-defined short-wavelength band positioned around 3.24 eV (383 nm) close to the absorption edge of the monocrystal. This edge luminescence has an excitonic nature and will be discussed in the next section [124]–[126]. The second luminescence band is a broad and complex long-wavelength band, usually located around 2.1 eV (590 nm), in the green spectral band. The emission of this green luminescence is attributed to various defects or impurities in the ZnO lattice and is for all thin films processed by ALD stronger than for the monocrystal. Literature attributes the complex features to zinc vacancies V_{Zn} (3.06 eV), oxygen vacancies V_O (1.62 eV), interstitial zinc ions Zn_i (3.1 eV), interstitial oxygen ions O_i (2.28 eV) and oxygen antisites O_{Zn} (2.38 eV) [125], [127]–[130]. The assignment of the broad luminescence band around 2.1 eV to precise defects is still debated in the community, but it is generally assumed that it results from a combination of the above-cited defects resulting in a broad band [127]–[131]. Qualitatively, our observed luminescence signature provides thus evidence for defects, which in turn corroborates with a defect-activation of silent modes as observed in our Raman spectra. Some impurities can also take part in the defect band like interstitial hydrogen H_i and interstitial nitrogen N_i but, as discussed, our Raman characterization showed none of them distinctly. A luminescence signal arises around 1.65 eV (750nm) and its intensity becomes a well-defined and intense signature for a purge time of 20 s. A study from Stavale *et al.* assigns this luminescence band to oxygen

vacancies, stabilized principally by substitutional nitrogen atom on an oxygen site (N_O) [132]. Its relative intensity in the defect signature is proportional to the content of nitrogen in the ZnO film. This luminescence signal corroborates with our Raman analysis, both showing an increase of defects related to nitrogen in the ZnO lattice.

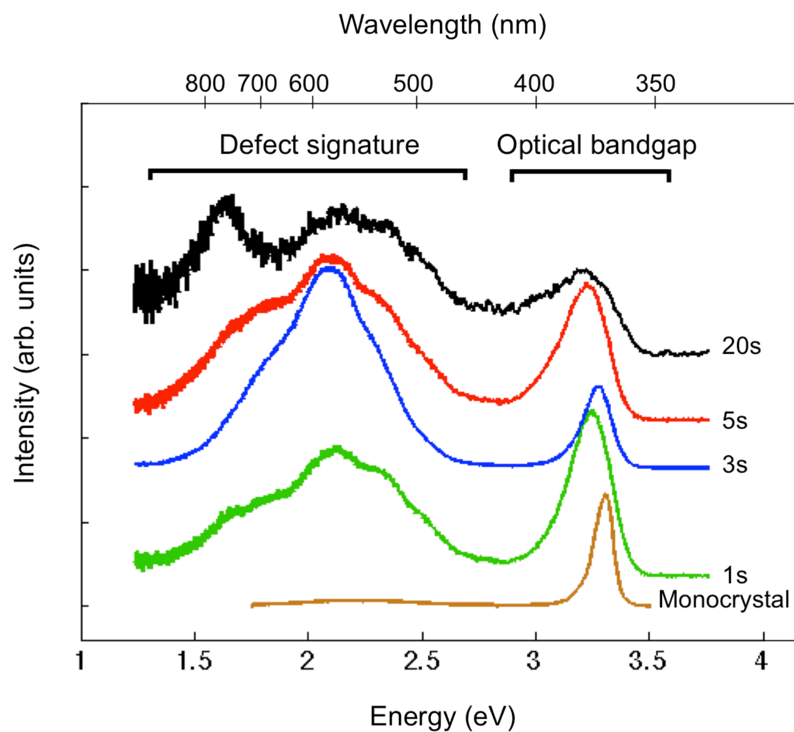

Figure 3-5: Photoluminescence spectra of a ZnO monocrystal and for thin films on Pt substrate for different times of purge by ALD. The intensity of the spectra is normalized and vertically shifted for better inspection.

3.3.3. Optical gap and electronic properties

The above sections have shown how different growth conditions, namely the time of purge, influence chemical and structural properties both at the average and local level. It is now interesting to investigate how the optical and electronic properties are influenced by these characteristics.

In a first step, we will discuss the optical bandgap in the light of the previous sections and then investigate the electrical conductivity. Figure 3-6 illustrates a red shift of about 3 % of the mean value of the excitonic peak that which decreases with increasing nitrogen concentration in the ZnO films. Generally speaking, the shift of the excitonic luminescence band can be due to several mechanisms: the nitrogen substitution of oxygen or intrinsic defects. We first note

that there is a clear correlation between the reduction of the optical bandgap and the nitrogen content. Rodnyi *et al.* report a red shift of the excitonic peak for acceptor impurity like nitrogen [124]. Similarly, Look *et al.* observe a red shift of the excitonic peak for a p-type ZnO doped with nitrogen compared to undoped ZnO, which is probably due to neutral acceptor bound excitation [133]. Additionally, a red shift can be due to intrinsic defects without doping element [126]. Wang *et al.* have shown that a high concentration of oxygen vacancies V_O creates in ZnO an impurity level near the valence band and narrows the bandgap [134]. V_O Stabilized by N_O, as suggested in the luminescence defect signature section, can confirm that both intrinsic defects and nitrogen doping are contributing to this red shift of the excitonic peak.

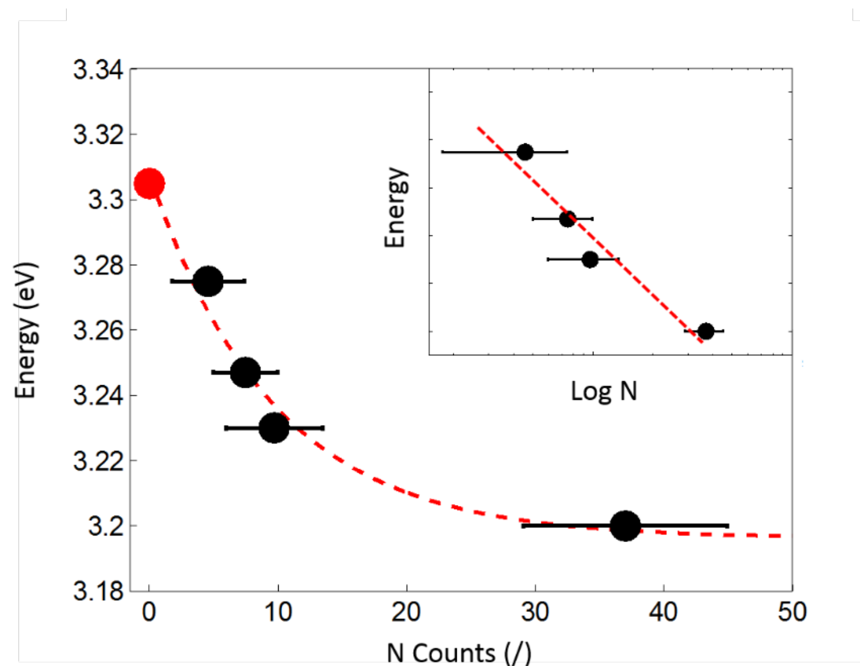

Figure 3-6: Mean value of the excitonic luminescence peak shifting in function of the nitrogen content in ZnO by SIMS. The red data point is the value for a pristine ZnO monocrystal. The red dashed line is an exponential fit and acts as a guide for the eyes for the decreasing values. The exponential red shifting is better visualized in the top right zoom with a logarithmic scale for nitrogen content in ZnO. The experimental and fitting error is smaller than the sized of the dots.

Electrical properties are investigated by 4-point probe measurements for ZnO on PMMA samples and reported in Figure 3-7. The results show a sheet resistivity around 7.8 x 10^2 *Ω.cm* for a purge time of 3 s which is the lowest nitrogen content of the processed films and then increases by several orders of magnitude with increasing nitrogen content. The electrical

characterization of the sample processed with the highest nitrogen content (i.e. 20 s of purge time) reaches the limit of detection, indicating a resistivity higher than 10^6 *Ω.cm*.

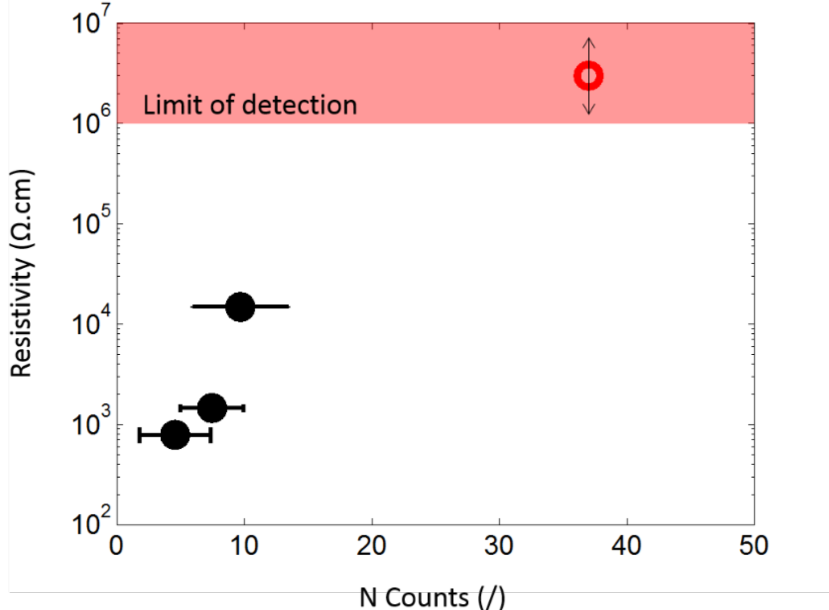

Figure 3-7: Sheet resistivity of ZnO thin films deposited on PMMA in function of the nitrogen content as determined by SIMS. The resistivity of the sample with the highest nitrogen content (i.e. 20 s of purge time) is above the detection limit of 10^6 Ω.cm and only schematically represented by the red open circle to underline the overall trend. The error of resistivity is smaller than the size of the dots.

In literature, ZnO doped samples with more than 1.5 % atomic of nitrogen are mostly investigated for p-type conductivity [112]. One of the main drawbacks of nitrogen doped ZnO is its time stability because of the low solubility of nitrogen in ZnO observed by a lattice relaxation [112], [124]. In our study, the nitrogen amount is below one percent and does not induce a p-type behavior. The electrical characterization six months later on the highest doped sample exhibits the same behavior, attesting to an excellent time stability for ZnO:N. Beside this, several studies show that nitrogen doping at a few percent atomic of ZnO by ALD decreases the electrical conductivity, electron concentration and Hall mobility of thin films [108], [109]. All in all, Figure 3-7 illustrates a surprisingly important modification of resistivity of at least 3 orders of magnitude, when considering the only small content and change of nitrogen doping below 1 at. %. At the present stage, we interpret this increase of resistivity with the nitrogen doping as followed. Zinc interstitials are shallow donors [131] and nitrogen substituting oxygen are interacting with interstitial zinc as demonstrated by Raman spectroscopy. We propose that the presence this Zn_i-N_O complex increases the resistivity of the thin film through the fact that N_O provides self-compensating charges to the donor

behavior of Zn_i, decreasing the charge carrier density. Furthermore, the lattice contraction of the c-axis due to the nitrogen doping leads to a hydrostatic stress that can contribute to an increase of the potential barrier at the grains boundaries due to the piezoelectric effect [135]. The increase of the grain boundary barrier is one of the various scattering mechanisms that control the mobility of electrons in polycrystalline ZnO thin films. However, other interactions with the nitrogen doping are probably contributing to this huge increase of resistivity and need further investigation.

Moreover, an additional characterization technique confirms the previous observations. A preferential texture growth along (002) of ZnO demonstrated by XRD can lead to an anisotropic transport behavior [136]. As the 4-point probe measures the sheet resistivity, the resistivity measurement through the ZnO thin film is performed by resiscope (a scanning probe microscopy technique described in section 2.2.8) with a p-type conductive diamond tip [137].

Another batch of ZnO at 80°C was processed with 500 cycles for different time of purge of 3, 20 and 60 seconds with a thickness of 96, 98 and 105 nm, respectively. The difference of deposition rate between batches is due to conditioning and maintenance of the reactor combined with the non-conventional temperature deposition. However, results from the same batch can be quantitatively compared and from different batches qualitatively compared. Characterization tendencies remain the same between batches.

The resiscope scans a 2 by 2 µm area to measure an average resistance of the ZnO thin film as shown in Figure 3-8. The resistive logarithmic scale varies from conductor to an insulator behavior from 10^2 to 10^{12}, respectively. The homogeneity of measurement exhibits a similar conductivity for all grains. The sample processed at 3 s exhibits a semiconductor behavior with a logarithmic value of resistivity of 7.1, (middle value between conductor and insulator on the log scale). The sample processed at 20 s, previously demonstrated with a higher nitrogen doping, increases the resistivity with a logarithmic resistive value of 7.9. The last sample, processed with 60 s exhibits a nearly insulator behavior with a logarithmic resistive value of 9.4.

Resiscope measurements confirm an isotropic tendency of an increasing resistivity with the time of purge (i.e. nitrogen doping), even until 60 s of purge, with an enhanced effect. The increase of more than 2 orders of magnitude between 3 and 60 s enables a controlled switching from semiconductor to insulator behavior of ZnO.

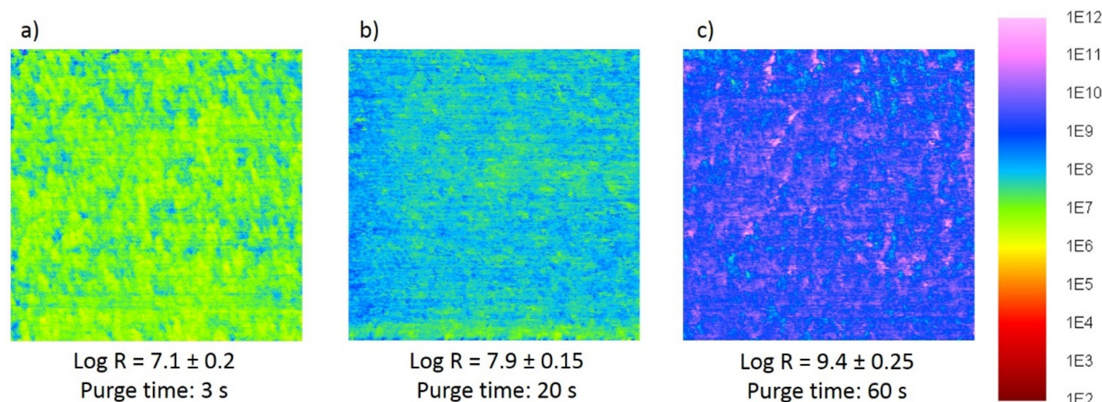

Figure 3-8: Resiscope measurement of different N-doped ZnO processed by ALD with a time of purge of (a) 3 s, (b) 20s and (c) 60s. 2 by 2 µm area of scan.

3.3.4. Piezoelectric properties

A piezoelectric behavior of ZnO is required for a piezoelectric harvesting device. The piezoresponse force microscopy (PFM) provides information about local piezoelectric behavior of ZnO. The local piezoelectric coefficients are often used as a figure of merit for the crystal quality [138]. PFM characterizes the polycrystalline ZnO processed by ALD on Pt substrate on 1 by 1 µm area. The Figure 3-9 shows the PFM characterization of ZnO processed with 20 s of purge time. The area is scanned twice to image the out-of-plane and the in-plane piezoresponse. The amplitude of the piezoresponse determines the piezoelectric coefficient (Figure 3-9b,e), as mentioned in the section 2.2.8, and reported in the Table 3.2. These values of d_{33} are smaller than the 10 pm/V for bulk ZnO [19] and can be explained as followed.

The size of the crystallites determined by XRD are around 25 nm, each crystallite owning a different domain of polarization due to the crystallographic properties of Wurtzite ZnO. The domain size can therefore be smaller than the tip radius of 20 nm. The piezoresponse averages several domains deflection, resulting a decrease of the value when opposite polarization orientations cancel each other. Furthermore, the inhomogeneous electric field underneath the tip deforms non-uniformly the sample up to three times the tip radius [139]. The consequence is an average deflection measured of several domains through the depth. These two considerations, the non-homogeneous electric field and the small size of crystallites/domains can explain this low piezoelectric value of coefficient. It is thus not

possible to extract a value of piezoelectric coefficient from these polycrystalline ZnO thin films.

Only qualitative information can be extracted from PFM measurement. The out-of-plane and in-plane phases of the piezoresponse image the different domains orientation near the surface (Figure 3-9c,f). It shows a various size of domains randomly oriented. Only a macroscopic piezoelectric characterization can extract a reliable piezoelectric coefficient.

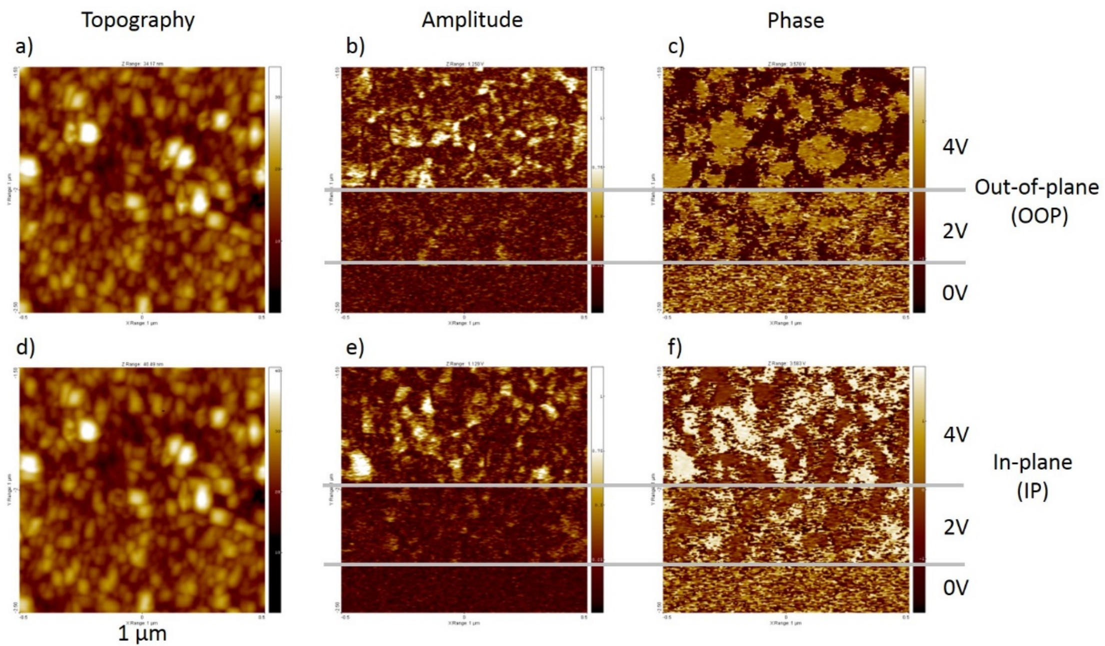

Figure 3-9: 1 by 1 µm PFM scan of a polycrystalline ZnO:N. a-c) Out-of-plane PFM. d-f) In-plane PFM. (a) & (d) Topography of the OOP and IP scanning the same area. b) The amplitude response of the OOP from 0 to 4V. c) The phase response of the OOP from 0 to 4V. e) The amplitude response of the IP from 0 to 4V. f) The phase response of the IP from 0 to 4V.

Table 3.2: Piezoelectric coefficient d_{33} in pm/V of ZnO thin film processed for different time of purge by ALD. Out-of-plane and In-plane coefficient are averaged for different measured area.

	1 s	3 s	5 s	20 s
Out-of-plane	0.074 (±.004)	0.090 (±.006)	0.132 (±.012)	0.147 (±.022)
In-plane	0.24 (±.015)	0.18 (±.021)	0.33 (±.019)	0.23 (±.015)

3.4. Conclusion

In this chapter, we have shown that a low-temperature ALD process, combined with the effect of the time of purge using a nitrogen gas, can produce ZnO thin films with nitrogen doping level below 1 %. Despite a very low deposition temperature of only T = 80 °C all investigated samples are crystalline, as attested through the presence of well-defined Bragg reflections. A thorough chemical and structural analysis illustrates that the time of purge allows tuning the N-doping level which, despite being low, affects both the long-range and short-range structure. As common in ZnO, Raman and luminescence spectroscopy suggest a complex defect structure, characterized by nitrogen ions which substitute oxygen ions and by Zn cations on interstitial sites. Interestingly, even the low level of doping, and the associated presence of N_O-Zn_i complexes, allow tuning the sheet resistivity of ZnO films by several orders of magnitude. Piezoelectric behavior attests of a good quality ZnO exhibiting an interest in piezoelectric devices.

All in all, our study shows that crystallized N-doped ZnO films can be obtained at temperatures down to 80°C, opening the door for the deposition of ZnO on temperature-sensitive supports, with the option to tune structural, optic and electric properties for a variety of applications.

4. P-PENG fabrication, electronic engineering and output performances

4.1. Introduction

This chapter introduces the electromechanical optimization of the design of the new kind of Patterned-PENG (P-PENG) fabricated in this thesis. This approach based on finite-elements-modeling is reconsidered along the chapter based on the experimental results. The versatility of the device engineering relies on the NIL that accurately controls the aspect ratio and the density of ZnO NWs grown by ALD. The transport properties and the local structure of ZnO are finely controlled to optimize the performance via the tailoring of the nitrogen doping of polycrystalline ZnO NWs. Therefore, first devices based on contacts relying on a p-n junction or a blocking barrier are characterized. A specific electronic setup is developed for an accurate characterization of performances and to reliably compare different devices having intrinsically different nitrogen doping in ZnO. To the best of our knowledge, this is the first report on the growth of ZnO NWs in a polymer template using a simple, scalable and low-temperature process based on NIL and ALD which has the potential to scale-up the manufacturing of flexible P-PENGs.

4.2. P-PENG mechanical design based on finite element modelling

The pattern of the stamps used for NIL determines the shape of the ZnO NWs. The design of this pattern is optimized to maximize the coupling of the mechanical deformation with the voltage output when considering only the direct piezoelectric effect of ZnO pillars. The matrix of ZnO:PMMA can be seen as a composite material, which can be simulated through finite element modelling (FEM) to optimize the electromechanical response. As a matter of

simplification, the software COMSOL, COMputer SOLution, considers ZnO as a single monocrystal. The c-axis of polarization points up and a constant force is applied as described in Figure 4-1a. A linear piezopotential appears between the top (blue in Figure 4-1a) and the bottom (red in Figure 4-1a) of the ZnO NW and an output voltage (ΔV) of the matrix ZnO:PMMA is calculated. Two key parameters are taken into account to maximize the output voltage: the aspect ratio of ZnO NWs and the pitch between each NW.

First, by FEM and experimental observation of ZnO NWs, it is shown that an increasing aspect ratio leads to an increase in the output voltage [140], [141]. However, a high aspect-ratio larger than 4 remains challenging for our NIL process at the nanoscale [142]–[145]. Several limitations and reliability of the technique usually appear in such a range of aspect ratio. Patterns like protrusion pillars, can break off during the demolding process because of the frictional forces related to the large contact area between the rigid stamp and the resist [142], [143]. The polymer resist can detach from the substrate with the same mechanism. On the contrary, an incomplete filling of the pattern can be driven by a dewetting process of the resist [146]. Soft stamps as polydimethylsilixane (PDMS) could be an alternative at the microscale but they are subject to paring, buckling and collapsing, and thus become unreliable at the nanoscale [145]. Recent works demonstrate a high aspect ratio (>10) at the nanoscale with unconventional techniques and customized patterned for particular applications [142], [144], [147]. Taking into account these considerations, an aspect ratio of 10 is usually beyond the technological limit of the thermal nano-imprint lithography. Reaching the printing of high aspect ratio of 10 remains a challenging process at the nanoscale. Nevertheless, in our work, we have purposely chosen to address this challenge by selecting NWs with a width and a length of 200 nm and 2 µm, respectively.

Once the aspect ratio being fixed at 10, the pitch is optimized with a constant stress of 10 MPa applied along the z-axis, starting from zero (i.e. a film of ZnO) to infinite (i.e. a film of PMMA with one ZnO NW). Figure 4-1b shows that the modelled optimum is about a 640 nm pitch, giving a periodicity of 840 nm. Moving from a square to hexagonal ZnO lattices does not affect the voltage output by more than 1 %. The mold processing leads to a truncated conical shape to facilitate the demolding process and avoiding any break off (Figure 4-2b). The average diameter of pillars is 200 nm and this leads to a top and bottom diameter of 120 and 400 nm, respectively.

This truncated conical shape drives a non-uniform stress along ZnO NWs under pressure. A strain gradient is induced and a flexoelectric effect may appear [148]. Flexoelectricity is a

property of dielectric materials to be polarized when subject to an inhomogeneous strain. This effect could add a contribution to the piezoelectric effect but is still ineffective in our case. Indeed, using the model of the truncated structure under inhomogeneous deformation [149], it results in our geometry to a flexoelectric contribution of only 6 nC m^{-2}, which is insignificant compared to the e_{33} piezoelectric coefficient of ZnO of 1.55 C m^{-2} [150].

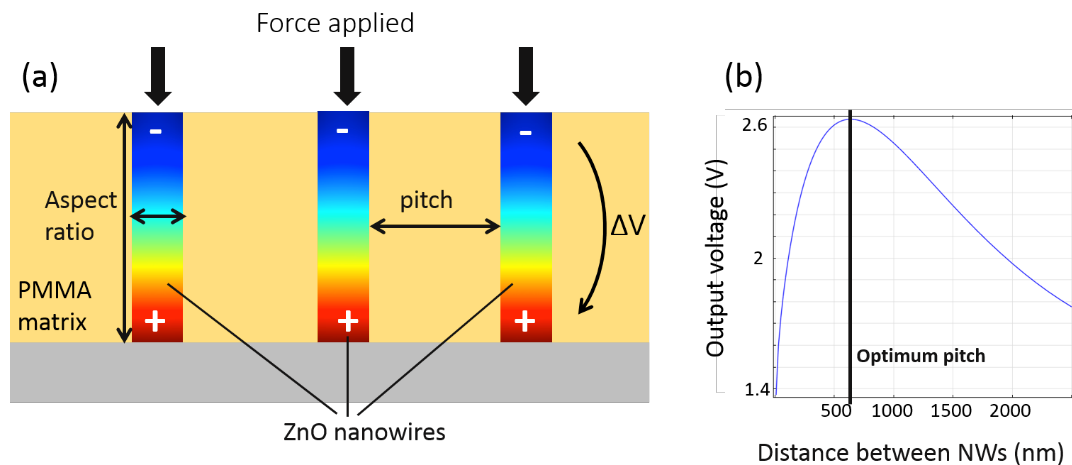

Figure 4-1. a) Schematic of the finite element modelling the P-PENG working principle. A negative piezopotential appears in the top (blue) and increases linearly to the grounded bottom (red) NW. An output voltage ΔV is generated from the applied force. b) Optimization of the pitch for a locked aspect ratio of the ZnO NWs in the PMMA matrix.

4.3. Device engineering

The versatility of the NIL and ALD allows developing a device platform that enables the use of various substrates and difference design of devices architecture. In our work, we rigorously compare electrodes contacts relying on the electrical engineering of a blocking barrier and a p-n junction. Therefore, several substrates and bottom electrodes are investigated. The here used stiff substrates are silicon, Pt(100nm)/Al_2O_3(100nm)/Si and Pt(100nm)/ TiO_2(20nm)/SiO_2(500nm)/Si, while the flexible substrates are ITO(100nm)/PET (60 Ω □$^{-1}$) and Pt(100nm)/PET. The processing of P-PENGs starts by spin coating 2 µm thick PMMA on the substrate, as shown in Figure 4-2a. After evaporation of the solvent, a silicon mold covered with an anti-sticking layer is hot pressed against the PMMA film. The mold, represented in Figure 4-2b, has a truncated conic shape with an average diameter of 200 nm (± 30 % width variation from the top to the bottom). 40 bars are pressed at 155°C for 120 s, 50°C above the

glass-transition temperature of PMMA. Then, the substrate and mold under pressure are cooled down to room temperature before releasing the pressure and demolding (Figure 4-2a(i) & 2c). The truncated conical shape of the pattern helps the demolding process without damaging the holes. One can also highlight the lack of any residual PMMA layer at the bottom of holes avoiding the use of plasma cleaning. After the NIL, ALD fills the PMMA matrix with zinc oxide doped with nitrogen (Figure 4-2a(iii) & 2d). Diethylzinc and water are used as zinc and oxidant precursors, respectively. The doping of ZnO with nitrogen stems from dinitrogen, used both as purging and carrying gas (see section 3.2). The ALD is processed at a temperature of 80°C to prevent the melting or the swelling of the PMMA pattern. The thickness of the so-deposited ZnO can be varied between 100 and 150 nm by changing the temperature and the number of cycles of the ALD process allowing to completely fill the cavities. This reproducible platform is the cornerstone of the device engineering that is thoroughly studied. Indeed, different deposition techniques and materials are possible for the electrical contact of ZnO wires. A p-type polymer PEDOT:PSS is spin-coated for a p-n junction or an insulator material Al_2O_3 is deposited by ALD as a capacitive barrier for a blocking contact (Figure 4-2a(iv)). Finally, a top electrode is sputtered or evaporated to complete the stack (Figure 4-2a(v)).

As a concrete example of the versatility of our platform combining NIL and ALD, Figure 4-2e shows a FIB-SEM image of a different device architecture with a substrate of silicon, a passivation layer interfacing the bottom electrode ($Pt/Al_2O_3/Si$), the PMMA and ZnO composite and a top electrode of Au.

The stamp-shape and the conformal ZnO deposition by ALD exhibits a different geometry than the one previously modeled by finite elements calculations. Therefore, the experimental geometry is integrated in the COMSOL simulation to evaluate the influence of such a geometry on the piezoresponse. We compare two different geometries. The first one is the simplified model of a ZnO NW in a PMMA matrix, covered with a thin film of ZnO due to the conformal ALD process (Figure 4-3a). The second is the truncated conic shape NW with the same stamp dimensions (Figure 4-3b). A 2D axisymmetric model is used with similar initial conditions for both geometries. The bottom of the structure is fixed and grounded. A boundary load of 1 MPa stress is applied on the top of the nanostructure along the z-axis Figure 4-3c-d. Here, ZnO is considered monocrystalline with the c-axis pointing along the z-axis to simplify the model. It is assumed that a polycrystalline ZnO would give a comparative behavior between the different geometries. Figure 4-3 c & d show the simulated piezopotential distribution along the circular ZnO NW and the ZnO NW with a truncated conical shape, respectively. Absolute maximum voltage of 0.248 V and 0.219 V are extracted on the top of each modeled ZnO NW.

A revolution of the 2D axisymmetric model displays a 3D representation in Figure 4-3 e & f. The maximum piezopotential decreases by 11.7 % between the circular NW and the truncated conic shape NW.

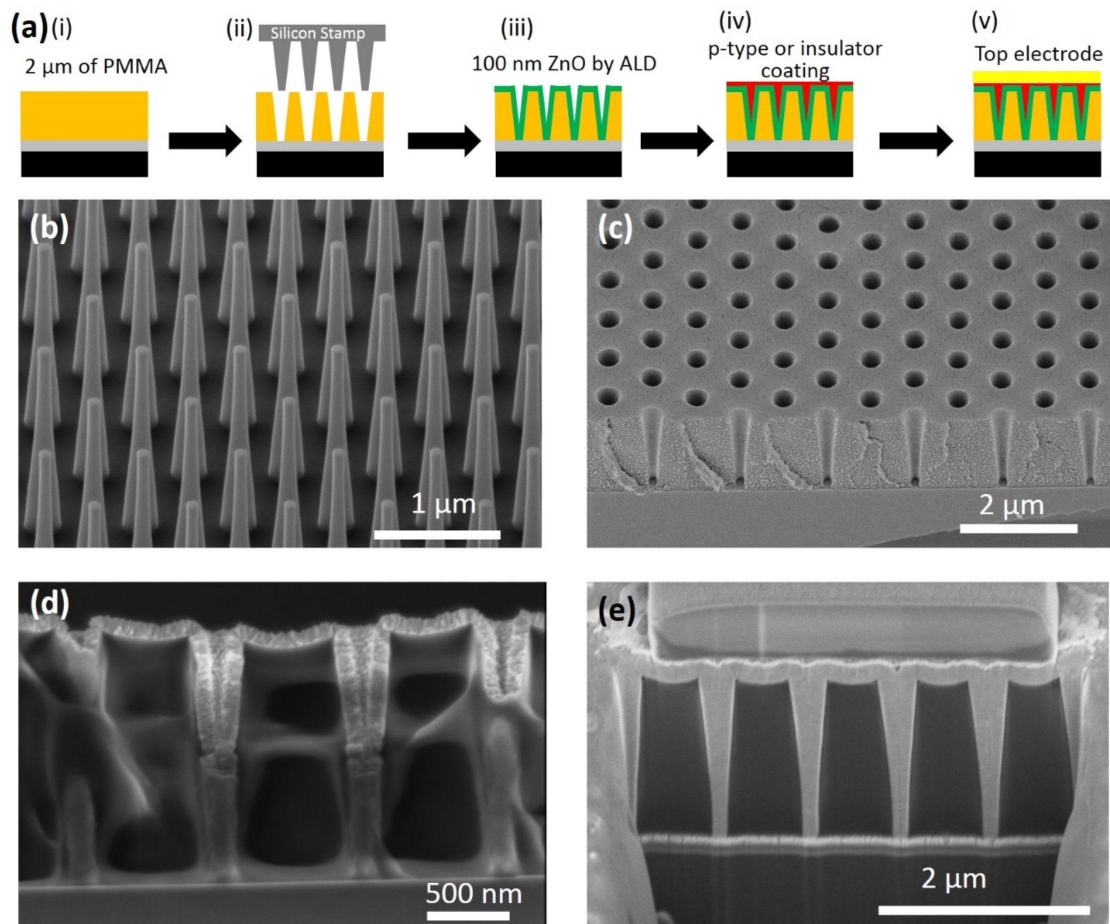

Figure 4-2. a) Flowchart of the P-PENG fabrication. i) Spin coating of PMMA. ii) Nano-imprint lithography. iii) ZnO deposition by ALD. iv) PEDOT or Al_2O_3 deposition by ALD. v) Top electrode deposition. b) SEM image of the silicon stamp for NIL. c) SEM image of the nano-imprinted PMMA. d) Cross section SEM image of the half-filled patterned PMMA with ZnO by ALD. e) Cross section SEM image realized by FIB of ZnO nanostructures in a PMMA matrix.

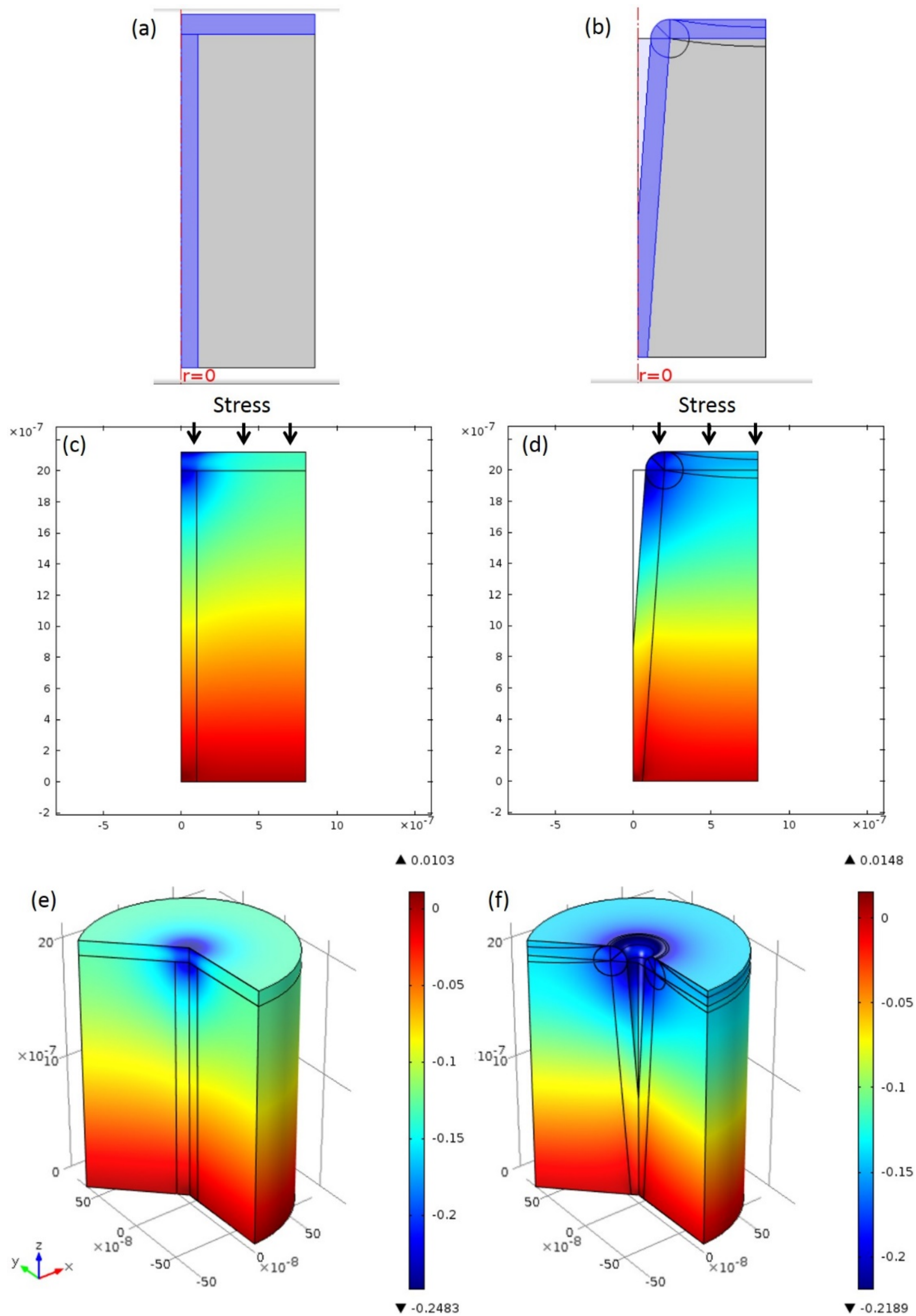

Figure 4-3: COMSOL simulation for geometry adaptation. a-b) 2D axisymmetric modeling along the red dashed axis of the geometry with ZnO represented in blue and PMMA in grey. a) ZnO nanowire with a cap laye of ZnO. b) Truncated conic shape ZnO nanostructure. c-d) Piezopotential distribution in the ZnO:PMMA matrix under a stress applied on top for the geometry (a) & (b). e) 3D representation of the piezopotential distribution of the 2D axisymmetric revolution of the ZnO nanowire (c), in V. f) 3D representation of the piezopotential distribution in V of the 2D axisymmetric revolution of (d).

4.4. Morphological and structural properties

The low-temperature process could in principle lead to non-piezoelectric polycrystalline ZnO and thus motivate in-depth structural characterizations of ZnO NWs. Figure 4-4a is a SEM top view of ZnO deposited on the PMMA template and shows ZnO grains of various size and orientation on the top surface. Figure 4-4b shows the SEM cross-section of the upper edge of a half-filled hole with ZnO. Interestingly, the preferential texture of ZnO grains seems to grow normal to the surface of PMMA, even inside holes. A cross section of the matrix ZnO:PMMA with top and bottom electrodes is realized by a focus ion beam (FIB) and observed by SEM (Figure 4-4c). A cap of Pt is deposited by FIB before using Ga^{+} for etching. Each false color represents a different material component for an easier visualization of the stack. This cross section confirms a highly conformal ZnO thin film deposition by ALD and a complete filling of PMMA cavities. X-ray diffraction confirms ZnO in a wurtzite structure, with a preferential crystalline orientation along the [002] direction, similar to ZnO thin film deposited on a flat PMMA substrate. TEM images of one entire pillar shows that the ZnO NW is polycrystalline throughout the whole cavity, with a crystallite size that varies from 25 nm at the top to around 15 nm at the bottom. Dark field TEM exhibits a random texture of ZnO NWs, selecting different orientation of grains with particular c-axis orientation, as shown in Figure 4-6. SEM and TEM confirm the polycrystallinity of ZnO NWs with a random texture. Tapping AFM in Figure 4-4e further reveals a donut-shape topography on top of NWs, which arises from the PMMA in reaction to a concentric stress of the ZnO around the inner top NW. The ALD leads to a modification of topography on the top of ZnO pillars (arrow in the center of Figure 4-4b). Indeed, pillars exhibit V-shape on their top with a circular excrescence leading to the donut-shape when observed in top view. This change of topography may impact the piezoelectric response of the NW; this is discussed at the end of this section. In spite of a laser-spot-resolution larger than the size of NWs, the mapping by overlapping point by point Raman spectra evidences ZnO NWs versus the PMMA matrix **(**Figure 4-4f**)**. One can notice that the spectrum of ZnO NWs shows the same fingerprint than N-doped ZnO thin films studied in section 3.3.2.

All-in-all, the characterization by SEM, TEM, XRD and Raman spectroscopy suggests high-quality polycrystalline continuous N-doped ZnO conical NWs with a donut-shapes on top.

PFM measurements confirm qualitatively the piezoelectric behavior of the integrated ZnO NWs. In-plane and out-of-plane piezo responses have been clearly detected (Figure 4-5), but a quantitative analysis of the data is unreliable because of the soft substrate (i.e. PMMA), which leads to artefacts into the deformation mechanism.

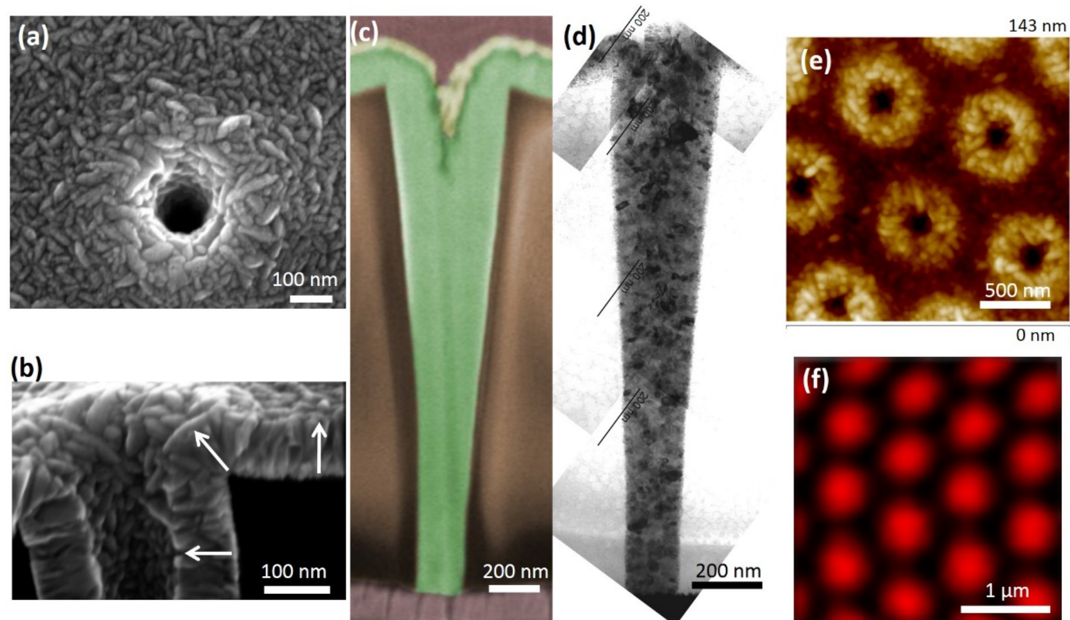

Figure 4-4: a) SEM image top view of the half-filled polycrystalline ZnO NW. b) Cross section SEM image of the ZnO half-filled NW. Arrows indicate the preferential normal growth of the ZnO. c) FIB-SEM cross section image in false color. From bottom to top: red for Pt, orange for PMMA, green for PMMA, yellow for Au and red for FIB Pt. d) TEM image of polycrystalline ZnO NW. e) AFM topography of the donut-like shaped ZnO NW. f) Mapping from point-by-point Raman spectra. The red areas are the signature of N-doped ZnO in the deep cavities, leading to a larger scattering volume, while the signal is almost absent on the top flat parts.

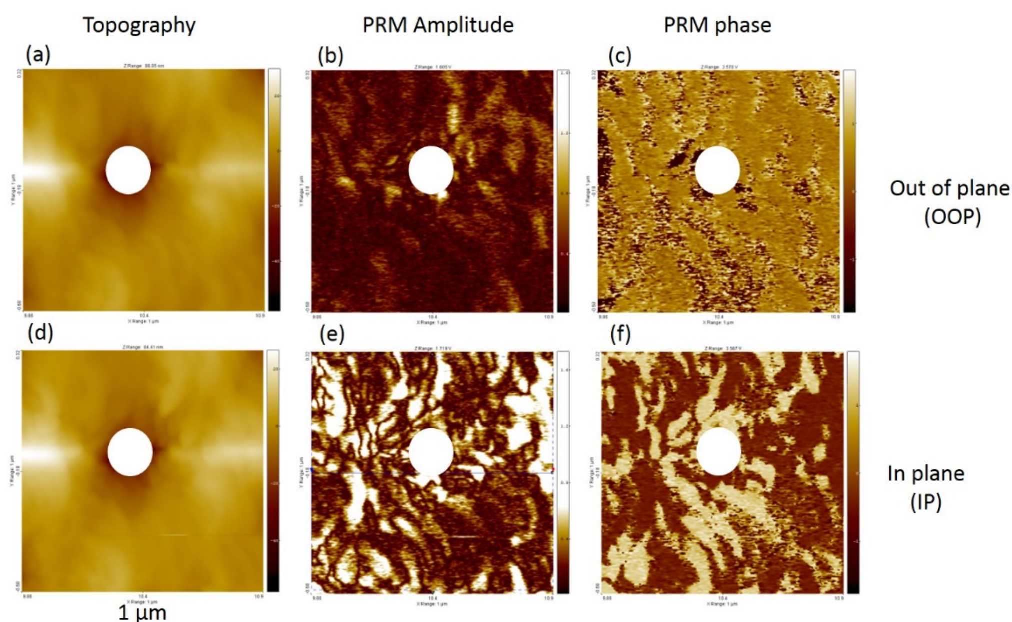

Figure 4-5: PFM response of ZnO NW at 4V characterized in-plane and out-of-plane. The white circle represents the centered hole of the NW. a & d) Topography of the ZnO NW. b) Out-of-plane PRM amplitude. c) Out-of-plane PRM phase. e) In-plane PRM amplitude. f) In-plane PRM phase

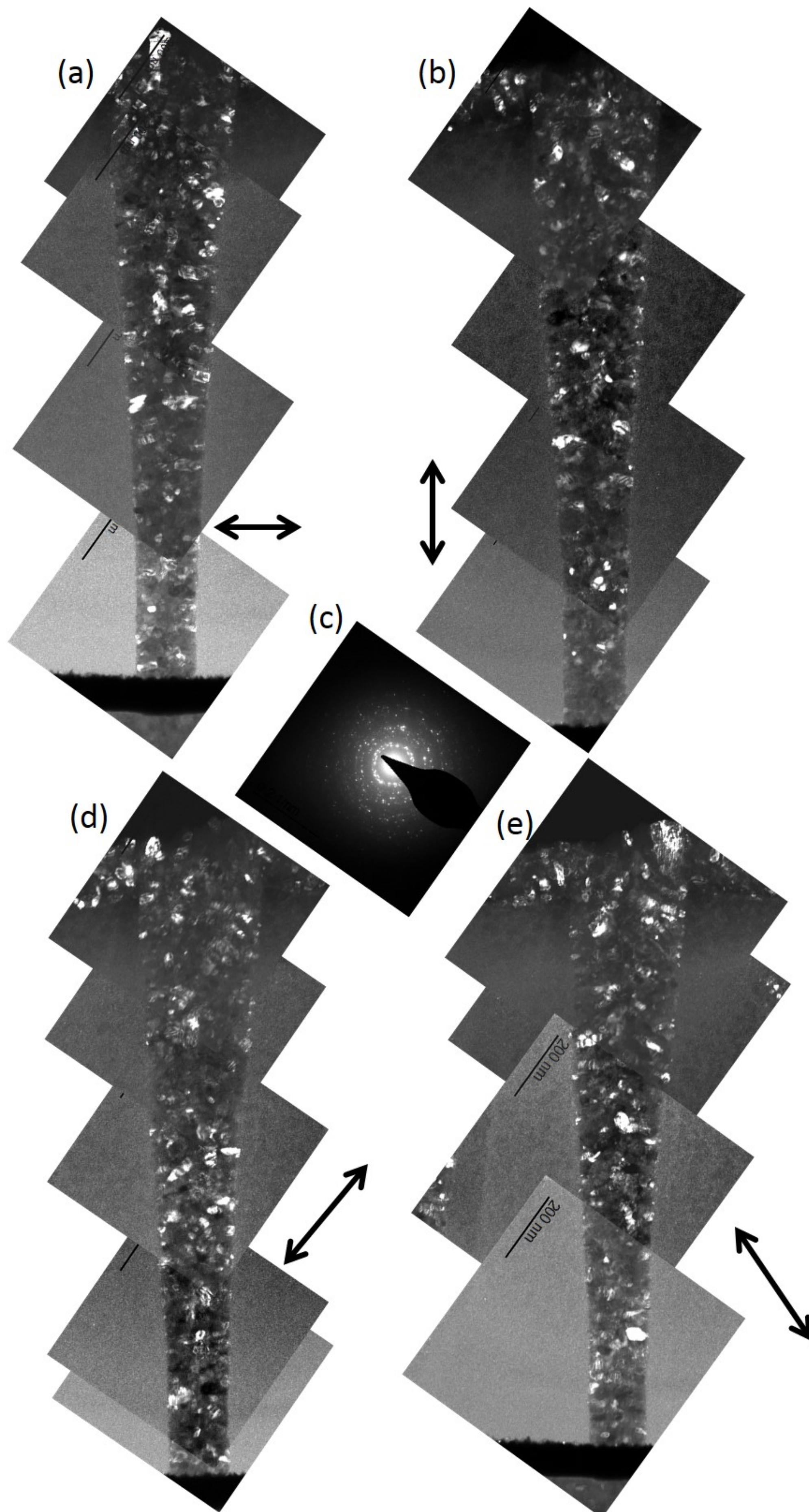

Figure 4-6: Dark field TEM of the same ZnO nanostructure for different c-axis orientation (002). a,b,d,e) The arrows point out the orientation of bright crystallites. c) Diffraction pattern for all orientation.

We already highlighted that ZnO NWs exhibit a donut-shape topography that was not envisaged in our COMSOL model. Therefore, this latter has been updated to model the piezoresponse of a constant stress of 1 MPa applied on a donut-shape ZnO truncated and conical NW. The same methodology is applied and the modeled piezopotential is shown in Figure 4-7. The truncated conic shape NW with a donut-shape topography exhibits an absolute maximum piezopotential of 0.235 V. The donut-shape increases the maximal piezopotential by 6.8 % compared to the simple truncated conical. In conclusion, the maximal piezopotential drops from 0.248 to 0.235 V when perfectly circular ZnO NWs are compared to truncated conical NWs having a donut-shape on top.

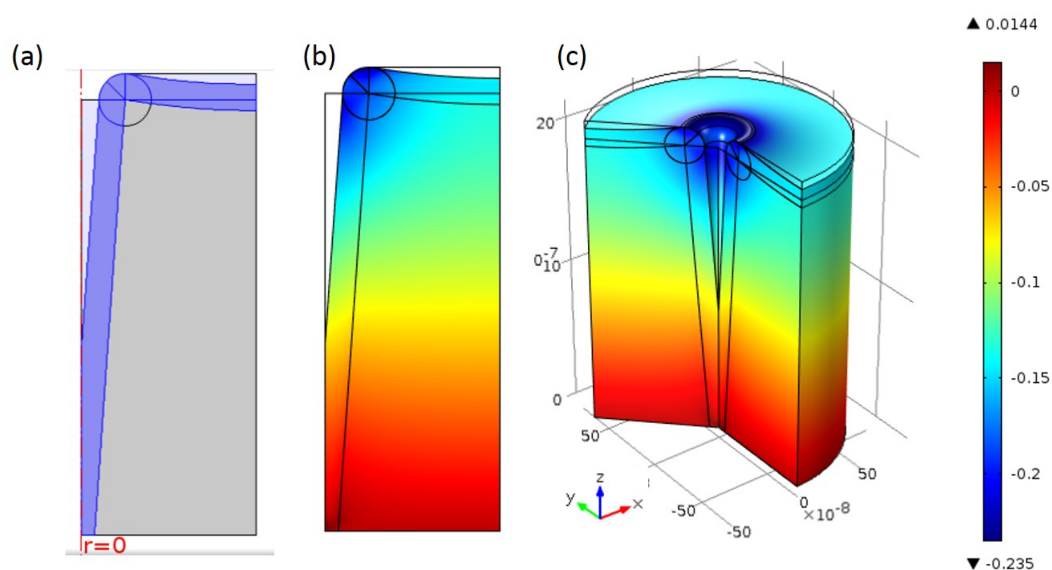

Figure 4-7: Geometric influence of the ZnO NW topography on the output voltage with a conic truncated shape and a donut-like topography. a) 2D axisymmetric modeling along the red dashed axis of the geometry with ZnO represented in blue and PMMA in grey b) Piezopotential distribution in the ZnO:PMMA matrix under a stress applied on top for the geometry. c) 3D representation of the piezopotential distribution of the 2D axisymmetric revolution of the ZnO NW

4.5. P-PENG electronic engineering and output performances

In our work, we have assessed in a first phase P-PENGs based on a Schottky barrier given by the direct deposition of Pt on ZnO NWs showed some limitations. The reproducibility of the Schottky barrier over all ZnO NWs significantly fluctuates leading to shortcut or electrical output instabilities. As stated by Hu *et al*., PENGs also encounter mechanical reliability issues on the hard contact metal/ZnO after cycling, this uses to modify the interface states between ZnO and metal [18]. Some post-process like plasma or annealing on ZnO are often required to ensure a reliable Schottky contact [59]. This is not always compatible with fabrication processes. Based on the random reproducibility of our Schottky barrier between polycrystalline ZnO NWs and Pt, others electrical architectures are rather investigated. They are based on a p-n junction and a blocking barrier electrical engineering.

4.5.1. p-n junction P-PENG

A first device is processed with a bottom electrode of Pt of 100 nm sputtered on a flexible substrate of PET, acting as an ohmic contact. PEDOT:PSS of 2 µm is spin coated on top of the ZnO:PMMA NWs to create a p-n junction in ZnO, as previously demonstrated by Briscoe et al. [61]. In this case, a top electrode of Ti/Au (10/50 nm) is evaporated to ensure a robust electrical contact. Figure 4-8b sketches the p-n junction architecture.

Energy harvesting performances are determined by manually bending devices while measuring the output voltage in a 1 MΩ impedance, R_{load}. The device has a 5 x 5 mm² active area with patterned ZnO NWs (Figure 4-8a). The stack is clamped as close as possible to the anchor where the stress is the most important as shown in Figure 4-8c. The initial state is bending down the device where the matrix of PMMA and ZnO NWs is under tensile stress with a non-homogeneous distribution. Then, the end of the device is released and oscillates up and down with a damping effect. The output voltage oscillates between plus and minus 200 mV and softens with the damping factor mainly related to the flexible substrate (Figure 4-9).

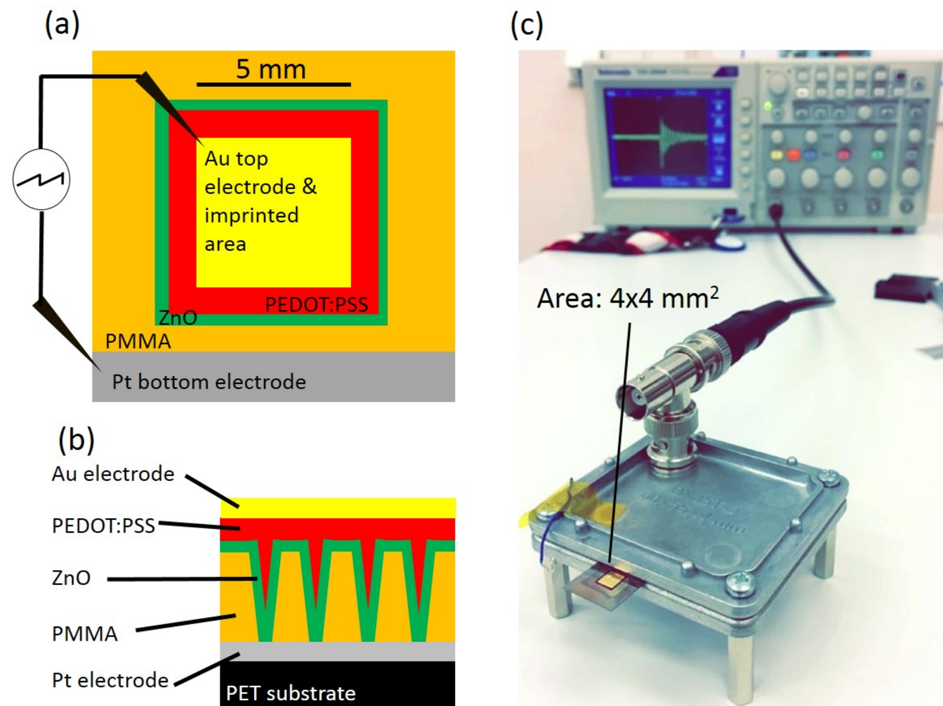

Figure 4-8: a) Schematic top view of the P-PENG and the electronic setup. b) Schematic cross section of the architecture of the P-PENG. c) Experimental setup for the bending characterization. P-PENG is clamped by its bottom electrode in the substrate holder.

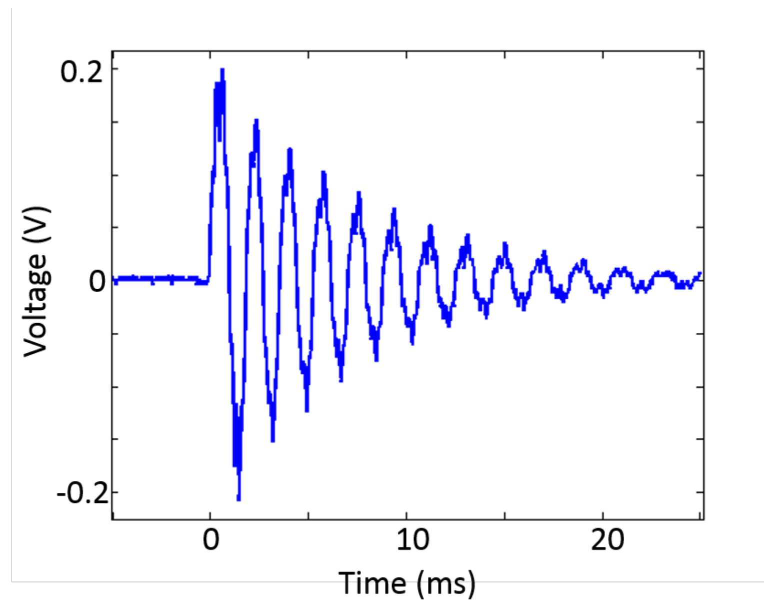

Figure 4-9: Voltage output of the P-PENG trough a 1MΩ load.

The P-PENG equivalent electrical model is schematized in Figure 4-10 with three components in parallel: I_{piezo} as the source of the piezoelectric current, C_i as the static capacitance and R_i as the leakage resistance [151]. This model is appropriate because polycrystalline ZnO NWs react like the classical behavior of piezoelectric ceramic when ZnO sufficiently resistive [152]. In that case ZnO acts as a dielectric medium instead of a semiconductor [153]. On the contrary, devices using semiconducting ZnO, as ZnO NWs obtained by Wang *et al.*, rely on a modulation of the Schottky barrier [18]. The usual method to characterize a PENG is via the open circuit voltage, V_{oc}, and/or the short circuit current density, J_{sc}, versus time as explained in section 1.5. This method gives information about the maximum reachable outputs and their behavior versus time. However, a PENG cannot harvest charges in an open or short circuit position and must be connected to a load. For this, an effective method is to measure the output voltage, V, through a resistive load, R_{load}, connected in parallel with the PENG to characterize both voltage and current, as described in Figure 4-10. In our case, the electrical equivalent model takes into account the influence of the whole stack materials in parallel and in series with the piezoelectric material (i.e. PEDOT:PSS deposited on ZnO in parallel with PMMA) (Figure 4-8b). The instantaneous power generated can be calculated with the equation,

$$P_{max} = \frac{V_{max}^2}{R_{load}}, \quad (5)$$

where P_{max} is the maximal power generated and V_{max} is the maximal peak voltage measured through the load resistance R_{load}. Usually, the piezoelectric material and the electrodes are deposited on planar surface with a specific active area (A). Then, it is more common to calculate an area power density, as $P_A = P/A$. The Table 4.1 summarizes the key performance

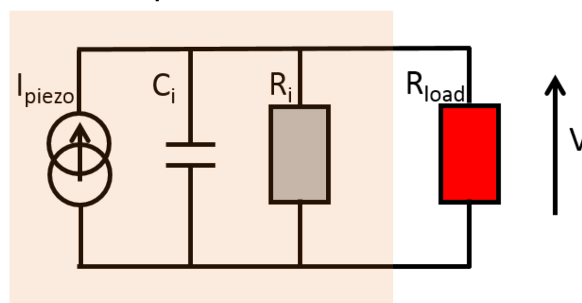

Figure 4-10: P-PENG equivalent model with a piezocurrent, static capacitance and a leakage resistance.

features as the energy generated per cycle and the average power density. Values of the capacitance C_i and the leakage resistance R_i are determined with the impedance meter. These results are compared with the same architecture developed by Briscoe *et al.* [63]. Even if our P-PENG generates a larger maximal output voltage, the maximal instantaneous power is smaller. The active area of patterned ZnO NWs (22.5 % of the total area) is smaller than usual PENGs and thus generates less piezocurrent. Energy and power outputs are, therefore, extrapolated to get a fairer comparison. This first P-PENG, without any process optimization of ZnO NWs, exhibits interesting performance compared to a PENG based on optimized ZnO NWs.

Table 4.1: Key parameters of P-PENG with a p-n junction architecture compared with the work of Briscoe et al. [63].

	ZnO/PEDOT:PSS	**Briscoe et al.**
V_{max} (mV)	200	76
Instantaneous area power density (µW cm^{-2}) (active area: 22.5%)	0.3	36
Expected instantaneous power density for 100% active area (µW cm^{-2})	1.33	
Average power density per cycle (µW cm^{-2})	0.0055	5.2
Expected average power density per cycle for 100% active area(µW cm^{-2})	0.024	
Energy output (nJ cm^{-2}) (active area: 22.5%)	0.475	38.6
Expected energy output (nJ cm^{-2})	2.11	
Leakage resistance R_i (MΩ)	1	0.001
Capacitance C_i (nF)	0.5	24
Effective transverse piezoelectric coefficient e_{31eff} (C m^{-2})	-0.45	

As a first approximation, this bending test with a controlled deflection can be used to determine the effective transverse piezoelectric coefficient $e_{31eff} = e_{31}\text{-}e_{33}(c_{13}^{E}/c_{33}^{E})$. A characterization method developed by Defay *et al.* [151] can easily determine this $e_{31\ eff}$, defined as:

$$e_{31eff} = \frac{\int_0^{+\infty} V(t)dt}{A\, R_{eff}\, b\, \delta(0)}, \tag{6}$$

with $V(t)$ output potential, A electrode area, R_{eff} equivalent resistance of R_i and R_{load} in parallel, b coefficient of geometric and mechanical properties of the substrate, $\delta(0)$ initial deflection of the free edge beam. This model is still valid when the piezotronic effect is neglected.

We obtain $e_{31\ eff}$ =-0.45 C m^{-2} for the device with the p-n junction. The effective transverse piezoelectric coefficient for these complex polycrystalline ZnO NWs is not far from ZnO thin films having $e_{31\ eff}$ = -1 C m^{-2} [154]. Unfortunately, the drawback of this method is its mechanical approximation, the lack of accuracy for the deflection, the vibrating beam length, the anchor position and the non-homogeneous stress along the bended device.

On top of this approximation, one of the main limitations of this method, when R_{load} is constant, is the variation of R_i. In our case, as shown in Figure 4-11, the current density-voltage characterization shows a diode behavior of the P-PENG with a hysteresis loop. The hysteresis loop features an abnormal variation of series resistance of our device with a significant shift of the threshold voltage. Nevertheless, R_i was assumed to be constant to extract $e_{31\ eff}$, adding an additional approximation in the characterization method of e_{31eff}. This variation of the internal resistance and its origin will be discussed in the next section (section 4.5.2).

However, the limitation of constant R_{load} is easily circumvented when the P-PENG is circuited with a variable load resistance. Such characterization with variable R_{load} have been specifically performed for devices using barrier blocking contacts.

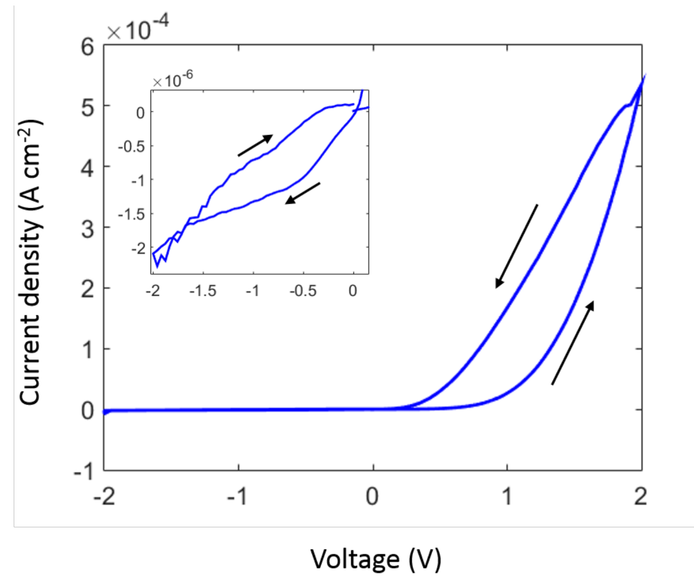

Figure 4-11: Current density-voltage characteristics of the p-n junction of the P-PENG with PEDOT:PSS. The arrows show the way of the characterization

The lower output performances of this first generation of P-PENG compared to the other PENG (Table 4.1) can also be linked with the features of spin-coated PEDOT:PSS. Indeed, the spin-coating process suffers from a relatively poor adhesion and the mechanical reliability of the interface PEDOT:PSS/ZnO. The AFM measurements of the surface topography evidence a rather high roughness of ZnO NWs (Figure 4-4e). This topography makes the top surface relatively hydrophobic leading to uncontrolled thickness of spin-coated PEDOT:PSS and a lack of adhesion between PEDOT:PSS and ZnO. Even the cavities on the top of ZnO NWs cannot be totally filled as shown in the Figure 4-12. That reduces the contact area and may impact the overall PENG performances introducing parasitic air gaps. Therefore, alternative deposition technology of conductive polymer shall be envisaged. Preliminary demonstration of the use of PRAP-CVD for the conformal deposition of PEDOT will be reported into the perspective section of this work. The other alternative that was completed is the use of an electrical architecture using a blocking barrier.

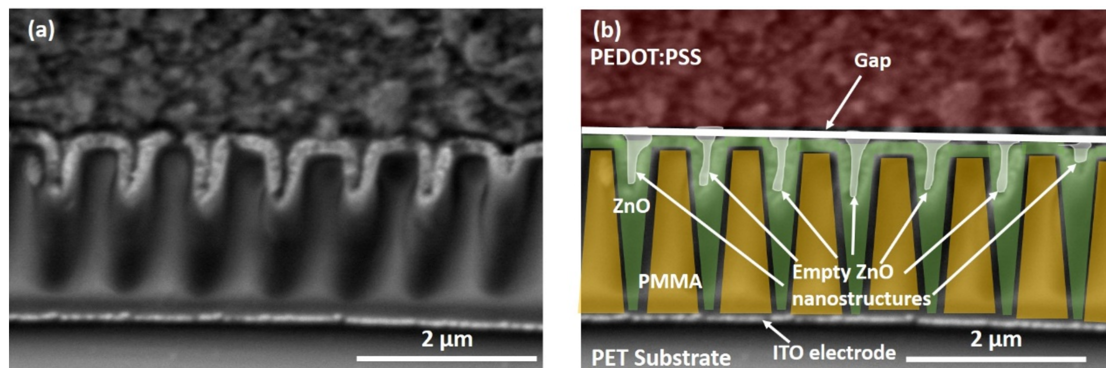

Figure 4-12: a) SEM cross section of a P-PENG with a p-n junction. Cross section realized by cryo-microtome shows the interface between PEDOT:PSS and ZnO nanostructures. b) Schematic representation of the different elements added on the SEM picture. From top to bottom: PEDOT:PSS in red, gap and cavities in ZnO in white, ZnO in green, PMMA in yellow, ITO and the PET substrate.

4.5.2. Blocking barrier P-PENG

The blocking barrier architecture relies on the integration of dielectric materials at the interface of the ZnO/Ti/Au Schottky contact. This leads to a ZnO/Al_2O_3/Ti/Au stack for which the electrical charges move to the electrode to screen the built-in electric field when stress or strain are applied. When the stress or strain is released, the piezopotential disappears and the external charge flows back, as explained in the section 1.5 [18]. The dielectric P-PENG is processed on PET with an ITO bottom electrode for an ohmic contact with ZnO. After the NIL step, two different N-doped ZnO devices are processed by ALD at 80°C with 720 cycles to fill the patterned PMMA holes with a conformal thin film of around 120 nm. One with a very low doping of nitrogen with a purge time of 3 s and the other one with a higher nitrogen doping tailored via a purge time of 20 s. Then, an insulator thin layer of 33 nm of Al_2O_3 is processed by ALD at 80°C as the blocking barrier. Alumina is preferred to a polymer as a dielectric layer for several reasons. First, the Al_2O_3 ALD provides a conformal deposition in cavities and a good adhesion compared to the spin coating process of a polymer. Second, the mechanical properties of alumina are closer to ZnO rather than a polymer which absorbs more strain of the strain applied on the device. Indeed, a study of Hinchet *et al.* shows by finite element modeling that the piezopotential generated by a constant applied force on top on the insulating layer deposited over ZnO NWs decreases by 10 % when PMMA is used instead of alumina [60]. Finally a top electrode of Ti/Au (5/50 nm) is evaporated. The two devices have a functional area of 7x7 mm². Figure 4-13a sketches a cross section of the devices, whereas Figure 4-13b is a top view of the device clamped in the setup used for the basic electrical characterization as we previously explained.

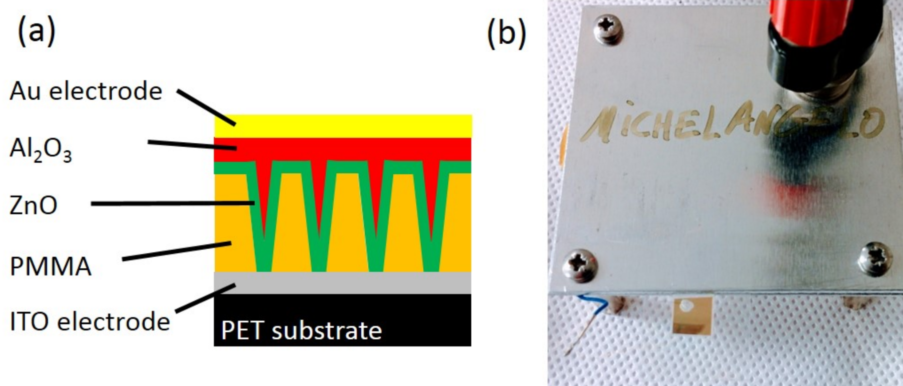

Figure 4-13: a) Schematic cross section of the architecture of the P-PENG. b) Experimental setup with the clamped P-PENG for the bending characterization.

Current-voltage characterizations of both devices (low N-doped ZnO and high N-doped ZnO) show also hysteresis behaviors of a Schottky diode response. The device with a low N-doped ZnO shows a slightly rectified diode behavior (Figure 4-14a) compared to the higher N-doped ZnO that shows a clear diode behavior (Figure 4-14b). The diode behavior results from a Schottky barrier between ZnO and Au [43]. The alumina at the interface ZnO/Au acts as a buffer layer, reducing the conductivity without interfering with the interface behavior [155]. At 2 V, the device with the lower N-doped ZnO (Figure 4-14a) shows a current density approximately 500 times larger than the device with a higher N-doped ZnO, confirming the much lower resistance of the lower N-doped ZnO thin films described in the previous chapter.

The observed hysteresis was also reported for the devices relying on p-n junction engineering. We have identified that this hysteresis is the consequence of charges accumulation or restitution in the P-PENG. This hysteresis appears with a combination of several effects: the resistive and capacitive behavior of the ZnO NWs, the barrier height of the contact (p-n or blocking barrier) and the parasitic capacitances. The devices are still considered as non-ideal Schottky diodes. The current-voltage curves are modeled, following the thermionic emission effect. The current can be expressed as [155]:

$$I = I_0 \exp\left(\frac{qV}{nk_BT}\right)\left[1 - exp\left(\frac{-qV}{k_BT}\right)\right], \tag{7}$$

and

$$I_0 = AA^{*}T^2 \exp\left(-\frac{q\varphi_b}{k_BT}\right), \tag{8}$$

where I_0 the saturation current, φ_b the effective barrier height, A^* the Richardson constant, q the electron charge, V the applied voltage, A the electrode surface area, k_B the Boltzmann constant, T the temperature in Kelvin and n the ideality factor. The values of R_s and φ_b are extracted using a method developed by Cheung *et al.* [155] and are reported in the Table 4.2 for the different P-PENGs.

Table 4.2: Electrical parameters obtained from I-V measurement of p-n junction and blocking/Schottky barrier.

	R_s (kΩ)	φ_b (eV)
p-n junction	3.64	0.142
Lower N-doped $ZnO/Al_2O_3/Au$	3.03	0.096
Higher N-doped $ZnO/Al_2O_3/Au$	60.7	0.135

The R_s of P-PENGs increases by 20 for the higher N-doped ZnO, further confirming the main impact of ZnO materials in this device architecture since the intrinsic resistivity of higher N-doped ZnO is 4 decades higher than the low N-doped doped ZnO. Furthermore, the significant increase of the barrier height for devices using lower and higher N-doped ZnO NWs confirms the change of the I-V curves moving from a slight current rectification response to a clear diode behavior. A low R_s and φ_b well correlate with a low hysteresis, as show the Figure 4-14a for the low N-doped ZnO. A higher height barrier leads to higher charge accumulation at the interface for the p-n junction and for the higher N-doped ZnO with a blocking barrier.

These devices can be turned to strain sensor applications with a modulation of current density while bending or compressing the ZnO NWs [43]. To demonstrate the strain sensor application, the device is clamped as a cantilever (Figure 4-13b) and bended up or down, compressing or stretching the ZnO:PMMA matrix, respectively. During the compression and tension state, current-voltage measurements are performed and compared with the free-standing cantilever, considered as the neutral reference. Figure 4-14c and d shows a slight increase of the current density when the ZnO:PMMA is under compressive stress (i.e. bend up) for both lower and higher N-doped ZnO, respectively. When the device is under tensile stress (i.e. bending down), the opposite effect is observed and the current density decreases for both devices. Two mechanisms may explain this modulation of current density in the case of polycrystalline ZnO NWs: the piezotronic effect and the piezoresistive effect. The piezotronic effect relies on a modulation of the barrier height [43], [156] as explained in the section 1.4.1. The piezoresistive effect is based on the shift of the resistivity of the material

[135]. The R_s and φ_b are extracted from the I-V curves under bending (up and down) and no significant variation of φ_b is found. Therefore, the current modulation is mainly driven by the piezoresistive effect, excluding any significant piezotronic effect in our devices using polycrystalline ZnO NWs.

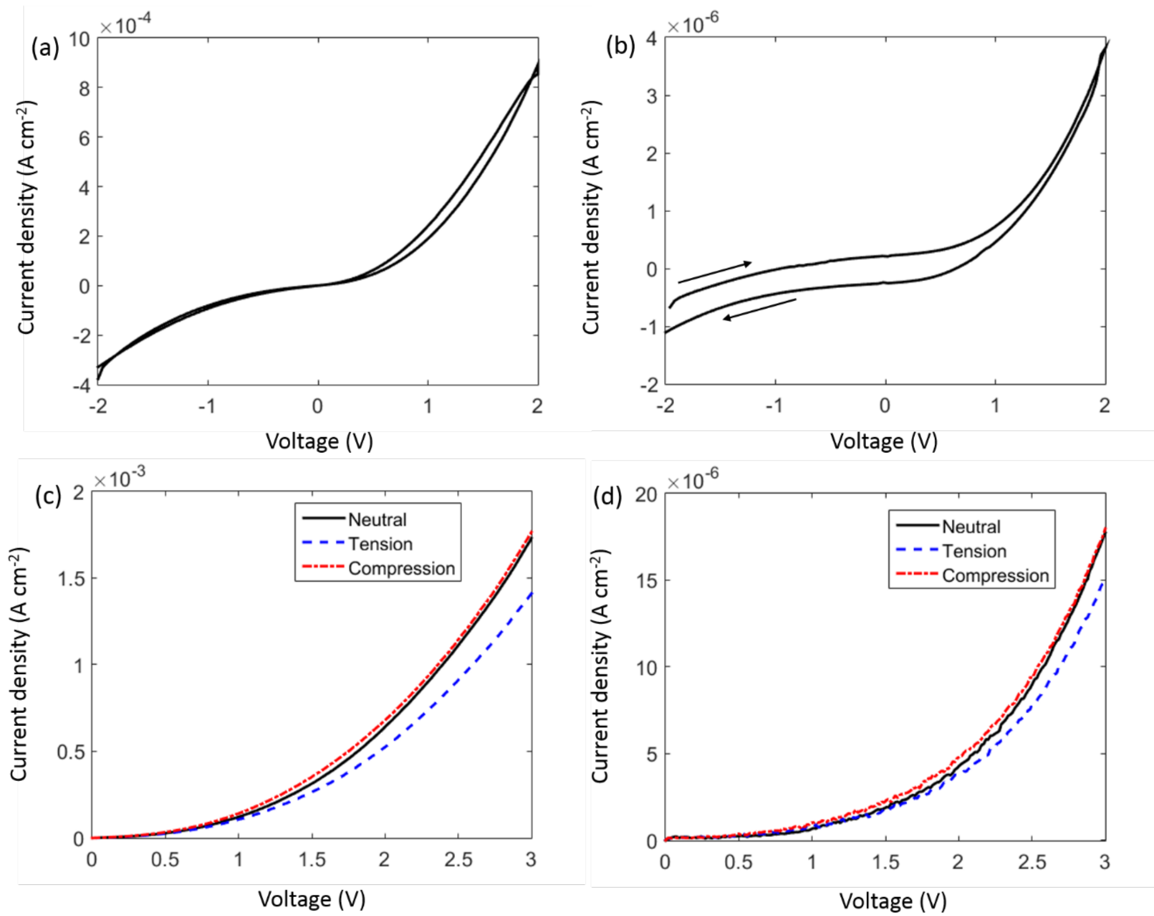

Figure 4-14: a) & b) Current density-Voltage characterization of devices from -2 to 2 V to -2V for the a) lower N-doped ZnO P-PENG and b) higher N-doped ZnO P-PENG. The arrows shows the way and way back. c) & d) Current density –Voltage characterization from 0 to 3 V under tension, compression and neutral for the c) lower N-doped ZnO P-PENG and d) higher N-doped ZnO P-PENG

Figure 4-15 shows the voltage output variation related to the damping factor of devices at their optimum load resistance. The charges generated from the piezocurrent I_{piezo} are discharged in their optimum load resistance, defined as the resistance where the power output is maximum [63] (in more details in the next section 4.6**)**. Table 4.3 compares the main features of both devices. V_{max} is defined as the maximum voltage output at the optimum load. The power generated at this V_{max} per area defines the instantaneous area-power-density. The

average power and the energy are calculated for one pulse of a few milliseconds. The device with a higher N-doped ZnO generates more than twice the amount of energy compared to the lower N-doped ZnO. The static capacitance C_i of both P-PENGs are quite similar compared to the leakage resistance R_i and the dielectric losses (D or tan δ) that are more than one order of magnitude different between the lower and the higher N-doped ZnO P-PENG. The change in the semi-conductor properties of ZnO NWs mainly explains the variation of dielectric losses. Indeed, more resistive are materials, lower are dielectric losses. It results for the higher N-doped ZnO an enhancement of accumulated charges at the interfaces instead of recombining through the material.

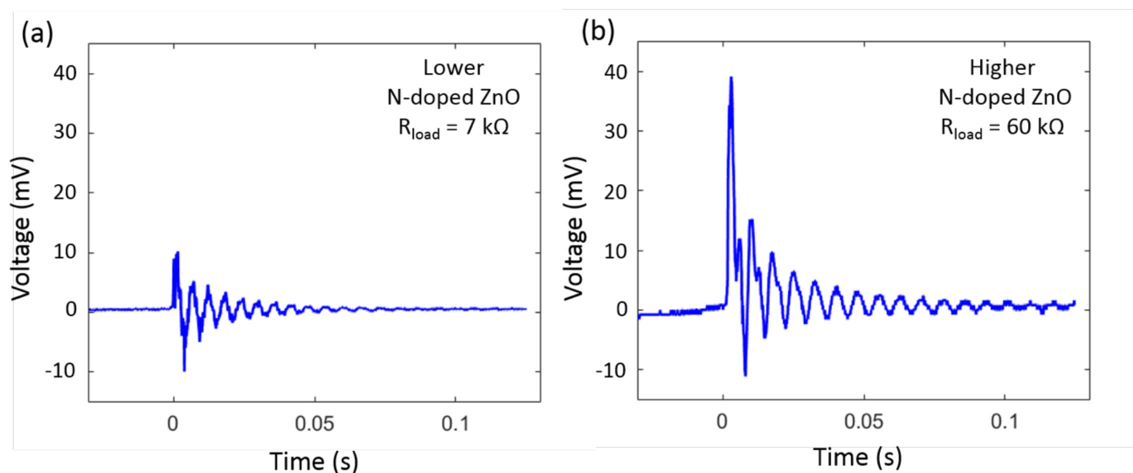

Figure 4-15: Voltage output of the oscillating devices after bending and release of the strain for the a) lower N-doped ZnO P-PENG at optimal load and b) higher N-doped ZnO P-PENG at optimal load.

These P-PENGs with N-doped ZnO can be compared qualitatively to other PENGs using doped ZnO. Other doping element as Li, P, As, Ag have been used in the literature to optimize the performance of the PENG by decreasing the charge carrier density, but often require much higher temperature process [55]–[57], [157]. Unfortunately, these works do not characterize the transport properties of their ZnO NWs to confirm a decrease of the charge carrier density. A work of Zhang *et al.* shows an enhancement of the output performance of the piezoelectric nanogenerator based on halides element and more particularly on Br-doped ZnO [58]. They show an increase of the output voltage correlated with a lattice expansion of the unit cell of 0.45 %. Interestingly, in our work, an opposite behavior is observed. The increase of the output voltage is measured when the lattice parameter is shrunk by 0.3 %, showing also that the performance of PENGs can still be enhanced when the crystalline lattice is contracted. Indeed,

the change in the electric conductivity of nitrogen-doped ZnO pillars predominantly impacts on the output performances of P-PENGs.

Table 4.3: Key characteristics for the low and high N-doped ZnO flexible energy harvesting devices.

	Low N-doped ZnO (purge 3s)	Higher N-doped ZnO (purge 20s)
V_{Max} (mV)	10.2	39.2
Optimum R_{load} (kΩ)	7	60
Instantaneous area power density (nW cm^{-2}) (active area: 22.5%)	36.5	65.6
Expected instantaneous power density for 100% active area (nW cm^{-2})	162.2	291.5
Average power density per cycle (nW cm^{-2})	0.25	0.80
Expected average power density per cycle for 100% active area (nW cm^{-2})	1.11	3.55
Energy of one pulse (pJ cm^{-2}) (active area: 22.5%)	75.3	176
Expected energy output (pJ cm^{-2}) (active area: 100%)	334.6	782.2
Leakage resistance R_i (kΩ)	17	200
Capacitance C_i (nF) (at 7 Hz)	49	56
D (or tan δ) (at 7 Hz)	>10	0.91

The P-PENGs performances of p-n junction and blocking barrier architecture using polycrystalline ZnO NWs and up-scalable processing technologies are competitive when compared to published PENG results. However, the analysis of the output voltage curves of the different P-PENGs features the oscillation and the mechanical damping factor of the used substrate. The oscillations represent the cantilever vibration of the P-PENG at its specific frequency. The specific vibration frequencies of the P-PENGs with the p-n junction and the blocking barrier are around 550 and 150 Hz, respectively. The specific vibration frequency features the time derivative of the deflection. This latter is a critical parameter, which is systematically neglected in literature, to perform an accurate and rigorous comparison of

energy harvesters. As an experimental illustration of such a statement, Figure 4-16 shows the linear increase of the output voltage of one of our PENGs as a function of the amplitude of a speaker triggering the deformation of our PENG while the deformation of the PENG membrane is measured almost constant as a function of the amplitude of the speaker. These experimental results use a specific characterization bench which is detailed hereafter but further prove the strong importance of the time derivative of the deflection. Indeed, changing the amplitude of the triggered signal fixed at 10 Hz (speaker) is mainly transduced into the P-PENG membrane by modifying the time derivative of the deflection and not the amplitude of the deformation. This simple but realistic experiment provides evidence that, beyond the amplitude of the PENG deformation, also the speed at which the PENG is deformed is a critical feature of nanogenerators. To the best of our knowledge, such a parameter has never been taken into account for a fine and rigorous benchmark of the performance of PENGs.

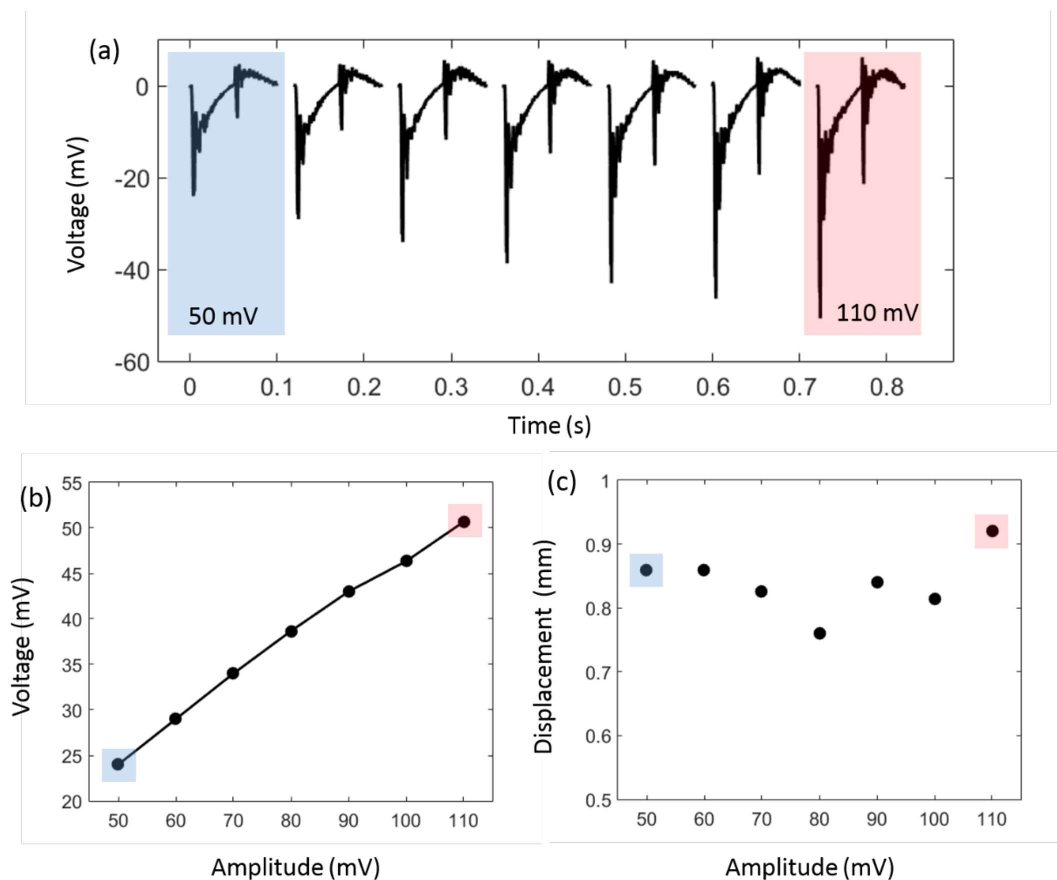

Figure 4-16: Characterization of the P-PENG for different amplitudes of the speaker. The blue and the red square represent the output values of voltage and displacement for an amplitude of 50 mV and 110 mV of the speaker, respectively. a) Output voltage of one cycle for an actuation from 50 to 110 mV of the speaker at 10Hz. b) Maximal absolute value of the output voltage for the increasing amplitude of the speaker from (a). c) Displacement maximal peak-to-peak of the P-PENG measured by the vibrometer.

Therefore, we specifically develop a new and original method for characterizing unambiguously PENG devices. Nevertheless, this method requires large area PENGs that have been purposely fabricated.

4.6. Setup for accurate characterization with speaker and vibrometer

We focus on the direct piezoelectric effect of ZnO NWs integrated in a large scale and flexible devices using blocking barrier contact. For this, the rate of the stress or strain applied on the device should be quantified and set as equivalent for making a reliable comparison of the performance of PENGs. Previous studies demonstrate theoretically the importance of the rate of stress [8], [63] but most of characterizations of PENGs reported in literature do not mention or take into account the rate of stress/strain for evaluating reliably the PENGs performance [34], [35], [47], [58], [65], [158]. The importance of the stress rate can be apprehended for a bending test when remembering the constitutive equation of piezoelectricity [25]:

$$\boldsymbol{T} = \boldsymbol{c}^{E}\boldsymbol{S} - \boldsymbol{e}^{t}\boldsymbol{E}, \tag{9}$$

$$\boldsymbol{D} = \boldsymbol{e}\boldsymbol{S} + \boldsymbol{\varepsilon}^{S}\boldsymbol{E}, \tag{10}$$

$$\boldsymbol{D} = \boldsymbol{d}\boldsymbol{T} + \boldsymbol{\varepsilon}^{T}\boldsymbol{E}, \tag{11}$$

with ***T*** stress, ***S*** strain, ***E*** electrical field, ***D*** electric displacement field, $\boldsymbol{c}^{E}$ elastic matrix at fixed E, ***e*** and ***d*** piezoelectric coefficient matrices, $\boldsymbol{e}^{t}$ transposed piezoelectric matrix, $\boldsymbol{\varepsilon}^{S}$ and $\boldsymbol{\varepsilon}^{T}$ dielectric permittivity matrix under constant strain and stress, respectively. The displacement current ***J*** is linked to ***E*** and ***D*** through one part of the Maxwell's equation,

$$\boldsymbol{J} = \frac{\partial \boldsymbol{D}}{\partial t} = \varepsilon_0 \frac{\partial \boldsymbol{E}}{\partial t} + \frac{\partial \boldsymbol{P}}{\partial t}, \tag{12}$$

with ***P*** polarization field, ε_0 permittivity in vacuum. For an anisotropic piezoelectric material under a small uniform mechanical strain, ***P*** is defined as

$$\boldsymbol{P} = \boldsymbol{e}\,\boldsymbol{S} + (\boldsymbol{\varepsilon^S} - \varepsilon_0)\boldsymbol{E}. \tag{13}$$

If the device is short-circuited to measure the current density (***E** = 0*), the time derivative of eq. (10) and (11) become respectively,

$$\boldsymbol{J} = \frac{\partial \boldsymbol{D}}{\partial t} = \boldsymbol{e}\,\frac{\partial \boldsymbol{S}}{\partial t}, \tag{14}$$

$$\boldsymbol{J} = \frac{\partial \boldsymbol{D}}{\partial t} = \boldsymbol{d}\,\frac{\partial \boldsymbol{T}}{\partial t}, \tag{15}$$

and (13) inserted in (12) give (14) with the same consideration. From this equation, it can be seen that the current-density is proportional to the rate of stress or strain applied on the piezoelectric material. A fast deformation can generate a high instantaneous current density and a high instantaneous power output, but it does not imply that this high-power output can be sustained over a long time. A high instantaneous power output is therefore not representative of the energy harvested. The energy harvested is the average power output during a specific time.

A PENG converts mechanical to electrical energy in a relation defined as the electromechanical coupling, k:

$$\boldsymbol{k}^2 = \frac{Electrical\ energy\ performend\ by\ PENG}{Mechanical\ energy\ supplied\ to\ PENG}, \tag{16}$$

where the conversion from mechanical to electrical energy is the piezoelectric coefficient and the input mechanical energy is relative to the applied strain or stress [63], [75]. Nevertheless, ***k*** and the maximum mechanical yield are limited by the yield stress of the piezoelectric material. From our perspective, the most relevant performance characterization is to average over the time the performance features to take into account the effect of time dependence like the average power or the energy generated by a pulse.

Various methods are used to characterize PENGs processed on a soft polymer substrate as developed in section 1.5: a *stress-driven* conversion or a *strain-driven* conversion. In literature, most of the reported setups strain the device without controlling their rate [34], [35], [47], [58], [65], [158]. Here, we set-up an original method that controls the strain rate in order to quantify and compare P-PENGs. For this purpose, a defined deflection of a membrane

vibrating at a specific frequency controls accurately the strain and its rate. Therefore, we fabricated a flexible P-PENG membrane relying on the same device architecture as investigated previously, with a blocking barrier except a top electrode of Pt instead of Au. The P-PENG is composed (from bottom to top) of PET/ITO/ZnO:PMMA/Al_2O_3/Pt. The P-PENG has a surface area of 5 cm diameter as shown in Figure 4-17a, leading to 3.7 billion ZnO nanopillars. The flexible substrate is clamped with a 7.8 cm diameter annular anchor above a speaker as described by the Figure 4-17b. A function generator inputs the waveform, frequency and amplitude to the speaker that transduces the acoustic wave to the membrane (as described in the experiment part). The clamped membrane vibrates at the fundamental mode (0,1) where there is no nodal diameter and one circular node (i.e. the clamped edge). A vibrometer with a white light measures the deflection at the center of the membrane where it is maximal. A maximal deflection of the membrane at 10 Hz is 0.45 mm. A rate of strain of 140 mm.s^{-1} is controlled with an acoustic pulse. The membrane vibrates with a damping factor at its fundamental frequency at 200 Hz.

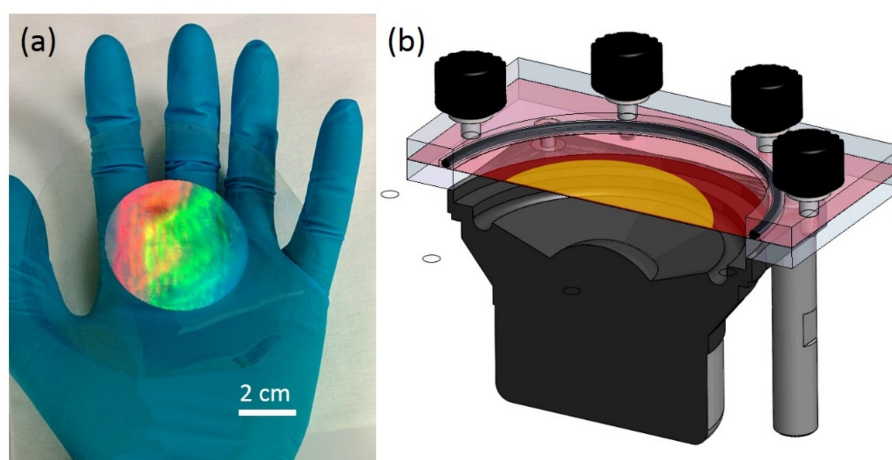

Figure 4-17. a) Photograph of a 5 cm diameter device with 3.7 billion ZnO nanostructures on a flexible substrate. The colored disk is due to light diffraction. b) Schematic cross section of the clamped device, actuated as a vibrating membrane by a speaker with a 7.8 cm diameter annular anchor. The orange area represents the active area of ZnO nanostructures.

The device is laying on the speaker as a free-standing membrane without being clamped. Then, the speaker sweeps in frequency from 15 to 50 000 Hz. The amplitude of deflection of the P-PENG membrane varies with the frequency and is maximal at the resonance frequency. The resonance frequency is determined by measuring the piezoelectric response of the membrane, proportional to the strain of the device (eq.(14)). The maximal output voltage is

measured and reported for each frequency in Figure 4-18. The output voltage is maximal around 200 Hz, determining the fundamental frequency of the membrane.

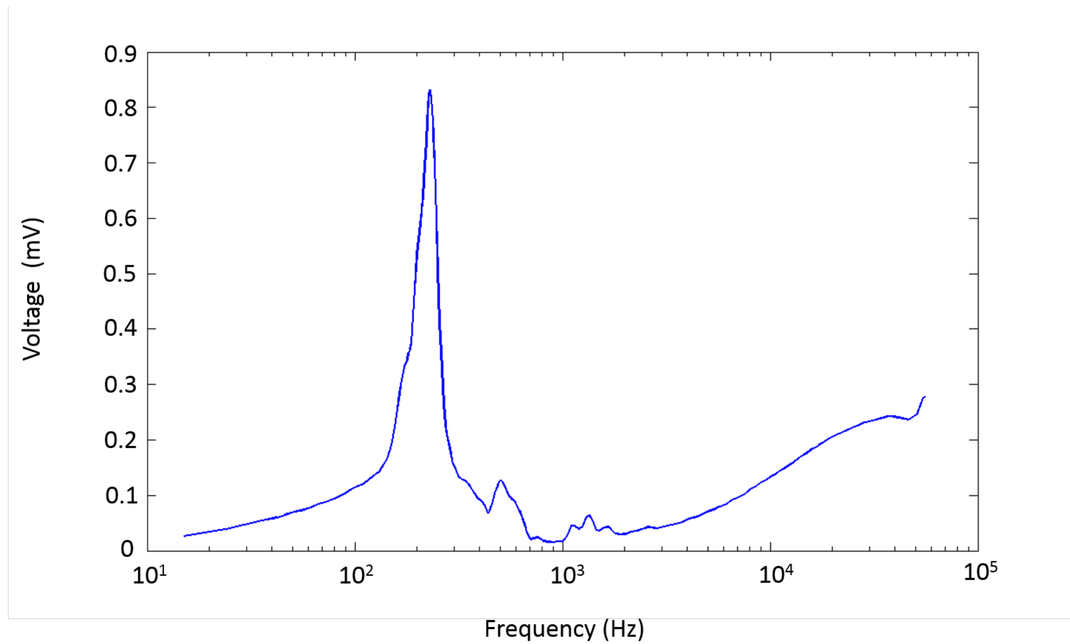

Figure 4-18: Variation of the maximum output voltage of the vibrating P-PENG for different frequencies.

Then, an effective method is to measure the output voltage, *V*, through a variable resistive load, R_{load}, connected in parallel with the P-PENG to characterize both voltage and current, as described in Figure 4-19. An operational amplifier is connected in parallel with the P-PENG and the R_{load}, which allows to measure the output voltage with an oscilloscope without affecting the measure.

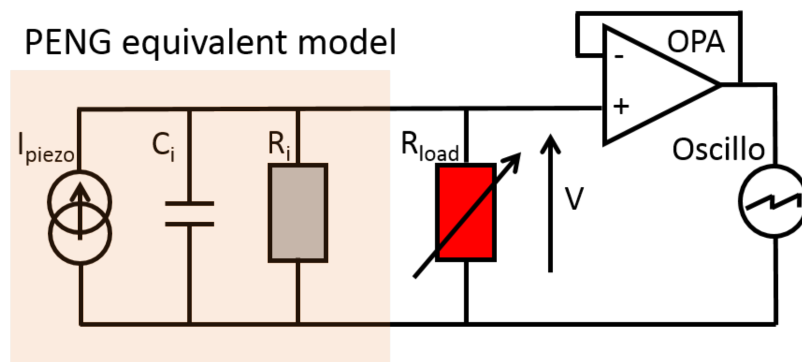

Figure 4-19. P-PENG equivalent model with the electrical setup for accurate characterization.

The resistive load varies between 30 Ω and 10 MΩ. The instantaneous power generated can be calculated with the eq. (5) ($P = \frac{V^2}{R}$,). We performed the complete electrical characterization on two PENGs, one with lower N-doped ZnO and a second with a higher N-doped ZnO. The value of P_A as a function of R_{load} is reported in Figure 4-20a. The evolution of the P_A and the output voltage of the higher N-doped P-PENG are shown in Figure 4-20b. The time variation of the output voltage at the optimal load resistance for the higher N-doped device is reported in Figure 4-20d. The acoustic strain has a 10 Hz frequency with a release of the pressure at half period, showing a lower voltage pulse. The output voltage frequency is around 200 Hz linked to the fundamental vibration frequency of the membrane. The open circuit voltage V_{oc} versus time for the low- and the high-N-doped devices are shown in Figure 4-20c and Figure 4-20e, respectively. The V_{oc} of P-PENGs using higher N-doped ZnO NWs is 3.5 larger than the one using lower N-doped ZnO NWs. The maximum instantaneous area power density for the device with a higher N doped ZnO is 1.14 nW cm^{-2} for its optimal R_{load} of 6 kΩ. The P_A of this higher N-doped device is more than 2.5 larger than the P_A of the lower N-doped device, with 0.45 nW cm^{-2} at R_{load} of 4 kΩ. The fatigue tests of devices are performed at 5 Hz during 5000 s (25 000 cycles), see Figure 4-20e. The voltage output remains constant with the same time variation behavior. The slight variation of the absolute maximum output voltage is caused by the sampling of the signal processing during the long-time characterization. It is worth noticing that the reported output values are one decade lower compared to the ones reported in the literature because of the very low deformation and very low mechanical stress applied in our experimental setup. However, our two devices are compared at the same deformation amplitude and the same rate of stress.

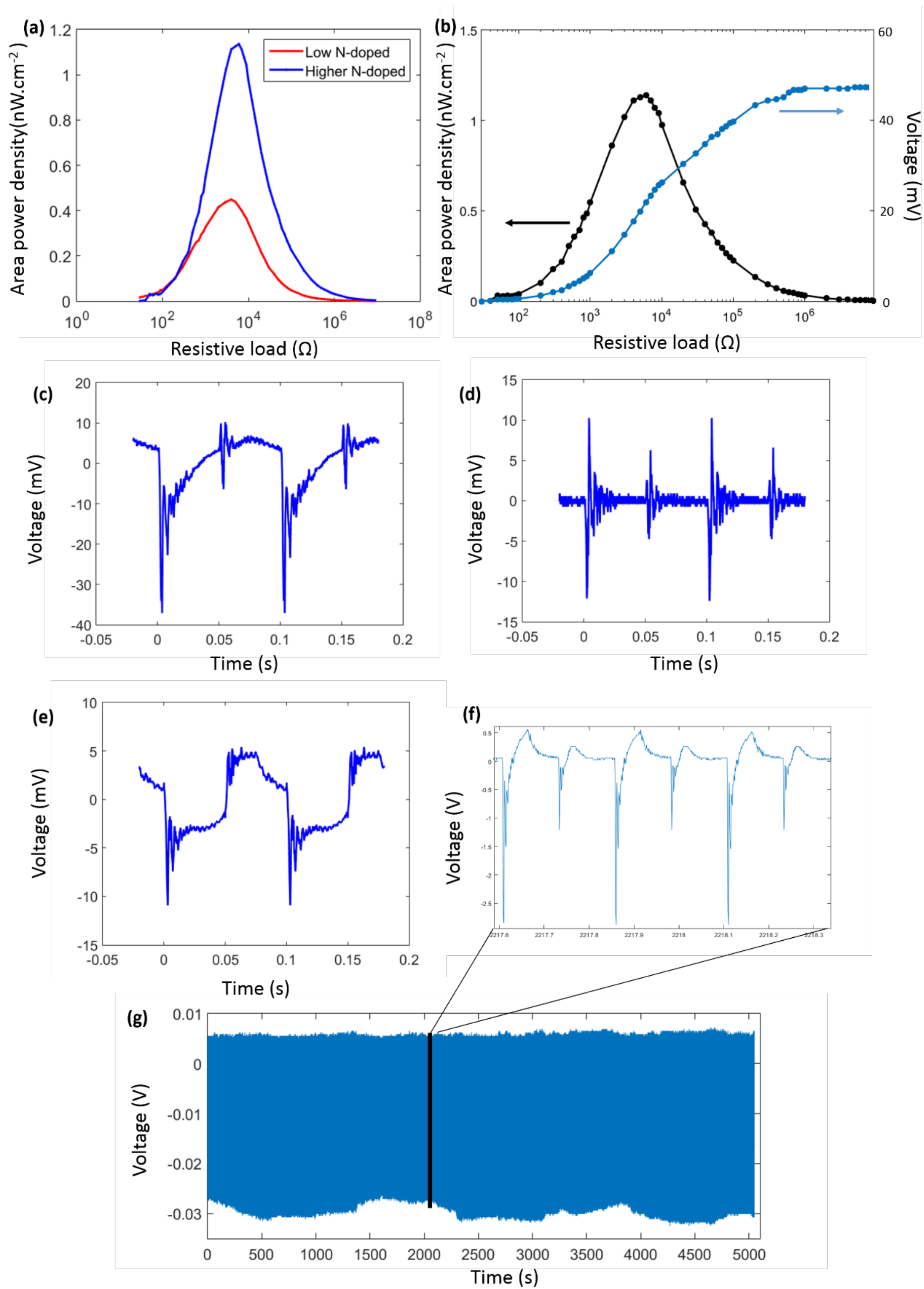

Figure 4-20. a) Dependence of the output area power density on the load resistance for a higher and a lower N-doped ZnO P-PENG. b) Dependence of the output voltage and area power density on the load resistance for the higher N-doped ZnO P-PENG. c) Time variation of the output voltage of the higher N-doped ZnO P-PENG in open circuit. d) Time variation of the output voltage of the higher N-doped ZnO P-PENG at its optimum load of 6kΩ. e) Time variation of the output voltage of the lower N-doped ZnO P-PENG in open circuit. f-g) Time variation of the output voltage in open circuit for fatigue testing at 5 Hz for 5000 seconds, f) Zoom of (g).

Our tested devices can be quantitatively compared with their similar geometry and mechanical properties. The C_i and R_i values are used to determine I_{piezo}. Those values are calculated with an impedance analyzer at the fundamental frequency vibration for both devices and reported in Table 4.4. In order to maximize the power output harvested, R_{load} shall match the internal impedance of the PENG [159], $Z = (\omega C_i)^{-1}$. C_i are different for different doping levels of nitrogen, which explains a lower optimal matching impedance Z for the lower N-doped ZnO compared to the higher N-doped ZnO. The experimental matching impedance (optimum R_{load}) is in the same order of magnitude that the internal impedance, Z while being significantly lower than the internal resistance R_i. The ratio Ri/R_{load} typically features the capabilities of the piezocurrent to flow outside the device when the internal impedance is almost matched by R_{load}. This is one of the mandatory electrical engineering of the external circuitry to enhance the optimal power output. For our both devices, the amount of I_{piezo} for optimum R_{load} is 76 % and 91 % for the device with the lower and the higher N-doped ZnO, respectively. This is a clear and reliable demonstration that the device using ZnO with a higher N-doping, harvests significantly more current and is much less leaky than the device using lower N-doped ZnO. This confirms that ZnO thin films processed by atomic layer deposition and slightly doped with nitrogen are prone to improve the output-performance of PENGs, even deposited in a high aspect ratio pattern to form complex NWs.

Table 4.4.Comparative output values and key parameters of low and higher N-doped ZnO P-PENGs

	Low N-doped ZnO (purge 3s)	Higher N-doped ZnO (purge 20s)
V_{oc} (mV)	10.5	36.7
Optimum R_{load} (kΩ)	4	6
Voltage on optimum R_{load} (mV)	6.53	12.4
Current density on optimum R_{load} (nA cm^{-2})	75.6	98.2
Instantaneous area power density P_A (nW cm^{-2}) (active area: 22.5%)	0.45	1.14
Expected instantaneous power density for 100% active area (nW cm^{-2})	2	5.06
Average power density per cycle (nW cm^{-2})	0.00145	0.0241
Expected average power density per cycle for 100% active area(nW cm^{-2})	0.0064	0.107
Energy of one pulse (pJ cm^{-2}) (active area: 22.5%)	0.294	2.51
Expected energy output (pJ cm^{-2}) (active area: 100%)	1.3	11.15
R_i (kΩ) (at 200 Hz)	12.6	65.4
C_i (nF) (at 200 Hz)	217	75.8
Internal impedance Z (kΩ)	3.66	10.5

In our method, the extraction of the value of the electromechanical coupling parameter k is unreliable because of the inhomogeneous stress distribution along the membrane under oscillation. However, considering an identical rate of strain and the eq. (14), the ratio of the current density of the devices becomes:

$$\frac{J_h}{J_l} = \frac{\boldsymbol{e}_h}{\boldsymbol{e}_l}, \tag{17}$$

with J_h and J_l the current density of the higher N-doped and lower N-doped ZnO devices, respectively, and $\mathbf{e}_h$ and $\mathbf{e}_l$ the effective piezoelectric coefficient of the higher N-doped and lower N-doped ZnO devices, respectively. Therefore, Equation (17) shows that the ratio of

current density is equivalent to the ratio of the effective piezoelectric coefficient of the measured devices. In our case and for the same R_{load}, the ratio between $\mathbf{e_h}$ and $\mathbf{e_l}$ shows an increase of 60 % of the piezoelectric coefficient when ZnO is doped with a higher amount of nitrogen.

A performance comparison of this P-PENG with other PENGs may be possible reminding several considerations. One of the most reliable ways to compare devices is to compare time invariant variables as a mean average power or energy generated as the previous consideration have demonstrated the time influence [63]. For this, a study of Crossley *et al.* compared different PENGs using an energy conversion efficiency, $\boldsymbol{\chi}$, that can be expressed as [75]:

$$\chi = \frac{Electrical\ work\ performed\ by\ PENG}{Net\ energy\ supplied\ to\ PENG}. \tag{18}$$

This efficiency looks like the electromechanical coupling factor $\boldsymbol{k^2}$, but is different because $\boldsymbol{k^2}$ is usually considered lossless. The net energy supplied to the PENG is the acoustic pressure in our work. The accurate characterization setup determines easily and accurately a good approximate value for the stress and strain applied on the P-PENG.

Considering the P-PENG as a circular thin membrane under pressure with a homogeneous deformation, the radial strain can be expressed as [160]:

$$\varepsilon_r \approx \frac{2}{3}\frac{W_0^2}{R_M^2}, \tag{19}$$

ε_r radial deformation, W_0 maximal deflection, R_M radius of the membrane. In our present case, the maximal radial deformation calculated for a measured deflection of 0.4 mm is 2.8 x10^{-2} %. The COMSOL simulation with a 1 MPa stress determines a strain of 1.55 x10^{-2} % on the truncated conic shape with the donut topography. These values are close and in a good agreement, related to their respective applied stress. Analytically, the stress is calculated with:

$$\sigma_M = \sigma_0 + \frac{2}{3}\frac{W_0^2}{R_M^2}\frac{E_M}{1-\nu_M^2}, \tag{20}$$

σ_0 initial stress (null), E_M Young's modulus, v_M Poisson's ratio. The piezoelectric active layer is 2 µm thick and the PET substrate is 125 µm thick. As the thickness of ZnO NWs is very thin compared to the substrate, the stress can be associated to the PET substrate only, giving $\sigma_M = 1.25\ MPa$.

Going back to the energy conversion efficiency, **χ**, the mechanical energy supplied to the P-PENG is considered as:

$$W = \frac{1}{2}\, s_E T^2, \tag{21}$$

with s_E the elastic compliance at constant electric field (25 TPa^{-1} for ZnO [2015 Crossley]), T the applied stress. Using $s_E = 25\ TPa^{-1}$ for ZnO [75], the energy input to the P-PENG is $62.5\ mJ\ m^{-3}$.

Usually, the electrical work performed by the PENG is calculated from V_{OC} and J_{SC} with the electrostatic energy density, expressed as [71], [75]:

$$W_E = \frac{1}{2}\, E_{OC} D_{SC}, \tag{22}$$

with E_{OC} the electric field in open circuit, D_{SC}, the charge density. In our case, the characterization at optimal load harvests the electrical energy and does not require the characterization at open and short circuit. Using the energy harvested by one pulse for the P-PENG with a high N-doped ZnO, the energy conversion efficiency is **χ = 10 %**. Crossley *et al.,* determined some PENG energy conversion efficiency. Those based on ZnO are efficient ≈ 5 %, others based on PVDF and PVDF-TrFE ≈ 12%, PZT 18 %, PMN-PT 16 % [75]. With 10 % P-PENG based on high N-doped ZnO has an energy conversion efficiency in the higher range of those reported in the literature [19].

4.7. P-PENG perspectives for optimization

The integration of PEDOT by PRAP-CVP on large P-PENG solves the technical problem of a lack of conformity and adhesion of the spin coated PEDOT:PSS. This device is fabricated with the low N-doped ZnO and the stack from the substrate to the top electrode is: PET/ITO/ZnO:PMMA/PEDOT/Au. Extrapolated from the small P-PENG results, the performance of this large P-PENG should be larger than the one with the blocking barrier.

Unfortunately, the maximum power output is 7 times smaller than the device with the blocking barrier. Too high losses are the consequences of this low power output. The variation of the power output with the resistive load exhibits 2 peaks instead of one (Figure 4-21). The impedance characterization shows an internal resistance and a capacitance of R_i = 93 Ω, C_i = 196 nF. R_i is more than 100 times smaller than blocking barrier reported in Table 4.4. The value of R_i corresponds to the first optimum of the power output represented with the dashed red line in Figure 4-21. The second main optimum around 1 kΩ is close to the internal matching impedance *Z*. This analysis shows that when R_{load} is matching R_i only 50 % of the charges are harvested, others are recombining due to the low intrinsic resistivity of ZnO with low nitrogen doping. By extrapolation, a power output would be twice bigger for the P-PENG with PEDOT than the P-PENG with alumina if all the charges were harvested (i.e. lossless). That confirms the interest of a p-n junction to harvest larger amount of energy if PEDOT is combined with a higher N-doped ZnO.

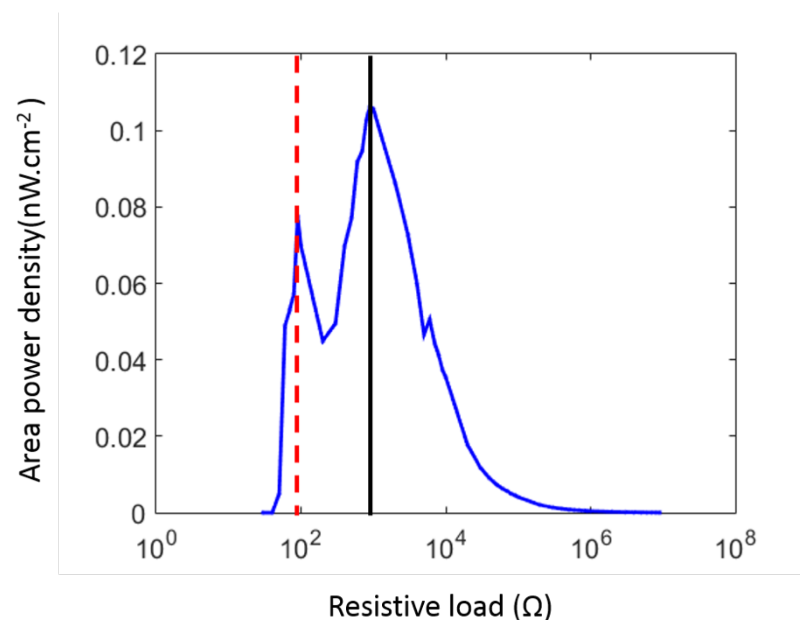

Figure 4-21: Variation of area power density of P-PENG with PEDOT with a variable load. The dashed red line is the value of the internal resistance Ri, and the black line is the R_{load} matching the optimal impedance Z.

4.8. Conclusion

In this work, a new kind of piezoelectric nanogenerator based on N-doped ZnO combining large scale technology, NIL and ALD, is fabricated and tuned with nitrogen doping to increase the piezoelectric response. Taking advantage of using a top-down approach, the electromechanical performances are optimized by a finite element modeling to control the aspect ratio and the pitch of ZnO NWs. The local structural analysis of this low temperature process shows highly polycrystalline ZnO nanopillars exhibiting piezoelectricity responses. The derivation of the constitutive piezoelectric equations demonstrates the importance of an accurate actuation setup. An equivalent model for the P-PENG combined with an accurate electromechanical setup allows to reliably compare two devices: one with a low N-doped ZnO and the other one with a higher N-doped ZnO. The original electromechanical setup underlines the effect of the rate of deflection. This characterization bench accurately controls and measures simultaneously the deformation, the time derivative of deformation, the frequency and the power output of large P-PENGs. P-PENGs are quantitatively compared. The P-PENG with higher N-doped ZnO shows larger output voltage and instantaneous power than the lower N-doped ZnO. The power output is increased by 150 % when nitrogen doping of ZnO nanopillars is tailored towards higher concentration and relies partly on the optimization of the internal resistance of the devices. Concomitantly to this feature, we show that higher nitrogen doping of our ZnO-based P-PENGs increases also the effective piezoelectric coefficient by about 60 %. An energy conversion efficiency of 10 % is deduced for the P-PENG with higher N-doped ZnO, higher than others reported ZnO based PENGs.

Conclusion and perspectives

The present work stands in the context of the rapid growth of portable electronics and wireless sensors. This growth drives the request for advances in materials science and technology to harvest energy from ambient sources. Piezoelectric nanogenerators, which convert vibrations into electrical energy, are considered as one of the promising building blocks for the design of low-cost and performant energy harvesting devices. Several demonstrations of PENGs have been reported throughout the last decade, many of them based on Zinc Oxide –ZnO– nanowires. Despite interesting performances, literature also suggests that the classical bottom-up approach of optimized ZnO-based PENGs performance approaches its limits and that top-down approaches merit further attention.

This has motivated the present work, with the aim to conceptualize by models, to fabricate and to investigate a new type of piezoelectric nanogenerator based on ZnO nanostructures to overcome current limitations.

To achieve this goal, we have used a top-down approach that allows an accurate control of the aspect ratio and density of tailored ZnO nanowires by using Nano-Imprint Lithography and Atomic Layer Deposition. In our work, we demonstrate that this approach enables the fabrication of large flexible piezoelectric nanogenerators with interesting properties.

In the first part of this work, we have optimized the synthesis of crystalline N-doped ZnO films by ALD at a deposition temperature as low as T = 80 °C. We have particularly investigated the role of the time of purge with nitrogen as purge gas in each cycle of a ZnO monolayer of the ALD process. A thorough chemical and structural analysis illustrates that the time of purge allows tuning the N-doping-level which, despite being low, affects both the long-range and

short-range structure. Raman and luminescence spectroscopy suggest a complex defect structure, characterized by nitrogen ions which substitute oxygen ions and by Zn cations on interstitial sites. Importantly, even the low level of nitrogen doping allows tuning the sheet resistivity of ZnO films by several orders of magnitude. The ability to obtain crystallized and tunable N-doped ZnO films down to 80 °C by ALD provides a critical building block to tune structural, optic and electric properties for a variety of applications.

In the second part, we have designed, fabricated and characterized a new type of PENGs based on patterned nanostructures made of conical-shape ZnO pillars. First, we have used a finite element modeling to identify the optimization for the electromechanical performances of the ZnO nanowires, namely in terms of their aspect ratio and pitch. This has defined the stamps of the nano-imprint, which has then be combined with a low temperature conformal ALD to provide ZnO conical nanostructures. A thorough structural analysis of such nanostructures attests a high crystallinity, a polycrystalline growth and piezoelectric properties. This has been the necessary technological achievement for addressing in a next step functional patterned piezoelectric nanogenerators.

We have produced small flexible devices with an active area of 4 x 4 mm^2, using either a blocking electronic barrier with alumina, either a p-n junction with a conductive polymer (PEDOT:PSS). The different devices and architectures have then been characterized at matching impedance. The electric characterization of a device with a p-n junction exhibits a maximum output voltage of 0.2 V and a power density of 0.3 $\mu W\ cm^{-2}$. An effective transverse piezoelectric coefficient value e_{31eff} of -0.45 $C\ m^{-2}$ is determined, which corresponds to the order of magnitude reported in literature.

As a proof of concept for potential industrialization, we scaled the P-PENGs up to 20 cm^2 for large flexible substrates. The 3.7 billion pillars, sandwiched between electrodes, evidence the robustness of our process. The analysis of the constitutive piezoelectric equations has prompted us to pay a particular attention to an accurate setup for P-PENGs characterization, which turns out to be mandatory to compare accurately devices. For this, we setup an electromechanical actuator. Two devices with the same architecture but with different levels of N-doping are compared. Using an equivalent electrical model, the performance of the P-PENG with the higher N-doped ZnO shows a larger output voltage and power density than the device with a lower N-doping level. This comparison shows that the higher N-doping-level leads to an increase of 150 % of the power output. From this we calculate that the effective piezoelectric coefficient increases by about 60 % for a P-PENG based on higher N-doped ZnO.

This latter demonstrates an energy conversion efficiency of 10 %, on top of PENG based on ZnO.

Several perspectives arise from our work. First, a further in–depth study of the upper limit of the nitrogen doping level in ZnO with longer times of purge or plasma activation could radically change the properties of ZnO:N as suggested from the resiscope measurement. We expect that an even higher level of N-doping will further increase the P-PENG performance. Second, combining higher N-doped ZnO (more resistive than the lower N-doped ZnO) with a p-n junction architecture is expected to harvest larger amounts of energy than a blocking barrier. This merits to be explored with PEDOT by PRAP-CVD as expected from the first large P-PENG. The perspective of a multi-stack P-PENG becomes a realistic process with the UV-NIL and low temperature ALD. That multi-stack devices require a few technological developments to be demonstrated and would lead to an increase of the P-PENG performances. For other applications like strain sensor, the piezoresistive effect revealed in this work opens new avenues for designing flexible strain sensors with improved accuracy and sensitivity. Finally, another perspective for NIL would be the use of a ferroelectric polymer as template for the ZnO nanostructures to increase the P-PENG performance, similarly to composite based PENGs [5].

References

[1] Brian Womack, “Dell Will Spend $1 Billion in New Focus on Internet of Things,” *Bloomberg*, 2017. [Online]. Available: https://www.bloomberg.com/news/articles/2017-10-10/dell-will-spend-1-billion-in-new-focus-on-internet-of-things.

[2] S. Stephenson, “No Place Like Home: The Internet Of Things And Its Promise For Consumers,” *Forbes*, 2017. [Online]. Available: https://www.forbes.com/sites/scottstephenson/2017/12/18/no-place-like-home-the-internet-of-things-and-its-promise-for-consumers/#18233c2f5fe2. [Accessed: 01-Jan-2017].

[3] TJ McCue, “$117 Billion Market For Internet of Things In Healthcare By 2020,” *Forbes*, 2015. [Online]. Available: https://www.forbes.com/sites/tjmccue/2015/04/22/117-billion-market-for-internet-of-things-in-healthcare-by-2020/#51f9657f69d9.

[4] Q. Zheng, B. Shi, Z. Li, and Z. L. Wang, “Recent Progress on Piezoelectric and Triboelectric Energy Harvesters in Biomedical Systems,” *Adv. Sci.*, vol. 4, no. 7, p. 1700029, Jul. 2017.

[5] K.-I. Park, C. K. Jeong, N. K. Kim, and K. J. Lee, “Stretchable piezoelectric nanocomposite generator,” *Nano Converg.*, vol. 3, no. 1, p. 12, Dec. 2016.

[6] Z. L. Wang, G. Zhu, Y. Yang, S. Wang, and C. Pan, “Progress in nanogenerators for portable electronics,” *Mater. Today*, vol. 15, no. 12, pp. 532–543, Dec. 2012.

[7] A. M. Roji M, J. G, and A. B. Raj T, “A retrospect on the role of piezoelectric nanogenerators in the development of the green world,” *RSC Adv.*, vol. 7, no. 53, pp. 33642–33670, 2017.

[8] Z. L. Wang, “On Maxwell’s displacement current for energy and sensors: the origin of nanogenerators,” *Mater. Today*, vol. 20, no. 2, pp. 74–82, Mar. 2017.

[9] F. R. Fan, W. Tang, and Z. L. Wang, “Flexible Nanogenerators for Energy Harvesting and Self-Powered Electronics,” *Adv. Mater.*, vol. 28, no. 22, pp. 4283–4305, 2016.

[10] K. V. Selvan and M. S. Mohamed Ali, “Micro-scale energy harvesting devices: Review of methodological performances in the last decade,” *Renew. Sustain. Energy Rev.*, vol. 54, pp. 1035–1047, Feb. 2016.

[11] K. A. Cook-Chennault, N. Thambi, and A. M. Sastry, “Powering MEMS portable devices—a review of non-regenerative and regenerative power supply systems with special emphasis on piezoelectric energy harvesting systems,” *Smart Mater. Struct.*, vol. 17, no. 4, p. 43001, Aug. 2008.

[12] S. Priya and D. J. Inman, *Energy Harvesting Technologies*. Boston, MA: Springer US, 2009.

[13] D. P. Arnold, “Review of Microscale Magnetic Power Generation,” *IEEE Trans. Magn.*, vol. 43, no. 11, pp. 3940–3951, Nov. 2007.

[14] Frost & Sullivan, *Advances in Energy Harvesting Methods*. New York, NY: Springer New York, 2013.

[15] Q. Deng, L. Liu, and P. Sharma, “Electrets in soft materials: Nonlinearity, size effects, and giant electromechanical coupling,” *Phys. Rev. E*, vol. 90, no. 1, p. 12603, Jul. 2014.

[16] F.-R. Fan, Z.-Q. Tian, and Z. Lin Wang, “Flexible triboelectric generator,” *Nano Energy*, vol. 1, no. 2, pp. 328–334, Mar. 2012.

[17] F. R. Fan, W. Tang, and Z. L. Wang, “Flexible Nanogenerators for Energy Harvesting and Self-Powered Electronics,” *Adv. Mater.*, vol. 28, no. 22, pp. 4283–4305, Jun. 2016.

[18] Y. Hu and Z. L. Wang, “Recent progress in piezoelectric nanogenerators as a sustainable power

source in self-powered systems and active sensors," *Nano Energy*, vol. 14, pp. 3–14, May 2015.

[19] C. R. Bowen, H. A. Kim, P. M. Weaver, and S. Dunn, "Piezoelectric and ferroelectric materials and structures for energy harvesting applications," *Energy Environ. Sci.*, vol. 7, no. 1, pp. 25–44, 2014.

[20] R. Ahmed, F. Mir, and S. Banerjee, "A review on energy harvesting approaches for renewable energies from ambient vibrations and acoustic waves using piezoelectricity," *Smart Mater. Struct.*, vol. 26, no. 8, p. 85031, Aug. 2017.

[21] S. Priya *et al.*, "A Review on Piezoelectric Energy Harvesting: Materials, Methods, and Circuits," *Energy Harvest. Syst.*, vol. 4, no. 1, pp. 3–39, Jan. 2017.

[22] A. Marin, S. Bressers, and S. Priya, "Multiple cell configuration electromagnetic vibration energy harvester," *J. Phys. D. Appl. Phys.*, vol. 44, no. 29, p. 295501, Jul. 2011.

[23] A. L. Kholkin, N. A. Pertsev, and A. V. Goltsev, "Piezoelectricity and Crystal Symmetry," in *Piezoelectric and Acoustic Materials for Transducer Applications*, Boston, MA: Springer US, 2008, pp. 17–38.

[24] S. Trolier-McKinstry and P. Muralt, "Thin Film Piezoelectrics for MEMS," *J. Electroceramics*, vol. 12, no. 1/2, pp. 7–17, Jan. 2004.

[25] Ieee, "An American National Standard IEEE Standard on Piezoelectricity," *Inst. Electr. Electron. Eng.*, 1988.

[26] H. S. Kim, J.-H. Kim, and J. Kim, "A review of piezoelectric energy harvesting based on vibration," *Int. J. Precis. Eng. Manuf.*, vol. 12, no. 6, pp. 1129–1141, Dec. 2011.

[27] A. Khan, Z. Abas, H. Soo Kim, and I. Oh, "Piezoelectric thin films: an integrated review of transducers and energy harvesting," *Smart Mater. Struct.*, vol. 25, no. 5, p. 53002, May 2016.

[28] J. C. Doll, B. C. Petzold, B. Ninan, R. Mullapudi, and B. L. Pruitt, "Aluminum nitride on titanium for CMOS compatible piezoelectric transducers," *J. Micromechanics Microengineering*, vol. 20, no. 2, p. 25008, Feb. 2010.

[29] Z. L. Wang, "Piezoelectric Nanogenerators Based on Zinc Oxide Nanowire Arrays," *Science (80-.).*, vol. 312, no. 5771, pp. 242–246, Apr. 2006.

[30] Z. L. Wang, "Energy Harvesting Using Piezoelectric Nanowires-A Correspondence on 'Energy Harvesting Using Nanowires?' by Alexe et al.," *Adv. Mater.*, vol. 21, no. 13, pp. 1311–1315, Apr. 2009.

[31] M. Alexe, S. Senz, M. A. Schubert, D. Hesse, and U. Gösele, "Energy Harvesting Using Nanowires?," *Adv. Mater.*, vol. 20, no. 21, pp. 4021–4026, Nov. 2008.

[32] X. Wang, J. Song, J. Liu, and Z. L. Wang, "Direct-Current Nanogenerator Driven by Ultrasonic Waves," *Science (80-.).*, vol. 316, no. 5821, pp. 102–105, Apr. 2007.

[33] R. Yang, Y. Qin, L. Dai, and Z. L. Wang, "Power generation with laterally packaged piezoelectric fine wires," *Nat. Nanotechnol.*, vol. 4, no. 1, pp. 34–39, Jan. 2009.

[34] S. Xu, Y. Qin, C. Xu, Y. Wei, R. Yang, and Z. L. Wang, "Self-powered nanowire devices," *Nat. Nanotechnol.*, vol. 5, no. 5, pp. 366–373, May 2010.

[35] G. Zhu, R. Yang, S. Wang, and Z. L. Wang, "Flexible High-Output Nanogenerator Based on Lateral ZnO Nanowire Array," *Nano Lett.*, vol. 10, no. 8, pp. 3151–3155, Aug. 2010.

[36] Y. Hu, Y. Zhang, C. Xu, G. Zhu, and Z. L. Wang, "High-Output Nanogenerator by Rational Unipolar Assembly of Conical Nanowires and Its Application for Driving a Small Liquid Crystal Display," *Nano Lett.*, vol. 10, no. 12, pp. 5025–5031, Dec. 2010.

[37] M. Skompska and K. Zarębska, "Electrodeposition of ZnO Nanorod Arrays on Transparent Conducting Substrates–a Review," *Electrochim. Acta*, vol. 127, no. May 2014, pp. 467–488, May 2014.

[38] R. Bao *et al.*, "Flexible and Controllable Piezo-Phototronic Pressure Mapping Sensor Matrix by ZnO NW/p-Polymer LED Array," *Adv. Funct. Mater.*, vol. 25, no. 19, pp. 2884–2891, May 2015.

[39] W. Wu, C. Pan, Y. Zhang, X. Wen, and Z. L. Wang, "Piezotronics and piezo-phototronics – From single nanodevices to array of devices and then to integrated functional system," *Nano Today*, vol. 8, no. 6, pp. 619–642, Dec. 2013.

[40] S. Xu, C. Lao, B. Weintraub, and Z. L. Wang, "Density-controlled growth of aligned ZnO nanowire arrays by seedless chemical approach on smooth surfaces," *J. Mater. Res.*, vol. 23, no. 8, pp. 2072–2077, Aug. 2008.

[41] M.-Y. Choi *et al.*, "Mechanically Powered Transparent Flexible Charge-Generating Nanodevices with Piezoelectric ZnO Nanorods," *Adv. Mater.*, vol. 21, no. 21, pp. 2185–2189, Jun. 2009.

[42] J. Liu, W. Wu, S. Bai, and Y. Qin, "Synthesis of High Crystallinity ZnO Nanowire Array on Polymer Substrate and Flexible Fiber-Based Sensor," *ACS Appl. Mater. Interfaces*, vol. 3, no. 11, pp. 4197–4200, Nov. 2011.

[43] W. Zhang, R. Zhu, V. Nguyen, and R. Yang, "Highly sensitive and flexible strain sensors based on vertical zinc oxide nanowire arrays," *Sensors Actuators A Phys.*, vol. 205, pp. 164–169, Jan. 2014.

[44] A. Kołodziejczak-Radzimska and T. Jesionowski, "Zinc Oxide—From Synthesis to Application: A Review," *Materials (Basel).*, vol. 7, no. 4, pp. 2833–2881, Apr. 2014.

[45] D. Choi *et al.*, "Fully Rollable Transparent Nanogenerators Based on Graphene Electrodes," *Adv. Mater.*, vol. 22, no. 19, pp. 2187–2192, Apr. 2010.

[46] S. Lee *et al.*, "Super-Flexible Nanogenerator for Energy Harvesting from Gentle Wind and as an Active Deformation Sensor," *Adv. Funct. Mater.*, vol. 23, no. 19, pp. 2445–2449, May 2013.

[47] Y. Hu, L. Lin, Y. Zhang, and Z. L. Wang, "Replacing a Battery by a Nanogenerator with 20 V Output," *Adv. Mater.*, vol. 24, no. 1, pp. 110–114, Jan. 2012.

[48] Y. Qin, X. Wang, and Z. L. Wang, "Microfibre–nanowire hybrid structure for energy scavenging," *Nature*, vol. 451, no. 7180, pp. 809–813, Feb. 2008.

[49] M. Lee *et al.*, "A Hybrid Piezoelectric Structure for Wearable Nanogenerators," *Adv. Mater.*, vol. 24, no. 13, pp. 1759–1764, Apr. 2012.

[50] Z. Li and Z. L. Wang, "Air/Liquid-Pressure and Heartbeat-Driven Flexible Fiber Nanogenerators as a Micro/Nano-Power Source or Diagnostic Sensor," *Adv. Mater.*, vol. 23, no. 1, pp. 84–89, Jan. 2011.

[51] N. Masghouni, J. Burton, M. K. Philen, and M. Al-Haik, "Investigating the energy harvesting capabilities of a hybrid ZnO nanowires/carbon fiber polymer composite beam," *Nanotechnology*, vol. 26, no. 9, p. 95401, Mar. 2015.

[52] Y. Qiu *et al.*, "Branched ZnO nanotrees on flexible fiber-paper substrates for self-powered energy-harvesting systems," *RSC Adv.*, vol. 5, no. 8, pp. 5941–5945, 2015.

[53] Z. Shao, L. Wen, D. Wu, X. Zhang, S. Chang, and S. Qin, "Influence of carrier concentration on piezoelectric potential in a bent ZnO nanorod," *J. Appl. Phys.*, vol. 108, no. 12, p. 124312, Dec. 2010.

[54] F. Wang *et al.*, "An aqueous solution-based doping strategy for large-scale synthesis of Sb-doped ZnO nanowires," *Nanotechnology*, vol. 22, no. 22, p. 225602, Jun. 2011.

[55] J. I. Sohn *et al.*, "Engineering of efficiency limiting free carriers and an interfacial energy barrier for an enhancing piezoelectric generation," *Energy Environ. Sci.*, vol. 6, no. 1, pp. 97–104, 2013.

[56] J. I. Sohn *et al.*, "A low temperature process for phosphorous doped ZnO nanorods via a combination of hydrothermal and spin-on dopant methods," *Nanoscale*, vol. 6, no. 4, pp. 2046–2051, 2014.

[57] S. Lee *et al.*, "Solution-processed Ag-doped ZnO nanowires grown on flexible polyester for nanogenerator applications," *Nanoscale*, vol. 5, no. 20, p. 9609, Oct. 2013.

[58] Y. Zhang *et al.*, "Lattice Strain Induced Remarkable Enhancement in Piezoelectric Performance of ZnO-Based Flexible Nanogenerators," *ACS Appl. Mater. Interfaces*, vol. 8, no. 2, pp. 1381–1387, Jan. 2016.

[59] J. Briscoe and S. Dunn, "Piezoelectric nanogenerators – a review of nanostructured piezoelectric energy harvesters," *Nano Energy*, vol. 14, pp. 15–29, May 2015.

[60] R. Hinchet, S. Lee, G. Ardila, L. Montès, M. Mouis, and Z. L. Wang, "Performance Optimization of Vertical Nanowire-based Piezoelectric Nanogenerators," *Adv. Funct. Mater.*, vol. 24, no. 7, pp. 971–977, Feb. 2014.

[61] J. Briscoe, M. Stewart, M. Vopson, M. Cain, P. M. Weaver, and S. Dunn, "Nanostructured p-n Junctions for Kinetic-to-Electrical Energy Conversion," *Adv. Energy Mater.*, vol. 2, no. 10, pp. 1261–1268, Oct. 2012.

[62] M. Y. Soomro, O. Nur, and M. Willander, "Enhancing the piezopotential from Zinc oxide (ZnO) nanowire using p-type polymers," *Mater. Lett.*, vol. 124, pp. 123–125, Jun. 2014.

[63] J. Briscoe *et al.*, "Measurement techniques for piezoelectric nanogenerators," *Energy Environ. Sci.*, vol. 6, no. 10, p. 3035, 2013.

[64] K.-I. Park *et al.*, "Piezoelectric BaTiO 3 Thin Film Nanogenerator on Plastic Substrates," *Nano Lett.*, vol. 10, no. 12, pp. 4939–4943, Dec. 2010.

[65] G. Zhu, A. C. Wang, Y. Liu, Y. Zhou, and Z. L. Wang, "Functional Electrical Stimulation by Nanogenerator with 58 V Output Voltage," *Nano Lett.*, vol. 12, no. 6, pp. 3086–3090, Jun. 2012.

[66] T. S. van den Heever and W. J. Perold, "Improving the output voltage of a ZnO nanogenerator by adding CNTs and lateral ZnO nanowires," *IEEE Trans. Nanotechnol.*, vol. 12, no. 6, pp. 1012–1017, 2013.

[67] S. Stassi, V. Cauda, C. Ottone, A. Chiodoni, C. F. Pirri, and G. Canavese, "Flexible piezoelectric energy nanogenerator based on ZnO nanotubes hosted in a polycarbonate membrane," *Nano Energy*, vol. 13, pp. 474–481, Apr. 2015.

[68] X. Chen, S. Xu, N. Yao, and Y. Shi, "1.6 V Nanogenerator for Mechanical Energy Harvesting Using PZT Nanofibers," *Nano Lett.*, vol. 10, no. 6, pp. 2133–2137, Jun. 2010.

[69] M.-L. Seol *et al.*, "Design Strategy for a Piezoelectric Nanogenerator with a Well-Ordered Nanoshell Array," *ACS Nano*, vol. 7, no. 12, pp. 10773–10779, Dec. 2013.

[70] R. A. Whiter, V. Narayan, and S. Kar-Narayan, "A Scalable Nanogenerator Based on Self-Poled Piezoelectric Polymer Nanowires with High Energy Conversion Efficiency," *Adv. Energy Mater.*, vol. 4, no. 18, p. 1400519, Dec. 2014.

[71] C. Ou *et al.*, "Template-Assisted Hydrothermal Growth of Aligned Zinc Oxide Nanowires for Piezoelectric Energy Harvesting Applications," *ACS Appl. Mater. Interfaces*, vol. 8, no. 22, pp. 13678–13683, Jun. 2016.

[72] N. Jalali *et al.*, "ZnO nanorod surface modification with PDDA/PSS Bi-layer assembly for performance improvement of ZnO piezoelectric energy harvesting devices," *J. Sol-Gel Sci. Technol.*, vol. 73, no. 3, pp. 544–549, Mar. 2015.

[73] F. L. Boughey, T. Davies, A. Datta, R. A. Whiter, S.-L. Sahonta, and S. Kar-Narayan, "Vertically aligned zinc oxide nanowires electrodeposited within porous polycarbonate templates for vibrational energy harvesting," *Nanotechnology*, vol. 27, no. 28, p. 28LT02, Jul. 2016.

[74] K. Il Park *et al.*, "Highly-efficient, flexible piezoelectric PZT thin film nanogenerator on plastic substrates," *Adv. Mater.*, vol. 26, no. 16, pp. 2514–2520, 2014.

[75] S. Crossley and S. Kar-Narayan, "Energy harvesting performance of piezoelectric ceramic and polymer nanowires," *Nanotechnology*, vol. 26, no. 34, p. 344001, Aug. 2015.

[76] O. Ishchenko, "Elaboration of Plasmonic Nano- Composites and Study of their Specific Catalytic Activities," 2016.

[77] V. Rogé *et al.*, "Improvement of the photocatalytic degradation property of atomic layer deposited ZnO thin films: the interplay between film properties and functional performances," *J. Mater. Chem. A*, vol. 3, no. 21, pp. 11453–11461, 2015.

[78] B. R. Pistillo *et al.*, "One step deposition of PEDOT films by plasma radicals assisted polymerization via chemical vapour deposition," *J. Mater. Chem. C*, vol. 4, no. 24, pp. 5617–5625, 2016.

[79] B. R. Pistillo, K. Menguelti, D. Arl, F. Addiego, and D. Lenoble, "PRAP-CVD: how to design high conformal PEDOT surfaces," *RSC Adv.*, vol. 7, no. 31, pp. 19117–19123, 2017.

[80] S. Tanuma, C. J. Powell, and D. R. Penn, "Calculations of electron inelastic mean free paths (IMFPS). IV. Evaluation of calculated IMFPs and of the predictive IMFP formula TPP-2 for electron energies between 50 and 2000 eV," *Surf. Interface Anal.*, vol. 20, no. 1, pp. 77–89, Jan. 1993.

[81] Z. L. Wang, "From nanogenerators to piezotronics—A decade-long study of ZnO nanostructures," *MRS Bull.*, vol. 37, no. 9, pp. 814–827, 2012.

[82] X. Wang, "Piezoelectric nanogenerators—Harvesting ambient mechanical energy at the nanometer scale," *Nano Energy*, vol. 1, no. 1, pp. 13–24, Jan. 2012.

[83] E. Guziewicz *et al.*, “Extremely low temperature growth of ZnO by atomic layer deposition,” *J. Appl. Phys.*, vol. 103, no. 3, p. 33515, Feb. 2008.

[84] O. Game, U. Singh, A. A. Gupta, A. Suryawanshi, A. Banpurkar, and S. Ogale, “Concurrent synthetic control of dopant (nitrogen) and defect complexes to realize broadband (UV–650 nm) absorption in ZnO nanorods for superior photo-electrochemical performance,” *J. Mater. Chem.*, vol. 22, no. 33, p. 17302, 2012.

[85] A. Janotti and C. G. Van de Walle, “Fundamentals of zinc oxide as a semiconductor,” *Reports Prog. Phys.*, vol. 72, no. 12, p. 126501, Dec. 2009.

[86] A. Tsukazaki *et al.*, “Repeated temperature modulation epitaxy for p-type doping and light-emitting diode based on ZnO,” *Nat. Mater.*, vol. 4, no. 1, pp. 42–46, Dec. 2004.

[87] D. C. Look and B. Claflin, “P-type doping and devices based on ZnO,” *Phys. status solidi*, vol. 241, no. 3, pp. 624–630, Mar. 2004.

[88] E. S. Tuzemen, K. Kara, S. Elagoz, D. K. Takci, I. Altuntas, and R. Esen, “Structural and electrical properties of nitrogen-doped ZnO thin films,” *Appl. Surf. Sci.*, vol. 318, pp. 157–163, Nov. 2014.

[89] D. Snigurenko, K. Kopalko, T. A. Krajewski, R. Jakiela, and E. Guziewicz, “Nitrogen doped p -type ZnO films and p-n homojunction,” *Semicond. Sci. Technol.*, vol. 30, no. 1, p. 15001, Jan. 2015.

[90] E. Guziewicz *et al.*, “Abundant Acceptor Emission from Nitrogen-Doped ZnO Films Prepared by Atomic Layer Deposition under Oxygen-Rich Conditions,” *ACS Appl. Mater. Interfaces*, vol. 9, no. 31, pp. 26143–26150, Aug. 2017.

[91] D. Snigurenko *et al.*, “N and Al co-doping as a way to p-type ZnO without post-growth annealing,” *Mater. Res. Express*, vol. 3, no. 12, p. 125907, Dec. 2016.

[92] C. H. Park, S. B. Zhang, and S.-H. Wei, “Origin of p -type doping difficulty in ZnO: The impurity perspective,” *Phys. Rev. B*, vol. 66, no. 7, p. 73202, Aug. 2002.

[93] Ü. Özgür *et al.*, “A comprehensive review of ZnO materials and devices,” *J. Appl. Phys.*, vol. 98, no. 4, p. 41301, Aug. 2005.

[94] A. Ohtomo and A. Tsukazaki, “Pulsed laser deposition of thin films and superlattices based on ZnO,” *Semicond. Sci. Technol.*, vol. 20, no. 4, pp. S1–S12, Apr. 2005.

[95] K. Ellmer, “Magnetron sputtering of transparent conductive zinc oxide: relation between the sputtering parameters and the electronic properties,” *J. Phys. D. Appl. Phys.*, vol. 33, no. 4, pp. R17–R32, Feb. 2000.

[96] Y. W. Heo, D. P. Norton, and S. J. Pearton, “Origin of green luminescence in ZnO thin film grown by molecular-beam epitaxy,” *J. Appl. Phys.*, vol. 98, no. 7, p. 73502, Oct. 2005.

[97] T. Tynell and M. Karppinen, “Atomic layer deposition of ZnO: a review,” *Semicond. Sci. Technol.*, vol. 29, no. 4, p. 43001, Apr. 2014.

[98] P. C. Rowlette, C. G. Allen, O. B. Bromley, A. E. Dubetz, and C. A. Wolden, “Plasma-Enhanced Atomic Layer Deposition of Semiconductor Grade ZnO Using Dimethyl Zinc,” *Chem. Vap. Depos.*, vol. 15, no. 1–3, pp. 15–20, Mar. 2009.

[99] J. Lim and C. Lee, “Effects of substrate temperature on the microstructure and photoluminescence properties of ZnO thin films prepared by atomic layer deposition,” *Thin Solid Films*, vol. 515, no. 7–8, pp. 3335–3338, Feb. 2007.

[100] S. Jeon *et al.*, “Structural and Electrical Properties of ZnO Thin Films Deposited by Atomic Layer Deposition at Low Temperatures,” *J. Electrochem. Soc.*, vol. 155, no. 10, p. H738, 2008.

[101] K. Tapily, D. Gu, H. Baumgart, G. Namkoong, D. Stegall, and A. A. Elmustafa, “Mechanical and structural characterization of atomic layer deposition-based ZnO films,” *Semicond. Sci. Technol.*, vol. 26, no. 11, p. 115005, Nov. 2011.

[102] H. Makino, A. Miyake, T. Yamada, N. Yamamoto, and T. Yamamoto, “Influence of substrate temperature and Zn-precursors on atomic layer deposition of polycrystalline ZnO films on glass,” *Thin Solid Films*, vol. 517, no. 10, pp. 3138–3142, Mar. 2009.

[103] M. Godlewski *et al.*, “ZnO layers grown by Atomic Layer Deposition: A new material for transparent conductive oxide,” *Thin Solid Films*, vol. 518, no. 4, pp. 1145–1148, Dec. 2009.

[104] I. a. Kowalik *et al.*, “Structural and optical properties of low-temperature ZnO films grown by atomic layer deposition with diethylzinc and water precursors,” *J. Cryst. Growth*, vol. 311, no. 4, pp. 1096–1101, Feb. 2009.

[105] S.-Y. Pung, K.-L. Choy, X. Hou, and C. Shan, “Preferential growth of ZnO thin films by the atomic layer deposition technique,” *Nanotechnology*, vol. 19, no. 43, p. 435609, Oct. 2008.

[106] E. Przeździecka *et al.*, “Photoluminescence, electrical and structural properties of ZnO films, grown by ALD at low temperature,” *Semicond. Sci. Technol.*, vol. 24, no. 10, p. 105014, Oct. 2009.

[107] H. K. Park, B. S. Yang, S. Park, M. S. Kim, J. C. Shin, and J. Heo, “Purge-time-dependent growth of ZnO thin films by atomic layer deposition,” *J. Alloys Compd.*, vol. 605, pp. 124–130, Aug. 2014.

[108] J.-F. Chien, C.-H. Chen, J.-J. Shyue, and M.-J. Chen, “Local Electronic Structures and Electrical Characteristics of Well-Controlled Nitrogen-Doped ZnO Thin Films Prepared by Remote Plasma In situ Atomic Layer Doping,” *ACS Appl. Mater. Interfaces*, vol. 4, no. 7, pp. 3471–3475, Jul. 2012.

[109] S. J. Lim, S. J. Kwon, H. Kim, and J. S. Park, “High performance thin film transistor with low temperature atomic layer deposition nitrogen-doped ZnO,” *Appl. Phys. Lett.*, vol. 91, no. 18, pp. 2013–2016, 2007.

[110] L.-J. Meng, C. P. Moreira de Sá, and M. P. dos Santos, “Study of the structural properties of ZnO thin films by x-ray photoelectron spectroscopy,” *Appl. Surf. Sci.*, vol. 78, no. 1, pp. 57–61, May 1994.

[111] J. Iqbal, A. Jilani, P. M. Ziaul Hassan, S. Rafique, R. Jafer, and A. A. Alghamdi, “ALD grown nanostructured ZnO thin films: Effect of substrate temperature on thickness and energy band gap,” *J. King Saud Univ. - Sci.*, vol. 28, no. 4, pp. 347–354, Oct. 2016.

[112] T. M. Barnes, K. Olson, and C. A. Wolden, “On the formation and stability of p-type conductivity in nitrogen-doped zinc oxide,” *Appl. Phys. Lett.*, vol. 86, no. 11, p. 112112, Mar. 2005.

[113] M. Wang *et al.*, “N Doping to ZnO Nanorods for Photoelectrochemical Water Splitting under Visible Light: Engineered Impurity Distribution and Terraced Band Structure,” *Sci. Rep.*, vol. 5, no. 1, p. 12925, Oct. 2015.

[114] T. Sander, S. Eisermann, B. K. Meyer, and P. J. Klar, “Raman tensor elements of wurtzite ZnO,” *Phys. Rev. B*, vol. 85, no. 16, p. 165208, Apr. 2012.

[115] A. Calzolari and M. B. Nardelli, “Dielectric properties and Raman spectra of ZnO from a first principles finite-differences/finite-fields approach,” *Sci. Rep.*, vol. 3, no. 1, p. 2999, Dec. 2013.

[116] V. Russo, M. Ghidelli, P. Gondoni, C. S. Casari, and A. Li Bassi, “Multi-wavelength Raman scattering of nanostructured Al-doped zinc oxide,” *J. Appl. Phys.*, vol. 115, no. 7, p. 73508, Feb. 2014.

[117] R. Cuscó *et al.*, “Temperature dependence of Raman scattering in ZnO,” *Phys. Rev. B*, vol. 75, no. 16, p. 165202, Apr. 2007.

[118] F. J. Manjón, B. Marí, J. Serrano, and A. H. Romero, “Silent Raman modes in zinc oxide and related nitrides,” *J. Appl. Phys.*, vol. 97, no. 5, p. 53516, Mar. 2005.

[119] P. Sundara Venkatesh, V. Ramakrishnan, and K. Jeganathan, “Raman silent modes in vertically aligned undoped ZnO nanorods,” *Phys. B Condens. Matter*, vol. 481, pp. 204–208, Jan. 2016.

[120] F. Friedrich, M. A. Gluba, and N. H. Nickel, “Identification of nitrogen and zinc related vibrational modes in ZnO,” *Appl. Phys. Lett.*, vol. 95, no. 14, p. 141903, Oct. 2009.

[121] M. A. Gluba, N. H. Nickel, and N. Karpensky, “Interstitial zinc clusters in zinc oxide,” *Phys. Rev. B*, vol. 88, no. 24, p. 245201, Dec. 2013.

[122] A. Kaschner *et al.*, “Nitrogen-related local vibrational modes in ZnO:N,” *Appl. Phys. Lett.*, vol. 80, no. 11, pp. 1909–1911, Mar. 2002.

[123] F. Friedrich and N. H. Nickel, “Resonant Raman scattering in hydrogen and nitrogen doped ZnO,” *Appl. Phys. Lett.*, vol. 91, no. 11, p. 111903, Sep. 2007.

[124] P. A. Rodnyi and I. V. Khodyuk, “Optical and luminescence properties of zinc oxide (Review),” *Opt. Spectrosc.*, vol. 111, no. 5, pp. 776–785, Nov. 2011.

[125] C. H. Ahn, Y. Y. Kim, D. C. Kim, S. K. Mohanta, and H. K. Cho, “A comparative analysis of deep level emission in ZnO layers deposited by various methods,” *J. Appl. Phys.*, vol. 105, no. 1, p. 13502, Jan. 2009.

[126] V. Srikant and D. R. Clarke, "On the optical band gap of zinc oxide," *J. Appl. Phys.*, vol. 83, no. 10, pp. 5447–5451, May 1998.

[127] B. Lin, Z. Fu, Y. Jia, and G. Liao, "Defect Photoluminescence of Undoping ZnO Films and Its Dependence on Annealing Conditions," *J. Electrochem. Soc.*, vol. 148, no. 3, p. G110, 2001.

[128] H. Zeng, G. Duan, Y. Li, S. Yang, X. Xu, and W. Cai, "Blue Luminescence of ZnO Nanoparticles Based on Non-Equilibrium Processes: Defect Origins and Emission Controls," *Adv. Funct. Mater.*, vol. 20, no. 4, pp. 561–572, Feb. 2010.

[129] X. M. Fan, J. S. Lian, Z. X. Guo, and H. J. Lu, "Microstructure and photoluminescence properties of ZnO thin films grown by PLD on Si(111) substrates," *Appl. Surf. Sci.*, vol. 239, no. 2, pp. 176–181, Jan. 2005.

[130] M. Willander *et al.*, "Luminescence from Zinc Oxide Nanostructures and Polymers and their Hybrid Devices," *Materials (Basel).*, vol. 3, no. 4, pp. 2643–2667, Apr. 2010.

[131] M. D. McCluskey and S. J. Jokela, "Defects in ZnO," *J. Appl. Phys.*, vol. 106, no. 7, p. 71101, Oct. 2009.

[132] F. Stavale, L. Pascua, N. Nilius, and H.-J. Freund, "Luminescence Properties of Nitrogen-Doped ZnO," *J. Phys. Chem. C*, vol. 118, no. 25, pp. 13693–13696, Jun. 2014.

[133] D. C. Look, D. C. Reynolds, C. W. Litton, R. L. Jones, D. B. Eason, and G. Cantwell, "Characterization of homoepitaxial p -type ZnO grown by molecular beam epitaxy," *Appl. Phys. Lett.*, vol. 81, no. 10, pp. 1830–1832, Sep. 2002.

[134] J. Wang *et al.*, "Oxygen Vacancy Induced Band-Gap Narrowing and Enhanced Visible Light Photocatalytic Activity of ZnO," *ACS Appl. Mater. Interfaces*, vol. 4, no. 8, pp. 4024–4030, Aug. 2012.

[135] P. M. Verghese and D. R. Clarke, "Piezoelectric contributions to the electrical behavior of ZnO varistors," *J. Appl. Phys.*, vol. 87, no. 9, pp. 4430–4438, May 2000.

[136] J. W. Orton and M. J. Powell, "The Hall effect in polycrystalline and powdered semiconductors," *Reports Prog. Phys.*, vol. 43, no. 11, pp. 1263–1307, Nov. 1980.

[137] S. B. Kuntze, E. H. Sargent, S. J. Dixon-Warren, J. K. White, K. Hinzer, and D. Ban, "Nanoscopic electric potential probing: Influence of probe–sample interface on spatial resolution," *Appl. Phys. Lett.*, vol. 84, no. 4, pp. 601–603, Jan. 2004.

[138] A. L. Kholkin, S. V. Kalinin, A. Roelofs, and A. Gruverman, "Review of Ferroelectric Domain Imaging by Piezoresponse Force Microscopy," in *Scanning Probe Microscopy*, vol. 1, no. January, New York, NY: Springer New York, 2007, pp. 173–214.

[139] F. Johann *et al.*, "Depth resolution of piezoresponse force microscopy," *Appl. Phys. Lett.*, vol. 94, no. 17, p. 172904, Apr. 2009.

[140] J. Song, X. Wang, J. Liu, H. Liu, Y. Li, and Z. L. Wang, "Piezoelectric Potential Output from ZnO Nanowire Functionalized with p-Type Oligomer," *Nano Lett.*, vol. 8, no. 1, pp. 203–207, Jan. 2008.

[141] Y. Gao and Z. L. Wang, "Electrostatic potential in a bent piezoelectric nanowire. The fundamental theory of nanogenerator and nanopiezotronics.," *Nano Lett.*, vol. 7, no. 8, pp. 2499–505, Aug. 2007.

[142] S. Lee, B. Park, J. S. Kim, and T. Kim, "Designs and processes toward high-aspect-ratio nanostructures at the deep nanoscale: unconventional nanolithography and its applications," *Nanotechnology*, vol. 27, no. 47, p. 474001, Nov. 2016.

[143] H. Schift, "Nanoimprint lithography: 2D or not 2D? A review," *Appl. Phys. A*, vol. 121, no. 2, pp. 415–435, Nov. 2015.

[144] V. J. Cadarso, N. Chidambaram, L. Jacot-Descombes, and H. Schift, "High-aspect-ratio nanoimprint process chains," *Microsystems Nanoeng.*, vol. 3, no. January, p. 17017, Jul. 2017.

[145] G. Shao, J. Wu, Z. Cai, and W. Wang, "Fabrication of elastomeric high-aspect-ratio microstructures using polydimethylsiloxane (PDMS) double casting technique," *Sensors Actuators A Phys.*, vol. 178, pp. 230–236, May 2012.

[146] H. Yoon, H. Lee, and W. B. Lee, "Toward residual-layer-free nanoimprint lithography in large-area fabrication," *Korea-Australia Rheol. J.*, vol. 26, no. 1, pp. 39–48, Feb. 2014.

[147] W. Jiang *et al.*, "Bio-inspired directional high-aspect-ratio nanopillars: fabrication and actuation," *RSC Adv.*, vol. 4, no. 79, pp. 42002–42008, 2014.

[148] P. Zubko, G. Catalan, and A. K. Tagantsev, "Flexoelectric Effect in Solids," *Annu. Rev. Mater. Res.*, vol. 43, no. 1, pp. 387–421, Jul. 2013.

[149] A. Abdollahi, C. Peco, D. Millán, M. Arroyo, and I. Arias, "Computational evaluation of the flexoelectric effect in dielectric solids," *J. Appl. Phys.*, vol. 116, no. 9, p. 93502, Sep. 2014.

[150] M.-T. Hoang, J. Yvonnet, A. Mitrushchenkov, and G. Chambaud, "First-principles based multiscale model of piezoelectric nanowires with surface effects," *J. Appl. Phys.*, vol. 113, no. 1, p. 14309, Jan. 2013.

[151] E. Defaÿ, C. Zinck, C. Malhaire, N. Baboux, and D. Barbier, "Modified free vibrating beam method for characterization of effective e31 coefficient and leakage resistance of piezoelectric thin films," *Rev. Sci. Instrum.*, vol. 77, no. 10, p. 103903, Oct. 2006.

[152] P. Wang, S. Shi, and H. Du, "Fabrication and performance of ZnO piezoelectric cantilever for vibration energy harvesting," in *2015 Symposium on Piezoelectricity, Acoustic Waves, and Device Applications (SPAWDA)*, 2015, pp. 147–151.

[153] P. Muralt, J. Conde, A. Artieda, F. Martin, and M. Cantoni, "Piezoelectric materials parameters for piezoelectric thin films in GHz applications," *Int. J. Microw. Wirel. Technol.*, vol. 1, no. 1, p. 19, Feb. 2009.

[154] Hyun-Uk Kim, Woo-Ho Lee, H. V. R. Dias, and S. Priya, "Piezoelectric Microgenerators-Current Status and Challenges," *IEEE Trans. Ultrason. Ferroelectr. Freq. Control*, vol. 56, no. 8, pp. 1555–1568, Aug. 2009.

[155] T. Wang, H. Wu, C. Chen, and C. Liu, "Growth, optical, and electrical properties of nonpolar m-plane ZnO on p-Si substrates with Al 2 O 3 buffer layers," *Appl. Phys. Lett.*, vol. 100, no. 1, p. 11901, Jan. 2012.

[156] W. Wu and Z. L. Wang, "Piezotronics and piezo-phototronics for adaptive electronics and optoelectronics," *Nat. Rev. Mater.*, vol. 1, no. 7, p. 16031, May 2016.

[157] J. I. Sohn *et al.*, "Modification of electrical and piezoelectric properties of ZnO nanorods based on arsenic incorporation via low temperature spin-on-dopant method," *J. Korean Phys. Soc.*, vol. 67, no. 5, pp. 930–935, Sep. 2015.

[158] P. Thakur *et al.*, "Superior performances of in situ synthesized ZnO/PVDF thin film based self-poled piezoelectric nanogenerator and self-charged photo-power bank with high durability," *Nano Energy*, vol. 44, no. October 2017, pp. 456–467, Feb. 2018.

[159] T. Hehn and Y. Manoli, *CMOS Circuits for Piezoelectric Energy Harvesters*, vol. 38. Dordrecht: Springer Netherlands, 2015.

[160] W. K. Schomburg, *Introduction to Microsystem Design*, vol. 1. Berlin, Heidelberg: Springer Berlin Heidelberg, 2011.